Assessing ZrC Degradation Under Thermal and Oxidative Stress

Master Thesis Report

Eden Pfanner

Delft University of Technology

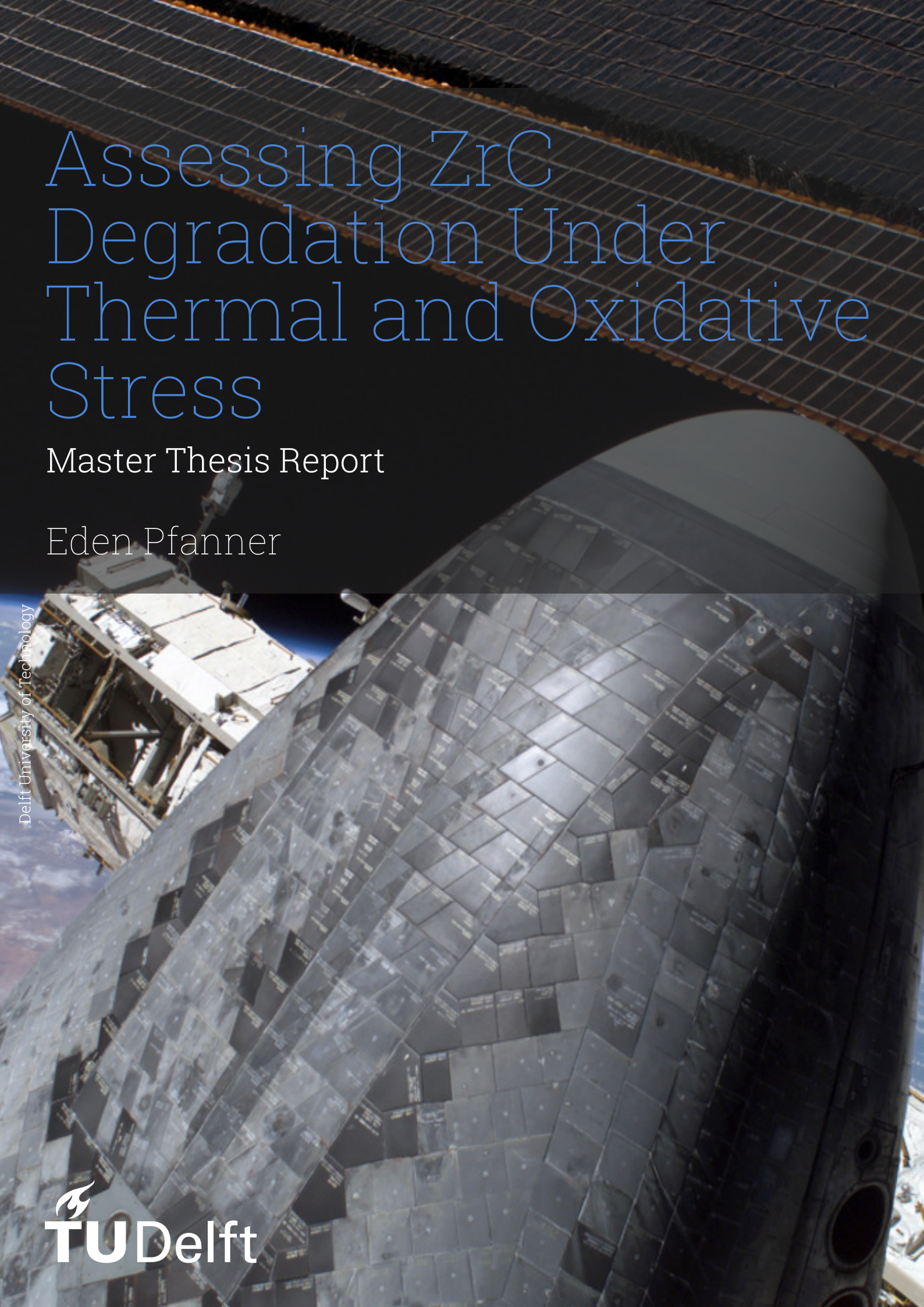

TU Delft

Assessing ZrC Degradation Under Thermal and Oxidative Stress

Master Thesis Report

by

Eden Pfanner

to obtain the degree of Master of Science
at the Delft University of Technology, Faculty Aerospace Engineering,
to be defended publicly on July 11, 2025.

Thesis Committee:

Chair:	Roger Groves
Supervisor:	Yinglu Tang
Daily Supervisor:	Yun-Ching Lin
Examiners:	Baris Kumru
Project Duration:	November 2024 - July 2025
Student Number:	5673410

Cover: Space Shuttle Discovery's thermal protection system tiles (Canopy Aerospace) by NASA

TU Delft

Acknowledgment

I would like to thank my supervisors, Dr. Yinglu Tang and Yun-Ching Lin, for their guidance, support, and constructive feedback throughout this project. Their inputs were valuable in helping shape the direction of this research and in navigating both technical and experimental challenges. I also appreciate the support of the staff of the Faculty of Aerospace Engineering, whose expertise and assistance have enriched both this work and my broader academic experience.

I would like to thank the technicians and staff in the Vliegtuighal labs, whose support with SEM, XRD, Raman spectroscopy, and TMA was essential to the success of this thesis. I am especially grateful for their patience and assistance with troubleshooting experimental challenges.

I am also thankful for the support and camaraderie of my classmates and colleagues, who provided not only technical advice but also a collaborative and enjoyable research environment. Finally, I would like to thank my family and friends for their support, encouragement, and understanding throughout this journey. Their belief in me made this achievement possible.

Eden Pfanner
Delft, July 2025

Abstract

Zirconium carbide (ZrC) is a promising ultra-high-temperature ceramic (UHTC) for thermal protection systems (TPS) due to its high melting point, thermal stability, and mechanical strength. However, its susceptibility to oxidative degradation and limited thermal shock resistance poses challenges for aerospace applications. This thesis investigates how prior oxidation history (defined by exposure temperature and duration) influences the thermal shock response of the zirconia oxide scale on monolithic ZrC. Samples were oxidized at 600°C, 700°C, and 800°C for varying durations, followed by thermal shock via water quenching. Post-exposure analysis using X-ray diffraction (XRD), Raman spectroscopy, scanning electron microscopy (SEM), and mass change measurements showed that increasing oxidation severity leads to thicker, brittle oxide scales with higher monoclinic ZrO_2 content and elevated crack densities. A transition to failure-prone behavior occurs between 700°C and 800°C, with failure thresholds defined by a ≥10% surface crack density and monoclinic ZrO_2 content exceeding 10%. These results establish oxidation-dependent limits for ZrC's thermal shock resistance.

Contents

List of Figures

List of Tables

Nomenclature

Abbreviations

Abbreviation	Definition
ACC	Advanced Carbon-Carbon
AO	Atomic Oxygen (O)
BDE	Bond Dissociation Energy
BSE	Backscattered Electrons
COMPO	Compositional Imaging Mode
CTE	Coefficient of Thermal Expansion
EDS	Energy-Dispersive X-ray Spectroscopy
FCC	Face-Centered Cubic
LEI	Low-Energy Imaging Mode
LEO	Low Earth Orbit
MO	Molecular Oxygen (O_2)
SEM	Scanning Electron Microscopy
SPS	Spark Plasma Sintering
TMA	Thermo-Mechanical Analysis
TPS	Thermal Protection System
UHTC	Ultra-High Temperature Ceramics
UV	Ultraviolet
XRD	X-Ray Diffraction

Symbols

Symbol	Definition	Unit
Δ	Difference	-
θ	Diffraction Angle	[degrees]

1 Introduction

1.1. The Challenge of Thermal Protection for Spacecraft

One of the challenges of space travel is selecting materials that can protect spacecraft from the harsh environments of space. During atmospheric re-entry, spacecraft are subjected to extreme temperatures and mechanical stresses that can compromise structural integrity. Since the dawn of space programs, thermal protection systems (TPS) have been critical for ensuring spacecraft arrive safely back to Earth. The materials used in these systems must endure excessive heat, which led to the development of ultra-high-temperature ceramics (UHTCs). These ceramic materials, with melting points over 3000°C, are defined by strong covalent bonding that allows them to withstand extreme conditions [1].

UHTCs are valuable for TPSs because of their refractory nature, providing stability at very high temperatures [2]. This stability stems from strong covalent bonding and modest ionic contributions enhancing thermal conductivity and defect tolerance. Originally developed in the 1960s for hypersonic flight vehicles, UHTCs have since proven their suitability for re-entry systems [2]. Today, space agencies worldwide favor materials such as hafnium diboride (HfB_2), zirconium diboride (ZrB_2), or silicon carbide (SiC)for their spacecraft due to their excellent properties in re-entry environments [3]. Among the many UHTCs studied, this thesis focuses specifically on monolithic zirconium carbide (ZrC) due to its exceptional thermal stability, high melting point, and relevance in extreme aerospace applications.

1.2. Role of Oxidation and Thermal Shock in Material Degradation

Although UHTCs exhibit outstanding thermal stability and ablation resistance, their application is often limited by inherent brittleness and poor resistance to thermally induced stresses, particularly in their monolithic form. During orbit, atmospheric re-entry, or other high-temperature transients, these materials are exposed to extreme thermal gradients, which generate internal thermal stresses that can lead to cracking or catastrophic failure [4].

ZrC, while boasting an exceptionally high melting point and hardness, is known to degrade under oxidative environments at high temperatures [5]. Oxidation promotes the formation of surface oxide layers, zirconia (ZrO_2) in this case, which may be porous, cracked, or non-uniform depending on temperature, oxygen partial pressure, and exposure duration. These oxide scales introduce significant volumetric changes and residual stresses due to mismatches in the coefficient of thermal expansion (CTE) [6]. ZrC has a relatively low CTE compared to zirconia phases. Monoclinic ZrO_2 exhibits the lowest CTE but is highly anisotropic, meaning its expansion varies significantly with crystallographic direction [7]. Tetragonal and cubic ZrO_2 both have substantially higher and more isotropic CTE values, with cubic typically being the highest [8]. As temperature increases, the expansion mismatch between ZrC and these zirconia phases becomes more pronounced. This generates significant tensile stresses during cooling, particularly when tetragonal or cubic phases are present, driving oxide cracking and delamination [6] [7]. This concept and the specific numerical CTE values involved will be discussed in more detail later in the presentation.

Along with oxidation, degradation is likely to occur from large temperature gradients induced from a shock or cycles. Thermal shock refers to a single, rapid temperature change, such as those induced by engine plume impingement or localized heating, causing steep thermal gradients and rapid stress

increase. In contrast, thermal cycling involves repeated heating and cooling, such as during multiple atmospheric passes or intermittent high-temperature operations. Though less intense per cycle than a thermal shock event, thermal cycling can accumulate damage over time through cyclic stress fatigue, progressive oxidation, and microstructural degradation.

Both phenomena are particularly detrimental when combined with oxidation: oxide layers can act as stress concentrators or delaminate under repeated strain, accelerating material failure. Understanding the distinctions and interactions between oxidation, thermal cycling, and thermal shock is therefore critical to evaluating the long-term structural integrity of monolithic UHTCs like ZrC under service-relevant thermal conditions.

1.3. Research Questions

The goal of this study is to understand how oxidation-induced changes in the surface oxide layer and its interaction with the ZrC substrate influence the thermal shock resistance of monolithic ZrC. To address current gaps in understanding, two key research questions are proposed:

1. **How does prior oxidation history (temperature and duration) affect the extent of surface and internal damage after thermal shock?** This question aims to quantitatively assess how oxidation parameters influence measurable outcomes, such as through-the-thickness crack density and the degree of oxide fracture and spallation observed after shock. By examining how these parameters correlate, the study identifies how oxidation history governs the severity of surface degradation.
2. **Under what oxidation conditions (temperature and duration) does ZrC become susceptible to critical failure when subjected to thermal shock?** This question focuses on defining critical thresholds of oxidation temperatures and durations beyond which the system exhibits clear signs of failure. This includes a >10% concentration of monoclinic ZrO_2, a >10% rise in crack density, or the visible onset of scale delamination [9] [10] [11] [12]. By mapping these limits, the study outlines operational boundaries for safe use under rapid cooling.

Together, these questions support a systematic understanding of thermal degradation mechanisms in monolithic ZrC and provide insight into its suitability for future aerospace applications involving high heat flux and sudden cooling.

2

Literature Review

Additional background information and data is required in order to answer the research questions.

2.1. Zirconium Carbide

Although not yet widely implemented in current aerospace systems, ZrC is recognized as a promising material for extreme environments due to its outstanding thermomechanical properties [6]. To better contextualize these properties, Table 2.1 compares ZrC against two benchmark aerospace materials: carbon-carbon (C/C) composites, a subset of advanced carbon–carbon (ACC) materials known for their lightweight high-temperature stability; and Inconel 718, a widely-used high-strength nickel superalloy. A visual representation of this comparison is also shown in Figure 2.1, highlighting the trade-offs between density, strength, and thermal performance.

Table 2.1: Comparisons of material properties at room temperature

Property	**ZrC** [6] [13] [14]	**C/C composite** [6] [15] [16]	**Inconel 718** [17]
Melting Point [°C]	3303 to 3530	3552	1260 to 1336
Density [g/cm^3]	6.73	1.65	8.19
Thermal Conductivity [W/m·K]	25	20 to 50	11.4
Elastic Modulus [GPa]	430	43 to 240	200
Hardness [GPa]	26.25	0.7	4.2
Flexural Strength [MPa]	460	100-200	1375

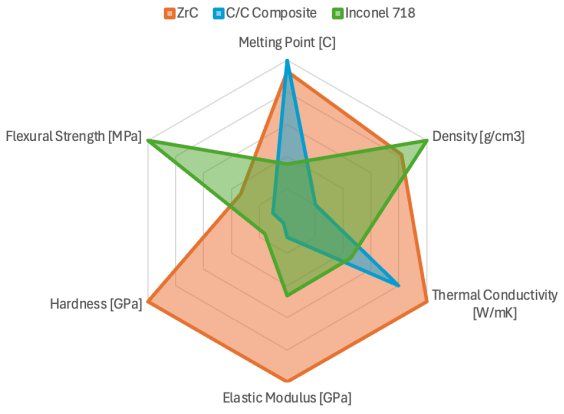

Figure 2.1: Normalized comparison of material properties at room temperature

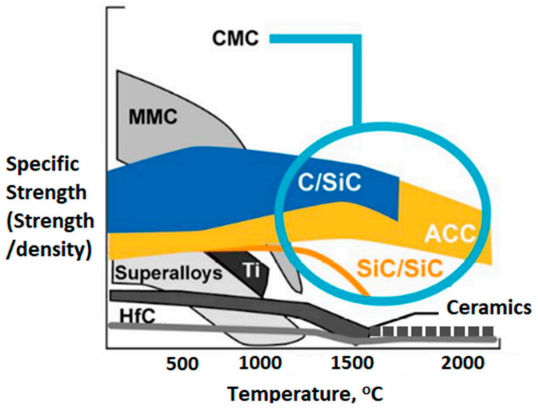

Figure 2.2: Specific strengths of materials typically used in high-temperature aerospace applications [6]

ZrC exhibits a combination of properties well-suited for extreme thermal environments, particularly those involving oxidation and rapid thermal gradients. Its melting point (3303–3530°C) is the highest among the materials compared [14], providing stability far beyond that of Inconel 718 (1260–1336°C)

[17]. While ZrC does require a protective coating above approximately 800°C to mitigate oxidation, this threshold is considerably higher than that of C/C composites, which begin to degrade in air above 500°C despite their high melting point in inert conditions [6].

A key advantage of ZrC is its ability to manage thermal stress. Its thermal conductivity (25 W/m·K) supports effective heat dissipation and minimizes localized gradients that drive thermal shock damage [14]. This conductivity is higher than Inconel (11.4 W/m·K) [17] and comparable to the in-plane conductivity of C/C composites (20–50 W/m·K) [16], although the anisotropic nature of composites can lead to uneven heat distribution.

Critically, ZrC's elastic modulus (430 GPa) indicates high stiffness, meaning thermal strains rapidly convert to stress, which is relevant for understanding crack formation during oxidation and shock [6]. This stiffness is substantially higher than that of C/C (43–240 GPa) and Inconel (200 GPa) [17], making ZrC more susceptible to brittle fracture but highly resistant to deformation.

Other properties further highlight ZrC's trade-offs in aerospace applications. Its density (6.73 g/cm³) [6] offers a middle ground: denser than lightweight C/C (1.65 g/cm³) [15] but lighter than Inconel (8.19 g/cm³) [17]. Its hardness (26.25 GPa) [14] greatly exceeds both C/C (0.7 GPa) [15] and Inconel (4.2 GPa) [17], providing excellent resistance to wear, erosion, and particulate damage in extreme environments. Although its flexural strength (460 MPa) [6] is lower than Inconel (1375 MPa) [17], it outperforms C/C composites (100–200 MPa) [15], which are limited by anisotropic behavior and manufacturing variability. These comparisons can be seen in Figure 2.2, where the specific strength of Inconel (superalloys) significantly decreases at high temperatures, while ZrC and C/C composites can be seen to maintain their strengths.

While comparisons with commonly used aerospace materials highlight ZrC's potential, its true relevance emerges when compared to other UHTCs. Materials like ZrB_2 and HfB_2 are more commonly used due to their superior thermal conductivity (60.9 W/m·K for ZrB_2 and 104.6 W/m·K for HfB_2) and higher fracture toughness (4.52 and 3.5 MPa·$m^{1/2}$, respectively) [18]. These properties make them highly effective for applications requiring strong thermal management and resistance to crack propagation.

Despite this, ZrC offers a distinct combination of advantages: it has the highest melting point (3530°C) and the highest hardness (26.25 GPa) among the UHTCs compared [6], along with a lower density (6.73 g/cm³) than HfB_2 (11.21 g/cm³) [18]. While its thermal conductivity (25 W/m·K) and fracture toughness (3 MPa·$m^{1/2}$) are lower, ZrC's flexural strength (460 MPa) remains comparable to ZrB_2 (450 MPa) and only slightly lower than HfB_2 (510 MPa) [6] [18]. Its elastic modulus (430 GPa) is also substantial, though marginally less than ZrB_2 (489 GPa) and HfB_2 (480 GPa) [6] [18].

Table 2.2: Comparison of monolithic UHTC properties at room temperature

Property	**ZrC** [6] [13] [14]	**ZrB_2** [18] [19]	**HfB_2** [18] [20]
Melting Point [°C]	3530	3245	3380
Density [g/cm^3]	6.73	6.12	11.21
Thermal Conductivity [W/m·K]	25	60.9	104.6
Young's Modulus [GPa]	430	489	480
Hardness [GPa]	26.25	16.5	19.8
Flexural Strength [MPa]	460	450	510
Fracture Toughness [MPa·$m^{\frac{1}{2}}$]	3	4.52	3.5

These trade-offs highlight why ZrC remains of interest: it provides a balance of extreme hardness, high-temperature stability, and lower density, which may benefit applications where erosion resistance, mechanical durability, and thermal extremes are critical, even if its oxidation resistance is less robust than borides. This emphasizes the need to better understand ZrC's behavior under combined oxidative and thermal stresses.

2.1.1. Monolithic vs. Composite UHTCs

One consideration in utilizing UHTCs is that they have traditionally suffered from poor fracture toughness, particularly in their monolithic forms. This intrinsic brittleness, although rooted in their strong

covalent bonding and high melting points, limits their use in environments with high thermal gradients and mechanical loads [1]. To address this, research has largely pivoted toward composite architectures, especially fiber-reinforced ceramic matrix composites (UHTCMCs). These systems combine UHTCs like ZrB_2 and HfB_2 with carbon or SiC fibers to enhance toughness through mechanisms such as crack deflection, fiber pull-out, and interface debonding [21]. Continuous fibers in particular have enabled the development of materials that can endure the complex thermal-mechanical loads found in hypersonic flight and atmospheric reentry [1].

Therefore, monolithic UHTCs remain underutilized and understudied, especially under high-temperature cyclic or rapid-cooling conditions. However, their simplified microstructures make them valuable for fundamental studies on damage initiation and oxidation mechanisms. They also offer potential advantages in environments where composite interfaces may degrade or delaminate under extreme oxidative or vacuum conditions [22]. In some applications, such as structural elements of thermal protection systems or non-load-bearing components exposed to transient heat spikes, the use of monolithic ceramics could be advantageous due to their straightforward fabrication and predictable behavior.

Recent flight tests, while highlighting the brittleness of monolithic UHTCs, also demonstrated their superior ablation resistance compared to traditional carbon-based composites, with lower recession rates under extreme heat fluxes [21]. This suggests untapped potential, provided their thermal degradation mechanisms can be better understood and mitigated. Such findings warrant a renewed evaluation of monolithic forms in design strategies where simpler, more durable solutions may be sufficient under specific operational conditions.

2.2. Oxidation of ZrC

Given their exposure to severe oxidative conditions, understanding the oxidation response of UHTCs like ZrC becomes crucial to improving their thermal and structural resilience. In particular, oxidation mechanisms due to molecular oxygen (O_2 or MO) are critical to characterize in order to understand ZrC's behavior in high-temperature oxidative environments.

MO-induced oxidation occurs in low-energy environments, such as terrestrial conditions, and is prominent at moderate to high temperatures (500–1500°C) and oxygen partial pressures ranging from 1 to 101 kPa [23]. The oxidation of ZrC under MO has been reported to follow reactions that produce zirconia and carbon oxides, typically CO or CO_2, depending on oxygen availability. These pathways are both thermodynamically favorable and experimentally validated under the temperature and pressure ranges relevant to this study [23] [24] [25]. Based on current literature and the oxidation conditions examined here, the following reactions are considered the most representative and plausible for describing the ZrC oxidation mechanism:

$$ZrC + 2O_2 \rightarrow ZrO_2 + CO_2 \tag{2.1}$$

$$2ZrC + 3O_2 \rightarrow 2ZrO_2 + 2CO \tag{2.2}$$

Byproducts CO_2 and CO are volatile and escape as gases, resulting in pores and cracks. These cracks promote oxidation deep within the material, leading to mass loss, damage, and reduced thermomechanical properties. Zirconia (ZrO_2), the solid oxidation product, forms on the surface as a ceramic scale and contributes to stress buildup due to its density mismatch with the underlying ZrC.

A study by Liu et al. involving C/SiC, where SiC is a comparable UHTC to ZrC, can be seen to display this behavior during a 10-hour period of exposure to MO at 1500°C [26]. This comparison is justified because SiC and ZrC share fundamental UHTC characteristics, including high melting points, strong covalent bonding, excellent thermal stability, and notable oxidation resistance, making their oxidation behaviors under MO exposure mechanistically similar [3] [21]. Figure 2.3 shows how MO oxidation leads to both compositional and morphological changes, as evidenced by the shift in X-Ray Diffraction (XRD) peaks and surface evolution observed in Scanning Electron Microscope (SEM) images. After 10 hours of exposure to 1500°C, the initially smooth microstructure becomes visibly rougher and more irregular, reflecting the formation of a zirconia-rich oxide layer. This newly developed surface exhibits

granular and uneven features, which indicate outward oxide growth and internal volume expansion. While visible cracks are not yet present, the surface coarsening and layering suggest the buildup of internal stresses and trapped gases, which may eventually lead to cracking or delamination with prolonged exposure.

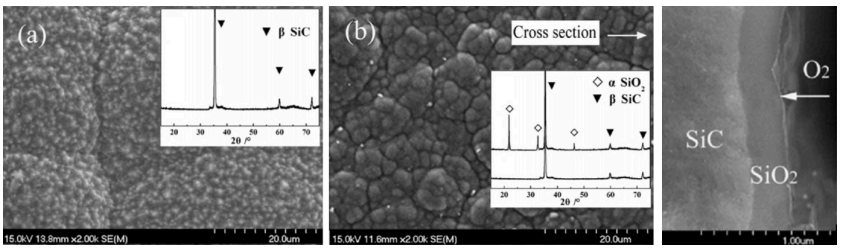

Figure 2.3: C/SiC (a) before oxidation and (b) after 10-hour oxidation with MO at 1500°C [26]

2.2.1. Oxygen Diffusion as a Precursor to Oxide Formation

Oxygen diffusion governs the initiation and growth of the oxide scale on ZrC. In ZrO_2, two key mechanisms facilitate oxygen transport: vacancy-mediated diffusion and interstitial diffusion [27]. Vacancy diffusion occurs when thermally activated oxygen atoms migrate by hopping into vacant oxygen lattice sites, which becomes prominent at elevated temperatures where vacancy concentrations are higher. These sites differ in local geometry; some are surrounded by three zirconium atoms, others by four, leading to significant variation in the energy required for diffusion. This causes oxygen to move easier in certain directions than others, making diffusion behavior strongly dependent on microstructure [27].

In contrast, interstitial diffusion involves oxygen atoms squeezing through the lattice in non-standard paths, typically becoming important near grain boundaries, in stressed regions, or when oxygen concentration is high. While less common in dense oxides, this mechanism can accelerate localized oxygen ingress and create zones of internal oxidation. These zones may introduce volumetric mismatch and residual stress that destabilize the oxide layer [27].

These mechanisms have distinct implications for oxide stability. Vacancy diffusion supports uniform oxide growth, while interstitial diffusion enables rapid but localized oxygen ingress, potentially triggering internal oxidation or stress buildup [27]. Such heterogeneity in oxygen transport can cause uneven expansion, delamination, or microcracking, especially under thermal cycling or shock conditions [28]. This is directly relevant to the damage behaviors observed in this study, where oxide spallation, interfacial cracking, and mass loss after thermal shock can be linked to how prior oxidation affected the distribution of residual stresses within the oxide scale.

2.2.2. Intermediate Layer

Although this work does not focus on characterizing the intermediate layer that may form during oxidation, it is important to acknowledge its possible presence. During the oxidation process of ZrC, researchers such as Gasparrini et al. have observed an intermediate phase forming between the unoxidized ZrC core and the fully oxidized ZrO_2 outer scale. This can be seen in Figure 2.4a, which shows cross-sectional SEM images of the ZrC/ZrO_2 interface after 1-hour exposure to MO at 800°C [5].

The images reveal three distinct regions: the unoxidized ZrC core, an intermediate layer, and the fully oxidized ZrO_2 layer. The intermediate layer is partially oxidized, retaining a mixture of Zr, C, and O phases, and it contains cracks and porosity due to the escape of volatile byproducts such as CO or CO_2, which compromise the oxide layer's mechanical integrity. It is likely that these gases pass through existing porous pathways, limiting widespread damage to the outer scale at initial stages. The fully oxidized ZrO_2 layer resists tensile stresses during oxidation, but cracks when internal stresses accumulate. Energy Dispersive X-Ray Spectroscopy (EDS) (Figure 2.4b) confirms the coexistence of unoxidized ZrC, intermediate phases, and ZrO_2, with a distinct compositional transition at the ZrC/ZrO_2 interface.

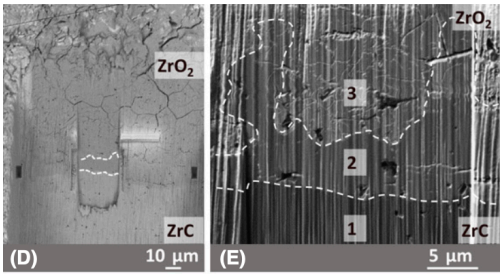

(a) SEI of (1) ZrC (2) intermediate layer (3) ZrO_2

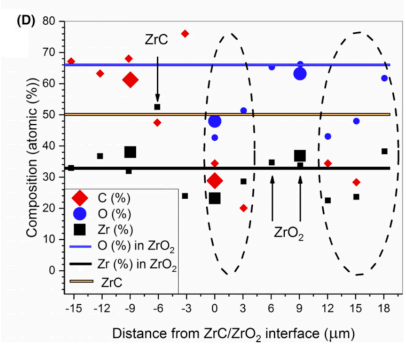

(b) EDS showing partial oxidation at interface

Figure 2.4: ZrC after 1 hour of MO exposure at 800°C [5]

The presence of an intermediate phase has been supported by multiple experimental observations and is especially evident under controlled oxygen pressures, where the reaction proceeds more uniformly, allowing a gradual progression from ZrC to ZrO_2. This behavior was captured and illustrated by Rama Rao & Venugopal in Figure 2.5, which shows a rapid increase in sample mass beginning around 550°C, with faster oxidation occurring at higher oxygen partial pressures. A reference line marking the theoretical mass gain for full oxidation reveals that the curves for 50 and 20 kPa plateau below this threshold, indicating incomplete oxidation and the formation of an intermediate layer. Interestingly, the curve for 5 kPa briefly exceeds the full oxidation limit before dipping back below it, which may reflect transient gas retention. Together, these deviations from ideal behavior support the existence of a nonstoichiometric intermediate, likely composed of zirconium oxycarbide (ZrC_xO_y) or ZrO_2 embedded in amorphous carbon [5] [24].

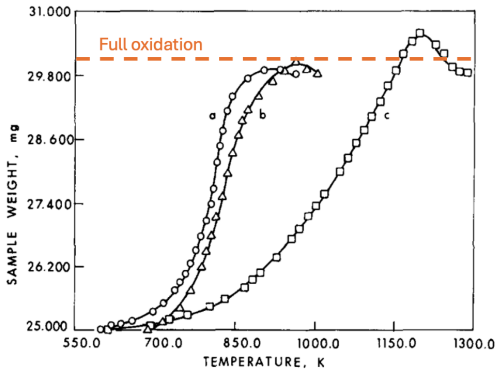

Figure 2.5: ZrC mass change at oxygen pressures (a) 50 kPa (b) 20 kPa (c) 5 kPa [24]

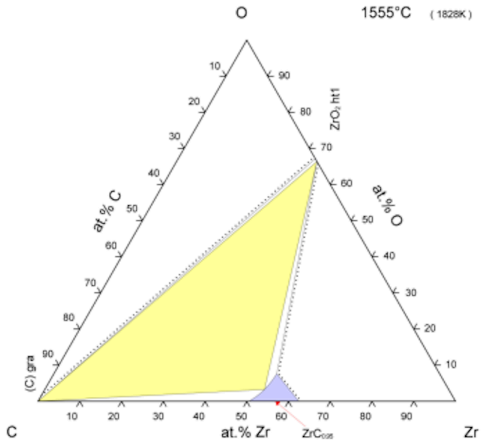

Figure 2.6: Phase diagram of ZrC_xO_y [29]

Figure 2.6 illustrates the stability and presence of ZrC_xO_y across a range of compositions up to 1555°C, coexisting with phases such as zirconia or free carbon. The size of the phase region indicates that ZrC_xO_y can accommodate a significant variation in oxygen and carbon content while remaining thermodynamically stable. This compositional flexibility supports its persistence as an intermediate layer under varying oxidation environments. Such stability may delay the transition to ZrO_2, offering a temporary barrier that moderates the progression of oxidation. However, oxygen incorporation into the ZrC lattice can also induce lattice distortions, weakening the protective oxide scale. Further research is required to determine how the extent of ZrC_xO_y stability influences the long-term structural integrity of oxidized ZrC systems.

Although further research on the formation of this intermediate layer did not take place in this study, its formation under the experimental oxidation conditions cannot be ruled out. The presence and characteristics of this intermediate layer could strongly influence how surface oxides respond to mechanical

strain during rapid cooling, thereby shaping the failure behavior investigated in later chapters. Its potential influence on oxide layer morphology, growth rate, and mechanical integrity was considered when interpreting oxidation behavior, and may warrant investigation in future work.

2.2.3. Zirconia Polymorphs

An essential factor in understanding oxidation behavior and mechanical degradation in ZrC is the evolution of zirconia polymorphs within the oxide scale. The stability and transformation of zirconia phases directly control not only oxidation kinetics but also how the oxide accommodates stress, resists cracking, and responds to thermal gradients or shock. This behavior is fundamental to how damage progresses during thermal exposure and cycling.

ZrO_2 exhibits three primary polymorphs: monoclinic (m-ZrO_2), tetragonal (t-ZrO_2), and cubic (c-ZrO_2). Each polymorph, visualized in Figure 2.7 has distinct stability ranges governed by temperature, grain size, and chemical environment. The formation of zirconia polymorphs is strongly influenced by thermal conditions and environmental factors, and each phase plays a distinct role in the material's oxidation behavior.

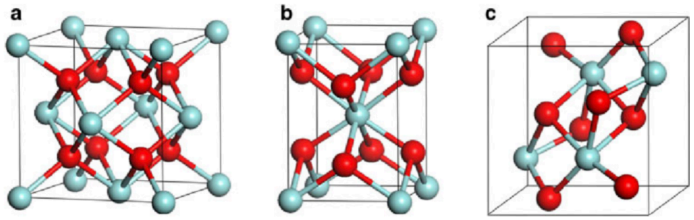

Figure 2.7: (a) cubic (b) tetragonal and (c) monoclinic zirconia microstructure [30]

Monoclinic ZrO_2 is the thermodynamically stable phase at moderate temperatures (below 1170°C) and typically dominates in undoped systems [5]. In contrast, tetragonal ZrO_2 is stable at higher temperatures but can persist metastably upon cooling if the oxide remains nanocrystalline, stabilized by grain sizes typically below 30 nm [31] [32]. Cubic ZrO_2 may also form transiently under certain non-equilibrium conditions, particularly in highly defective or nanocrystalline regions [33]. Furthermore, since most characterization methods, including XRD and Raman spectroscopy, are conducted at room temperature, the detected phases correspond to those stable or metastable after cooling, not necessarily those present at peak oxidation temperatures [31].

Within the moderate oxidation temperature range (600–800°C), literature suggests that oxide growth may initially favor fine-grained tetragonal ZrO_2, despite monoclinic being thermodynamically stable. This occurs because tetragonal, with its higher symmetry and lower surface energy, nucleates more readily than monoclinic, which introduces greater lattice distortion upon formation. Grain size effects further contribute to this behavior, as oxides formed under transient heating or rapid growth conditions often remain nanocrystalline, temporarily stabilizing the tetragonal phase [32]. However, as oxidation progresses, particularly toward the upper end of this temperature range, grain coarsening, defect reduction, and stress relaxation reduce the energy contributions that stabilize tetragonal, promoting transformation to monoclinic ZrO_2, which is thermodynamically favored below 1170°C [31]. The associated t→m transformation involves a volumetric expansion of approximately 3–5%, generating local shear stresses that frequently exceed the oxide's fracture toughness, leading to microcracking, delamination, and spallation [31].

The distribution and evolution of these polymorphs fundamentally govern how oxide morphology responds to oxidation temperature. High-temperature oxidation tends to favor dense, adherent oxide layers initially stabilized by t-ZrO_2, while lower-temperature oxidation produces porous, mechanically fragile oxide dominated by m-ZrO_2 from the outset. This polymorphic evolution directly influences not only oxidation kinetics but also the mechanical response of the oxide layer to thermal gradients and thermal shock, as discussed in subsequent chapters.

2.3. Thermal Shock and Cycling

While oxidation kinetics determine the stability and morphology of surface scales during high-temperature exposure, they also set the stage for how these materials respond to high thermal gradients.

2.3.1. Influence of Oxidation on Thermal Shock Resistance

Thermal shock in UHTCs causes damage through steep temperature gradients, which induce stress concentrations that exceed the intrinsic fracture toughness of brittle materials [4]. These stresses often result in surface cracks, spallation, and, in severe cases, complete structural fragmentation. Unlike ductile metals that can dissipate such stresses through plastic deformation, UHTCs lack this mechanism, leading to brittle and often catastrophic failure.

In oxidizing environments, thermal shock damage becomes more complex. The formation of surface oxide layers, particularly porous or poorly adherent ones like ZrO_2, introduces thermal expansion mismatches at the oxide–substrate interface. Porosity lowers the effective thermal conductivity and stiffness of the oxide, and it can also reduce the apparent CTE, leading to localized inhomogeneities in thermal strain [11]. As outlined in section 1.2, the CTE mismatch between ZrC and zirconia phases becomes particularly significant at elevated temperatures. The extent of this mismatch can be seen in Table 2.3. Upon rapid cooling, this mismatch generates tensile stresses that can lead to oxide delamination and subsurface cracking, accelerating structural degradation [6] [7] [34]. These stresses are further compounded by gas evolution during oxidation, where the release of CO and CO_2 can disrupt the surface through pitting, blistering, and material ejection [35]. Post-shock SEM observations frequently reveal these failure modes, underscoring their critical role in the degradation process.

Table 2.3: CTE of ZrC and ZrO_2 at room temperature and 1500°C

Phase	CTE at RT (×10^{-6} K^{-1})	CTE at 1500°C (×10^{-6} K^{-1})
ZrC [6]	∼4.0	∼9.0
m-ZrO_2 [7]	2.9 – 9.1 (anisotropic)	10 – 11 (anisotropic)
t-ZrO_2 [7]	10 – 11	12.4 – 14.2
c-ZrO_2 [8]	7.6 – 11.5	11.6

A number of studies have investigated these effects using rapid cooling methods like water quenching and forced gas flow, designed to replicate conditions encountered during space mission anomalies, engine shutdowns, or emergency re-entry events [21] [22] [36]. These protocols typically involve heating specimens to target temperatures (400°C–1900°C) followed by sudden exposure to ambient water or cold gas. However, the thermal shock behavior of monolithic ZrC has received little attention, as most research has concentrated on composite materials such as $MoSi_2$- and ZrB_2–SiC-based systems, which provide superior toughness and thermal shock resistance through reinforcement and crack-mitigating mechanisms.

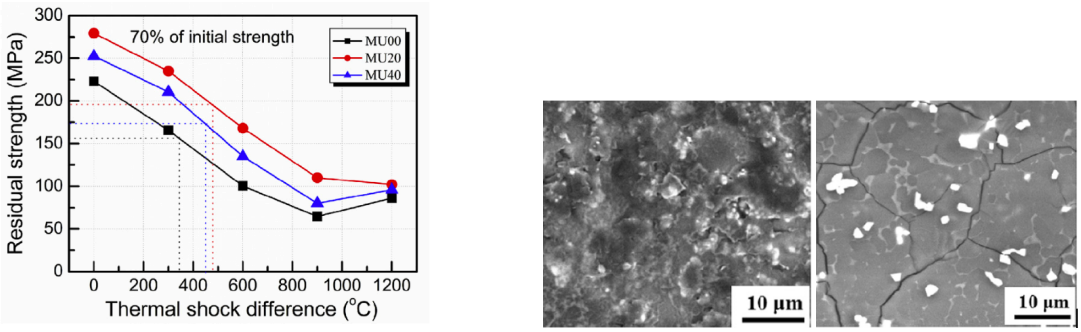

(a) Residual strengths after quenching from various temperatures **(b)** SEM images of MU00 after thermal shock at ΔT of 600°C and 1200°C

Figure 2.8: Thermal shock performance of $MoSi_2$-based UHTCs under water quenching [36]

Notably, one study from Zhang et al. investigated the thermal shock behavior of monolithic $MoSi_2$ (MU00) and $MoSi_2$-based UHTCs (MU20 and MU40) by heating samples to various temperatures in

air, holding for 5 minutes, and then rapidly quenching them in room-temperature water [36]. Post-quenching strength was evaluated using three-point bending, revealing a clear decline in residual strength with increasing thermal shock difference (ΔT), as shown in Figure 2.8a. At ΔT = 600°C, MU00 retained more than half of its initial strength, but at ΔT = 1200°C, the residual strength fell below 100 MPa. Since the damage mechanisms occur during the quenching process itself, the measured strength reflects a stabilized post-shock condition rather than a transient state. No significant time-dependent recovery or degradation is expected once the sample returns to room temperature. This loss of strength is further supported with SEM (Figure 2.8b), where surfaces with ΔT = 600°C exhibit smooth features consistent with oxide softening and partial crack healing, whereas ΔT = 1200°C results in extensive intergranular cracking and particle pull-out. These observations highlight how thermal shock damage in $MoSi_2$ is governed by the interaction of oxidation-driven mechanisms and thermal stress gradients.

Another study by Levine et al. evaluated the thermal shock response of ZrB_2-based composites by subjecting specimens to hydrogen-oxygen flame impingement at temperatures ranging from 1327°C to 1927°C, followed by nitrogen purge cooling [22]. The flame environment introduced not only high oxygen but also significant water vapor from combustion, both of which accelerate oxidation alongside thermal stresses. One tested material, composed of ZrB_2 + 14 vol% SiC + 30 vol% C (ZSC), was exposed to flame heating under progressively harsher conditions to assess damage evolution. As shown in Figure 2.9, the sample exhibited minimal visible damage after 5 minutes at 1327°C. However, after 75 minutes at the same temperature, surface roughening and localized discoloration appeared, suggesting the onset of oxidation or material degradation. The most extreme case, 180 minutes at 1627°C, showed severe charring, roughening, and non-uniform damage. These results visually demonstrate how prolonged high-temperature exposure, aggressive oxidative environments, and steep thermal gradients compound to accelerate surface degradation and structural damage.

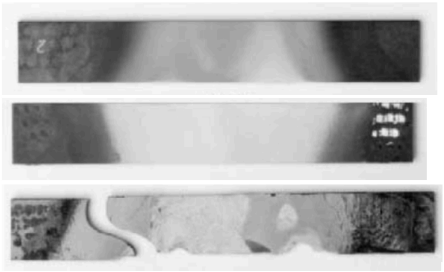

Figure 2.9: ZSC after thermal shock from: (top to bottom) 1327°C for 5 min, 1327°C for 75 min, and 1627°C for 180 min [22]

Modeling and experimental studies indicate that temperature differential alone is insufficient to predict thermal shock outcomes. Instead, the oxidation state prior to shock plays a decisive role. As highlighted in recent reviews, the formation, adhesion, and morphology of oxide scales directly influence crack initiation and propagation during rapid cooling [21]. This underscores the importance of characterizing the oxidation condition of UHTCs before thermal shock, as the initial oxide structure can strongly govern failure behavior under rapid or cyclic thermal loading.

2.3.2. Progressive Oxidative Degradation from Thermal Cycling

Although thermal shock failure in some UHTCs has been studied, the degradation mechanisms associated with repeated thermal cycling are less understood. In real-world aerospace applications, components are rarely exposed to a single extreme event. Most likely, they experience multiple thermal cycles during service, often under oxidizing conditions. These cycles can lead to progressive microstructural damage even when peak temperatures remain below critical shock thresholds.

Thermal cycling is known to exacerbate material degradation through subcritical crack growth, cyclic oxidation, and the accumulation of residual stresses. For ZrC, experimental evidence shows that oxidation in air between 800–1100°C leads to the formation of an intermediate layer that initially improves oxide adhesion [5]. However, at higher temperatures, this layer breaks down due to preferential carbon oxidation, forming CO and CO_2 and leaving behind a porous, unstable structure. This breakdown at the oxide–substrate interface may contribute to crack initiation or delamination during cycling.

One thermal-cycling study from Konnik et al. investigated ZrC oxidation from 1000–1600°C in air following pre-treatment in nitrogen [37]. Their results showed that oxide layer morphology varied significantly with temperature and exposure time. At temperatures above 1400°C, oxides were more compact and adherent due to the formation of tetragonal ZrO_2, which is stabilized by a combination of high temperature, accelerated sintering, and the retention of nanoscale grain sizes during rapid oxidation. On the other hand, lower-temperature monoclinic oxides were porous, mechanically unstable, and poorly bonded. This trend is visually evident in post-oxidation specimen images, where the sample oxidized at 1000°C disintegrated into powder, while those treated at 1200–1600°C retained dense, progressively darker oxide layers indicative of more stable morphologies Figure 2.10. These observations suggest that phase evolution plays a critical role in oxide integrity and its resistance to spallation or cracking during thermal cycling.

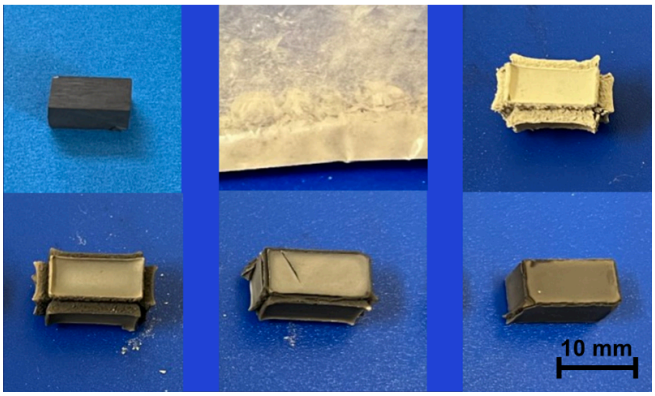

Figure 2.10: Top, left to right: unoxidized specimen, 1000°C, 1200°C. Bottom, left to right: 1400°C, 1500 °C, 1600°C. All oxidized specimens exposed for 40 minutes. [37]

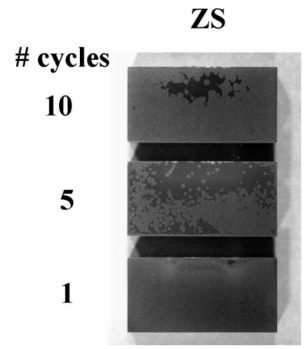

Figure 2.11: Oxidation of ZS UHTC at 1327°C in air under cyclic 10-minute exposures [22]

Additionally, the number of thermal cycles also plays a key role in determining the severity and character of oxide development. With each successive cycle, thermal expansion and contraction introduce repeated mechanical strain at the oxide-substrate interface, while repeated exposure to elevated temperatures promotes cumulative oxygen diffusion and scale thickening [5]. Studies have shown that early cycles with monolithic ZrC may only produce surface texturing or thin oxide films; however, after multiple repetitions, degradation mechanisms such as pore merging, interface debonding, and oxide embrittlement become more pronounced [38].

Further evidence for the degradation effects of repeated high-temperature exposure comes from a study by Levine et al. that examined ZrB_2–SiC–C composites subjected to multiple short oxidation cycles using hydrogen-oxygen flame impingement [22]. Samples were exposed to flame temperatures of 1327°C for 10 minutes per cycle, followed by nitrogen purge cooling. Progressive surface degradation was observed with increasing cycle count. As shown in Figure 2.11, the ZrB_2 + 20 vol.% SiC (ZS) composite exhibited minimal surface change after one cycle, but visible oxidation and surface discoloration appeared after five cycles. By ten cycles, widespread surface roughening, and non-uniform oxide formation were evident. Corresponding weight change measurements confirmed this trend, showing a steady increase in mass over repeated cycles due to cumulative oxide buildup. These observations highlight that even at a constant temperature, repeated thermal cycling at 1327°C drives progressive oxidation, surface instability, and mechanical degradation in ZrB_2-based composites.

Furthermore, a different study by Backman et al. conducted high-temperature oxidation experiments on high-entropy carbides (including Zr-containing systems) at 1500–1800°C using Joule heating under controlled oxygen partial pressures (0.1%–1%) [39]. Although not directly testing ZrC, their work highlights the strong temperature dependence of oxide morphology and the transition from porous to dense scales with increasing exposure temperature. Even short oxidation exposures (2–15 minutes) led to measurable material loss and surface evolution, indicating the potential for significant damage accumulation in thermally cycled systems. In particular, SEM cross sections of (HfZrTiTaNb)C samples oxidized for just 5 minutes in 0.1% O_2 at 1500°C, 1700°C, and 1800°C. Figure 2.12 revealed distinct differences in oxide morphology: at 1500°C, a thin, uniform scale formed with limited internal pene-

tration, while higher temperatures produced progressively thicker, more porous oxides and increased internal degradation. This observation suggests that rather than being purely surface-driven, degradation extends into the subsurface, likely compromising mechanical reliability, especially in mixed-metal carbides where diffusion pathways and strain mismatches are amplified. These images clearly demonstrate that even brief oxidation at elevated temperatures can significantly alter surface integrity and stress distribution, which are critical factors to understanding the performance of UHTCs under cyclic thermal loading.

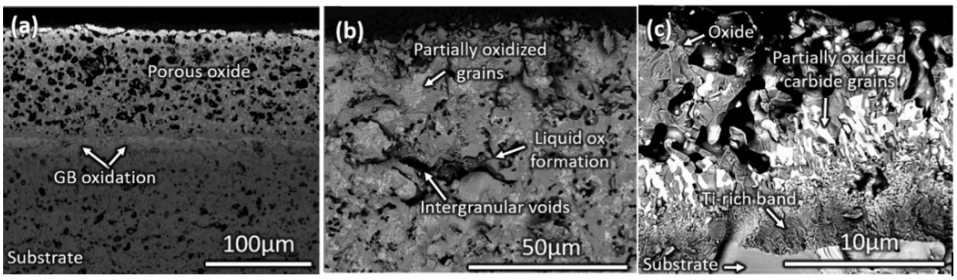

Figure 2.12: SEM images of (HfZrTiTaNb)C oxidized for 5 min at (a) 1500°C and (b) 1700°C, and 15 min at (c) 1800°C. [39]

Additionally, a foundational study by Shimada & Ishii demonstrates that ZrC is susceptible to oxidation even at relatively low temperatures (380–550°C) when exposed for extended durations ranging from 4 to 180 minutes [32]. Their results show that oxidation proceeds via diffusion-controlled kinetics after an initial rapid oxycarbide formation stage. Despite the mild temperatures, prolonged oxidation led to significant oxygen uptake and the formation of ZrO_2 alongside internal carbon accumulation. Above approximately 470°C, the oxidation-induced volumetric strain was sufficient to initiate cracking within ZrC grains, highlighting that even relatively moderate temperatures can drive meaningful degradation if exposure time is long enough. This observation reinforces that oxidation-related damage is not limited to high-temperature regimes but can accumulate progressively under milder thermal conditions, an important consideration for applications involving repeated thermal cycling or long-duration exposures below peak heating temperatures.

Taken together, these studies show that thermal cycling can degrade UHTCs by promoting oxide transformation, interfacial cracking, and eventual delamination. Particularly in monolithic systems, the absence of engineered reinforcement phases makes them more vulnerable to progressive damage under repetitive heating and cooling. Understanding how oxide growth and interfacial mismatch evolve with cycle count and temperature is essential for evaluating the long-term reliability of UHTCs in service.

2.4. Knowledge Gaps and Research Hypotheses

While UHTCs have been studied extensively for aerospace applications, much of the existing research has focused on fiber-reinforced or composite systems engineered for damage tolerance. In contrast, the behavior of monolithic ceramics, particularly ZrC, remains poorly characterized under combined thermal cycling and thermal shock conditions. This is a significant gap given the increasing interest in using structurally simple monoliths for applications where weight, predictability, and thermal resistance are critical.

Recent studies have clarified that temperature differential alone does not dictate thermal shock response. Instead, surface condition (including oxide scale morphology, thickness, porosity, and phase composition) plays a key role in determining how and where cracks form during rapid cooling. However, most prior work has either examined oxidation or thermal shock in isolation, with limited attention paid to how prior oxidation history influences subsequent mechanical degradation.

As reviewed in subsection 2.3.1, oxidation-induced surface features (such as interfacial voids, unstable intermediate layers, and porous ZrO_2 scales) contribute to crack nucleation. This is especially significant because these defects often form at size scales (ranging from nanometers to microns) comparable to the critical flaw sizes that can trigger cracking in brittle oxide layers [33]. Further, subsection 2.3.2 showed that even short-duration or cyclic exposures can produce significant oxide evolution. Yet, the

combined effect of short-term oxidation followed by thermal shock, particularly for monolithic ZrC, remains largely unexplored.

Furthermore, there is little consensus on the threshold oxidation conditions (in terms of temperature or time) at which oxide morphology shifts from being benign or protective to becoming structurally damaging. While surface analyses such as SEM, XRD, and Raman spectroscopy are commonly used to study post-shock materials, few studies have systematically correlated these features to oxidation temperature and shock-induced cracking in monoliths.

This thesis aims to fill this gap by evaluating how oxidation conditions influence the thermal shock response of monolithic ZrC. To guide the investigation, the following hypotheses are proposed:

2.4.1. Effect of Oxidation History on Thermal Shock Resistance

It is hypothesized that the severity of thermal shock damage in monolithic ZrC increases with prior oxidation temperature and duration due to the development of mechanically unstable oxide layers. This is because oxidation conditions directly influence both the thickness and microstructure of the oxide scale. Higher temperatures or longer exposures promote the growth of thicker scales and more porous morphologies, while also favoring the accumulation of stress-sensitive polymorphs like monoclinic ZrO_2 upon cooling. These characteristics reduce the structural integrity of the surface by introducing internal stresses, volume changes, and interfacial weaknesses, which in turn increase the likelihood of cracking, delamination, and mass loss during rapid cooling.

To investigate this, ZrC samples will be pre-oxidized under controlled thermal cycling conditions (ranging from 600°C to 800°C for 3 to 40 minutes) and subsequently subjected to thermal shock. The resulting damage will be characterized using SEM to assess crack density and oxide spallation, and XRD and Raman spectroscopy to evaluate changes in oxide phase composition and integrity. This approach enables direct evaluation of how oxidation history governs the thermomechanical performance of ZrC under extreme thermal gradients.

2.4.2. Influence of Oxidation Conditions on Damage Transitions

It is further hypothesized that there exists a critical oxidation threshold beyond which the nature of thermal shock damage transitions from mild to severe. Below this threshold, the oxide layer may remain thin, adherent, and relatively stress-tolerant. However, beyond a certain temperature–time exposure, the oxide structure may become increasingly defective through mechanisms such as t/c→m-ZrO_2 transformation, interfacial void formation, or layer stratification, leading to brittle failure during thermal shock.

This transition will be identified by comparing damage indicators across samples exposed to progressively harsher oxidation regimes, including short and long exposures at 600°C, and moderate exposures at 700°C and 800°C. Post-shock metrics such as increases in monoclinic phase content, visible cracking, spallation, or loss of oxide adherence will be used to identify when degradation shifts from benign to critical. By correlating these changes with oxidation history, the study seeks to define the boundary between safe and failure-prone thermal environments for monolithic ZrC.

3

Methodology

This study will involve a series of oxidative thermal cycling and shock experiments designed to simulate off-nominal mission scenarios. Experimental tests will be used to investigate how prior oxidation influences the thermal shock response of monolithic ZrC.

3.1. Materials and Sample Preparation

This section describes the fabrication method, material characteristics, and preparation procedures used for the ZrC specimens tested in this study.

3.1.1. Spark Plasma Sintering (SPS)

Spark Plasma Sintering (SPS) is an advanced powder consolidation technique that applies uniaxial pressure and a pulsed direct electrical current to rapidly densify materials. Unlike conventional sintering methods, SPS achieves high heating rates (up to 1000°C/min) and enables densification at lower temperatures and shorter holding times, minimizing grain growth and energy consumption [40].

For UHTCs like ZrC, which are notoriously difficult to densify due to their high melting points and strong covalent Zr–C bonds, SPS offers a significant advantage. Traditional sintering methods typically require temperatures exceeding 2200°C and long soak times, leading to severe grain coarsening and degradation of mechanical properties [41]. SPS overcomes these challenges through localized joule heating, spark discharges at particle contacts, and plasma-enhanced diffusion, producing fine-grained, highly dense ceramics with improved hardness, toughness, and thermal stability [42] [43].

For the ZrC specimens tested in this study, SPS was the ideal fabrication method because it reliably achieves relative densities exceeding 98% with minimal porosity, ensuring a fine-grained microstructure critical for resisting oxidation and thermal shock during high-temperature testing [41].

3.1.2. Sample Description

The material used in this study consists of monolithic ZrC specimens fabricated via SPS. The ZrC powder was sourced from Goodfellow (purity: 99.5%, particle size < 45μm) and was sintered using a two-step heating schedule, beginning with a hold at 1500°C, then ramping to 2000°C under a uniaxial pressure of 80 MPa for a final 10-minute hold. This process (visualized in Appendix A) produced dense ceramics with minimal porosity and fine microstructure, suitable for oxidation and thermal shock testing. The sintered specimens have masses ranging from 184.9 mg to 315.1 mg.

Due to time constraints, pre-fabricated and pre-polished samples from a prior experimental batch were used to maximize testing time. Minor variations in size and shape reflect the limitations of the available material, which may introduce some influence on oxidation kinetics, heat transfer, or stress distribution during thermal shock. However, all specimens were compositionally identical and geometrically similar, with care taken to ensure consistent orientation and placement during testing.

Prior to thermal cycling, all samples were cleaned in ethanol to remove surface debris. No coatings or surface treatments were applied to maintain the intrinsic behavior of the ZrC during oxidation and thermal shock. In future studies, the use of machined, geometrically identical specimens would reduce variability and allow for more rigorous mechanical and thermal comparisons.

3.2. Thermal Cycling Oxidation Procedure

Prepared ZrC samples underwent thermal cycling to induce controlled oxide scale formation.

3.2.1. Thermomechanical Analysis (TMA)

Thermomechanical analysis (TMA) is a technique used to measure the dimensional change of materials under controlled temperature variations. In TMA, a small, constant force is applied to the specimen while it undergoes a programmed heating or cooling cycle, allowing real-time tracking of expansion, contraction, or softening behaviors [44]. In the context of aerospace materials, TMA provides critical insight into how components respond to repeated thermal fluctuations, which are common in space environments [45]. By using TMA to simulate heating and cooling cycles within controlled lab settings, researchers can mimic some aspects of these thermal environments, identifying failure thresholds, oxidation-driven instabilities, and mechanical degradation pathways.

In this study, the PerkinElmer TMA was operated in ambient air, using its heating and cooling capabilities (–90°C to +900°C) to both thermally cycle and deliberately oxidize the ZrC specimens. This approach not only replicates thermal transitions similar to those encountered in hypersonic flight or atmospheric re-entry but also promotes the formation of oxide layers under controlled oxygen exposure. While the exact cooling rates and environmental pressures of real missions cannot be perfectly recreated, the controlled thermal cycling in air provides a representative screening of how monolithic ZrC behaves when subjected to coupled thermal and oxidative stresses. This enables the investigation of how prior oxidation history and repeated thermal stress influence the material's mechanical resilience under extreme aerospace conditions.

3.2.2. Testing Procedure

Oxidation was conducted through a series of controlled thermal cycles in air at varying high temperatures. As a reference, Figure 3.1 maps oxidative environments from previous studies as a function of temperature and total exposure time, highlighting a focus on high-temperature or long-duration isothermal conditions. In contrast, this work aims to investigate the unexplored regime of intermediate temperatures with short-duration cycling for ZrC. These conditions simplify post-shock analysis by preserving the oxide scale, yet still producing oxidation products relevant to TPS degradation. This approach addresses a gap in existing research which has overlooked oxidation behaviors under short, moderate thermal exposures. To implement these conditions experimentally, the thermal cycling schedule shown in Table 3.1 was designed within the operational constraints of the PerkinElmer TMA.

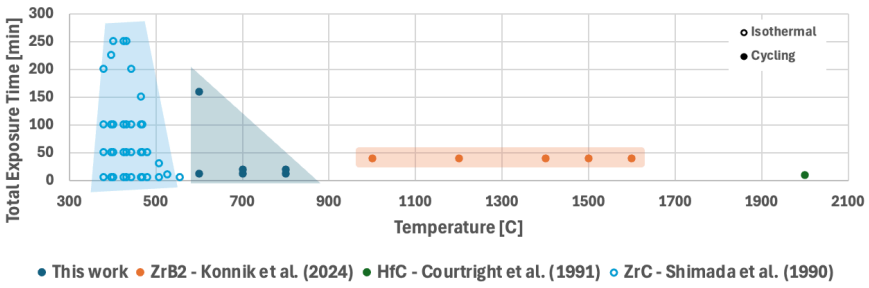

Figure 3.1: Temperature and exposure time of existing studies (including both cycling and isothermal holds)

Table 3.1: Experimental Matrix for Thermal Cycling

Sample	Low Temp.	Dwell Time - Low	High Temp.	Dwell Time - High	Total High Time
600-3	-70°C	3 min	600°C	3 min	12 min
600-40	-70°C	10 min	600°C	40 min	160 min
700-3	-70°C	3 min	700°C	3 min	12 min
700-5	-70°C	5 min	700°C	5 min	20 min
800-3	-70°C	3 min	800°C	3 min	12 min
800-5	-70°C	5 min	800°C	5 min	20 min

Each sample will undergo four complete thermal cycles, alternating between the designated low and high temperatures. This approach enables controlled oxide growth through repeated exposure, while remaining within the TMA's operational constraints and ensuring the procedure can be completed within a practical timeframe. Based on the findings discussed in subsection 2.3.2, even a small number of cycles can lead to visible changes in oxide morphology, including roughening, porosity, and the onset of delamination [22]. Therefore, four cycles are expected to generate measurable surface evolution without inducing catastrophic spallation.

By selecting four thermal cycles, this study targets the transitional regime where oxidation products begin to significantly influence thermal shock response without inducing excessive surface degradation. This intermediate cycling level is intended to capture the onset of damage mechanisms (such as crack initiation, oxide fragmentation, and surface roughening) while maintaining sufficient structural integrity for post-shock characterization. A higher number of cycles would likely lead to severe spallation or delamination, complicating subsequent analysis. Observations from this controlled regime will clarify how oxidation history affects the shift from stable behavior to failure under rapid cooling, directly supporting the research objectives related to damage thresholds and failure mechanisms in monolithic ZrC.

Each cycle includes a consistent low-temperature soak at –70°C and a variable high-temperature hold between 600°C and 800°C. These high-temperature dwell times were selected to represent different levels of oxidation exposure, allowing for controlled variation in oxide thickness and surface morphology. The chosen conditions were guided by previous oxidation studies of ZrC which demonstrated that oxidation below 900°C typically avoids severe spallation (as evidenced by Yun-Ching Lin, unpublished work). This is critical, as extensive delamination or material loss prior to shock testing would obscure the effects of prior oxidation on thermal shock behavior.

The 600–800°C range offers an ideal window to capture the onset and evolution of oxidation without inducing catastrophic failure. Prior research has shown that even short exposures within this range can produce measurable surface changes, including preliminary oxide layer formation, grain boundary roughening, and oxygen ingress—all of which are relevant to understanding degradation mechanisms during thermal shock [38] [32]. In contrast, oxidation below roughly 500°C proceeds too slowly to yield significant microstructural changes in reasonable timeframes, while temperatures above 1000°C typically lead to rapid oxide scale growth, internal stress buildup, and surface spallation. These higher-temperature effects dominate failure modes and would interfere with the ability to isolate how more subtle oxidation histories influence subsequent cracking or delamination under rapid cooling.

To further ensure consistent oxidation development, a heating and cooling rate of 20°C/min was selected. This moderate ramp rate minimizes thermal gradients within the sample, promoting uniform temperature distribution and oxide scale formation during each cycle. In contrast, much faster cooling rates (as used in quenching studies) can introduce steep thermal gradients that drive localized cracking or oxide detachment unrelated to the oxidation history. By controlling both the thermal ramp and the cycle profile, this study aims to generate a range of surface oxidation conditions that remain structurally intact, enabling a clear correlation between oxidation exposure and thermal shock resistance.

3.3. Thermal Shock Procedure

Once the oxide scale is established through thermal cycling, the samples will be subjected to thermal shock to evaluate the shock resistance of the pre-formed oxide layers.

3.3.1. Tube Furnace

Tube furnaces are widely used in thermal shock testing due to their ability to deliver uniform, high-temperature heating under precisely controlled conditions. Equipped with a long alumina work tube, the Lenton PTF 16/75/610 tube furnace used for this study enables precise thermal processing with continuous operation up to 1550°C [46]. The three-zone design offers accurate control over heating rates, dwell times, and thermal uniformity, and it can be configured for use in controlled atmospheric environments. For thermal shock experiments, this uniform and stable heating is essential to ensure that specimens reach thermal equilibrium before rapid cooling, enabling consistent and reproducible testing of material response.

Additionally, the open-end design of the tube furnace makes it suitable for high-temperature sample

extraction, allowing users to quickly remove specimens from the hot zone and quench them in a cooling medium such as water. This setup provides the sharp thermal gradients needed to simulate extreme thermal shock events, such as those encountered in components during engine shutdowns, re-entry phases, or plume interactions, where cooling rates can exceed hundreds of degrees Celsius per second [47]. By enabling controlled and repeatable application of steep thermal gradients, tube furnaces play a critical role in assessing the crack resistance, spallation behavior, and overall durability of brittle ceramics and ultra-high-temperature materials subjected to severe thermal cycling.

3.3.2. Testing Procedure

After oxidation, each sample will be reheated in the tube furnace under an argon atmosphere to the same peak temperature used during its oxidation cycle (600°C, 700°C, or 800°C). Maintaining an inert argon environment is essential to prevent additional oxidation during this phase, ensuring that the surface oxide condition remains representative of its identified pre-shock state. Performing this step in air would alter the oxide morphology during reheating, making it impossible to isolate the effects of the original oxidation cycle.

After a 10-minute hold at the target temperature, which allows for thermal equilibration throughout the sample, each specimen will be rapidly extracted and quenched in room-temperature water. This abrupt temperature drop (580°C for 600-series samples, 680°C for 700-series, and 780°C for 800-series) induces high thermal gradients, generating internal stresses that simulate thermal shock. Observing the resulting surface damage and fracture behavior will provide insight into how prior oxidation influences the material's resistance to sudden thermal loading.

Although the specific thermal environments encountered during spaceflight may vary in terms of cooling medium, the use of water quenching remains a widely accepted method for simulating severe thermal shock in brittle ceramics. This approach allows for controlled, repeatable introduction of steep temperature gradients that approximate the rapid thermal transients materials face during events such as engine shutdowns, plume impingement, or atmospheric re-entry, which can exceed 300°C/s [34]. These conditions drive surface microcrack formation and strength degradation, which are essential metrics for evaluating thermal shock resistance. While not perfectly representative of in-flight conditions, this method enables conservative screening of material behavior under extreme gradients. Observing post-quench surface conditions (such as oxide spallation, crack morphology, or delamination) will help identify damage modes associated with different oxidation histories, directly supporting the core research questions related to failure mechanisms in oxidized ZrC.

Following each thermal cycle and shock, the specimens were analyzed to monitor oxide scale progression and to characterize its degradation.

3.4. Structural and Phase Analysis with XRD

XRD was used to identify surface phases in oxidized ZrC samples and assess the extent of oxidation resulting from thermal cycling. Measurements were performed using a Rigaku Miniflex 600 diffractometer operating at 40 kV and 15 mA, with data collected over a 2θ range of 20°–85°, a step size of 0.02°, and a scan speed of 1.2°/min. Table 3.2 lists the characteristic 2θ positions and corresponding lattice parameters for ZrC, polymorphs of ZrO_2, and amorphous carbon. Because the diffraction signal is sensitive to the phases present, it directly reflects how oxidation has progressed over repeated exposures.

Table 3.2: Diffraction angles for various Zr- and C- based phases

Phase	Avg. 2θ Positions (°)
ZrC [48]	33.0 - 38.3 - 55.3 - 66.0 - 69.3 - 82.0
Monoclinic ZrO_2 [49]	24.2 - 28.2 - 31.4 - 40.8 - 45.0 - 50.0 - 55.6
Tetragonal ZrO_2 [49]	30.2 - 35.3 - 50.4 - 60.1
Cubic ZrO_2 [50]	30.3 - 35.1 - 50.5 - 60.2
Amorphous Carbon [51]	35 - 43 (broad)

3.4.1. Phase Identification

During phase identification, one thing to note is that the diffraction peaks of tetragonal and cubic ZrO_2 are notoriously difficult to distinguish due to their close proximity in 2θ, particularly around 30°, 35°, and 50°, where both phases exhibit strong reflections from similar crystallographic planes. This overlap is especially problematic in systems with nanocrystalline domains or metastable phase retention, where peak broadening further obscures subtle differences in lattice parameters [31] [33]. As a result, conventional laboratory XRD lacks the resolution to reliably separate these two polymorphs under such conditions. Therefore, tetragonal and cubic zirconia are grouped together as a combined t/c-ZrO_2 phase for analysis. This approach is consistent with prior literature, which highlights the limitations of standard XRD in distinguishing between the two without the use of complementary techniques such as synchrotron radiation or Rietveld refinement with highly accurate structural models [5] [31] [33].

Additionally, amorphous carbon can appear in oxidized ZrC samples due to residual carbon left behind during oxidation. Moderate-temperature oxidation (600–800°C) may not fully consume this carbon, especially if protective oxides limit gas diffusion. Crystalline graphite shows sharp XRD peaks, while thermally degraded or disordered carbon appears as broad humps. Identifying these carbon phases is important for understanding the material's thermal and mechanical behavior after cycling.

To identify phases, Rietveld refinement was performed using Profex software, which iteratively fits simulated diffraction patterns to experimental XRD data [52]. This method adjusts structural parameters (including phase fractions, lattice constants, and peak profiles) to minimize the difference between the measured and calculated patterns. The primary output of interest in this study is the phase-specific weight percent, which Profex estimates based on peak intensities and unit cell information from the reference structures. The software evaluates the quality of fit using statistical indicators such as the goodness of fit (GOF), R-factors, and weighted profile residuals. In systems like ZrO_2, where tetragonal and cubic phases have highly similar peak positions and overlapping features, Profex may struggle to resolve them unambiguously. In such cases, slight differences in profile shape and relative intensity are used to distribute the fit between the two phases, but the results should be interpreted cautiously. This ambiguity reinforces the need to report t- and c-ZrO_2 as grouped values when necessary and to complement XRD with other techniques for definitive phase identification.

3.4.2. Assumptions and Limitations

While phase identification is based on ideal assumptions (such as perfect crystallinity, uniformly spaced lattice planes, and purely elastic scattering) real-world conditions often deviate from these ideals. Surface roughness and the presence of mixed or poorly crystalline phases can all contribute to shifts in peak position or width and variations in intensity. Additionally, due to the small geometry of the samples in this study, the x-rays interact not only with the specimen but also with the sample holder, introducing background noise and reducing peak amplitudes. Despite these limitations, characteristic peaks remain distinguishable and sufficient for drawing phase-related conclusions.

It is also important to note that XRD is a surface-sensitive technique, typically probing only the top few microns to tens of microns, depending on the material and the incident angle [53]. This means that the phase information collected through XRD reflects only the outermost oxidized layer, not the full bulk composition of the sample. As a result, the XRD data primarily captures the structural evolution of the oxide scale rather than any internal gradients or unreacted core material that may persist beneath the surface. While this surface-specific insight is critical for understanding oxidation kinetics and thermal barrier degradation, it also implies that deeper oxidation effects or sub-surface phase transformations may go undetected. Therefore, interpretation of the XRD results should focus on surface transformation and be supplemented by cross-sectional or bulk analysis methods where necessary.

3.4.3. Interpretation of XRD Data

To evaluate oxidation progression and surface phase evolution, XRD patterns will be interpreted by tracking changes in peak intensity, peak positions, and peak shape. A decrease in ZrC peak intensity will be taken as evidence of surface degradation and consumption of the carbide phase. Concurrently, the emergence or growth of peaks corresponding to t- and c-ZrO_2 will suggest oxidation product formation, with the presence of t/c-ZrO_2 indicating possible metastable phases retained from high-temperature oxidation. If significant m-ZrO_2 content appears, it will imply a transformation from

t/c-ZrO_2 upon cooling, particularly in the absence of stabilizing dopants.

Broadened peaks will be interpreted as an indication of nanocrystalline grain sizes or residual stress accumulation during oxidation and cooling [32] [31]. Peak broadening will also be used to infer microstructural changes such as grain refinement or defect formation. This approach is especially relevant given the known challenges of distinguishing overlapping zirconia polymorph peaks in oxidized samples.

3.5. Structural and Phase Analysis with Raman Spectroscopy

Raman spectroscopy was also used to identify and confirm the presence of zirconia polymorphs and assess the structural evolution of the oxide layer formed during thermal cycling. Raman analysis was conducted using a Renishaw inVia confocal Raman microscope, operating with a 532 cm^{-1} excitation source. Spectra were collected over the range of 100–2000 cm^{-1}, with an integration time of 10 s and an accumulation of 10 scans per point to improve signal-to-noise ratio.

ZrC is Raman-inactive under these conditions, so the analysis focused on oxide phases and carbonaceous products. The spectral window (100–2000cm^{-1}) was selected to capture both zirconia lattice modes (100–800cm^{-1}) and carbon features, particularly the D and G bands of amorphous carbon near 1350 and 1580cm^{-1}. These broad carbonaceous bands come from disordered, graphite-like carbon that lacks a regular structure, leading to wide, overlapping peaks in the spectrum [54]. The presence of these bands in oxidized samples indicates residual or segregated carbon following thermal exposure and highlights variations in oxidation completeness across samples.

Phase identification was performed by comparing measured spectra to literature reference peaks for the zirconia polymorphs and amorphous carbon (Table 3.3). Monoclinic zirconia exhibits sharp, well-resolved peaks arising from its low-symmetry lattice, while tetragonal and cubic forms present broader or overlapping bands due to higher symmetry and limited vibrations [50]. However, cubic ZrO_2 is often difficult to detect via Raman due to its low scattering cross-section and overlap with tetragonal peaks [55]. Although nominally Raman-inactive, c-ZrO_2 can exhibit weak signals when defects like nanocrystallinity, oxygen vacancies, or strain locally break symmetry. As a result, ambiguous features were interpreted as t/c-ZrO_2 when not clearly assignable to a single phase.

Table 3.3: Characteristic Raman peak positions ZrO_2 and amorphous carbon [51]

Phase	Raman Peak Positions (cm^{-1})
m-ZrO_2	177 - 190 - 223 - 307 - 336 - 382 - 476 - 506 - 539 - 615 - 640
t-ZrO_2	148 - 267 - 320 - 462 - 605 - 648
c-ZrO_2	246 - 303 - 444 - 617
Carbon	1350 - 1580

Beyond phase identification, shifts in Raman band positions provide insight into residual stress within the oxide layer. For t-ZrO_2, shifts of characteristic peaks to lower wavenumbers indicate compressive stress, while shifts to higher wavenumbers indicate tensile stress [55]. The opposite trend applies to m-ZrO_2 modes. This is particularly relevant because compressive stress stabilizes the tetragonal phase, while stress relaxation promotes transformation to the monoclinic phase, which is accompanied by volume change and can drive cracking, delamination, or porosity formation. In this work, such stress-related spectral shifts are critical for interpreting how prior oxidation influences oxide integrity and damage susceptibility during thermal shock.

3.5.1. Limitations and Assumptions

As with XRD, Raman spectroscopy is performed at room temperature, so only zirconia phases that remain stable or metastable upon cooling can be detected [5]. Under the moderate oxidation temperatures used and in the absence of stabilizing dopants, monoclinic ZrO_2 is expected to dominate. Tetragonal phases may persist if stabilized through grain size effects, while cubic ZrO_2 may also form transiently under certain conditions, particularly in highly defective or nanocrystalline regions.

Raman spectroscopy offers excellent surface sensitivity (top 1–2 μm), but it is influenced by surface

quality, optical alignment, and material anisotropy. Stress interpretation is inherently semi-quantitative, and polymorphs such as t-ZrO_2 and m-ZrO_2 may exhibit overlapping peaks. Despite these limitations, Raman spectroscopy remains a powerful complement to XRD, enabling localized phase identification, stress tracking, and evaluation of oxidation-induced structural change.

3.5.2. Interpretation of Raman Data

Real-world Raman spectra often deviate from ideal peak positions due to surface roughness, nanostructuring, internal stress, and the presence of amorphous phases. Interpretation must therefore account for not only the position and intensity of peaks, but also their width and symmetry.

In this study, peak broadening in Raman spectra is used as an indicator of structural disorder, fine grain size, and phase overlap, particularly within the oxide layer formed after thermal shock [54] [55]. Broadening arises from nanocrystalline grains, defects, and strain, which disrupt the long-range order required for sharp vibrational modes. Overlapping signals from multiple zirconia polymorphs can further obscure peak resolution. Additionally, subtle shifts in peak positions are used to qualitatively assess residual stress, where movement toward lower wavenumbers generally indicates tensile strain and movement toward higher wavenumbers suggests compressive strain [55]. This is especially relevant for interpreting spectral changes in monoclinic and tetragonal ZrO_2, where stress influences peak clarity, separation, and overall spectral symmetry. These features are critical for evaluating both the microstructural integrity and stress conditions of oxidized surfaces following thermal exposure.

3.6. Microstructural Analysis with SEM

To investigate the effects of thermal shock on oxidized ZrC, microstructural analysis was performed using SEM. This technique enables high-resolution imaging of surface and cross-sectional features, revealing critical details such as oxide layer morphology, microcrack formation, delamination, and degradation patterns linked to prior oxidation conditions.

Prior to SEM, samples were mechanically polished where necessary to expose cross-sections for through-thickness examination. Polishing was carried out in multiple stages using diamond suspensions: grinding with 3µm and 1µm DuraPol compounds, followed by final surface finishing using Chem OPS NonDry suspension to achieve a smooth, damage-free surface suitable for high-resolution SEM imaging.

3.6.1. Imaging Modes

Imaging was carried out using Low-Energy Imaging (LEI) and Compositional (COMPO) modes. LEI mode enhances topographic contrast by operating at lower accelerating voltages, making it particularly suitable for detecting fine surface features such as microcracks, surface roughening, or localized fragmentation in the oxide scale. This mode is valuable for identifying early-stage damage mechanisms that result from mismatches in thermal expansion or structural instability introduced during thermal cycling and quenching.

COMPO mode, which relies on backscattered electron (BSE) imaging, provides atomic number contrast that helps differentiate between heavier and lighter phases. In this context, it enables distinction between retained ZrC substrate and the overlying oxide layers. Changes in brightness can reveal the presence of monoclinic or tetragonal/cubic zirconia, as well as highlight voids, pores, or delaminated interfaces. Cross-sectional imaging with COMPO also assists in determining oxide layer thickness and uniformity, which are key indicators of oxidation progression and its impact on shock resistance.

The combined use of LEI and COMPO modes allows for both qualitative and semi-quantitative assessment of thermal degradation pathways. Features such as crack morphology, oxide adhesion, and phase contrast provide a spatial context to complement bulk-phase results obtained from XRD and Raman spectroscopy.

3.6.2. Limitations

While SEM provides valuable morphological detail, its interpretation is subject to certain limitations. Polishing can introduce artifacts or obscure fine surface features, especially near cracks or porous zones. In cross-sectional views, phase boundaries may be difficult to distinguish if compositional gradients

are subtle. COMPO imaging, while useful for detecting contrast between ZrC and oxide layers, cannot differentiate zirconia polymorphs without supporting phase analysis. Additionally, LEI and BSE resolution depends on imaging conditions, which may limit detection of very fine cracks or thin oxide scales. Despite these constraints, SEM remains a critical tool for linking observed damage features to thermal history, particularly when paired with XRD and Raman results.

3.7. Mass Change Tracking

To evaluate the progression of oxidation during thermal cycling, sample mass was recorded before and after each thermal cycle using a high-precision analytical balance. Mass change provides a simple yet powerful indirect metric for tracking oxidation kinetics, as oxygen incorporation into the ZrC lattice (primarily through surface oxide formation) results in a measurable weight gain.

In the temperature range explored in this study (600°C–800°C), the oxidation behavior of ZrC is expected to follow linear kinetics [23]. Studies have shown that ZrC oxidizes with a near-linear mass gain over time within this regime, indicating that surface reaction processes dominate rather than bulk diffusion. This linear mass increase supports the use of discrete mass measurements between thermal cycles to assess the extent of oxidation and the rate of oxide scale growth.

By tracking cumulative mass change across successive cycles, this method enables a non-destructive, cycle-by-cycle assessment of surface evolution. It serves to quantify how oxidation progresses under different thermal conditions (including peak temperature and dwell time), and to relate the degree of oxidation to observed changes in surface morphology and thermal shock resistance.

A consistent increase in mass across cycles would suggest stable oxide growth, while abrupt changes could indicate phase transitions, crack exposure, or the onset of porous oxide formation. Although mass gain alone does not reveal oxide microstructure or adhesion, it complements other characterization methods by providing a continuous, quantitative indicator of oxidation severity.

4

Thermal Cycling Results

Upon completing thermal cycling, the samples were examined to assess their oxidation states. As shown in Figure 4.1, distinct color variations provide a visual indication of each sample's oxidation history. The progressive lightening in color corresponds to increased oxidation. These preliminary visual cues are supported by further analytical evidence presented later in this chapter.

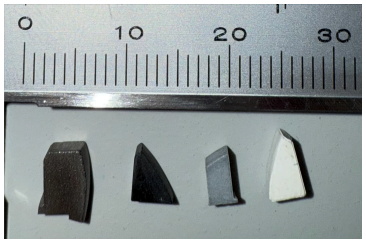

Figure 4.1: (left to right): unoxidized ZrC and oxidized Sample 600-3, Sample 700-3, and Sample 800-3

4.1. Mass Change After Thermal Cycling

One of the most basic indicators of oxide scale formation is the increase in mass. As described in section 3.7, oxidation is characterized by an uptake in oxygen, producing zirconia and adding weight to the sample. The rate at which this process occurs gives insight into the state of oxidation that is occurring. The mass change from the samples can be seen in Figure 4.2.

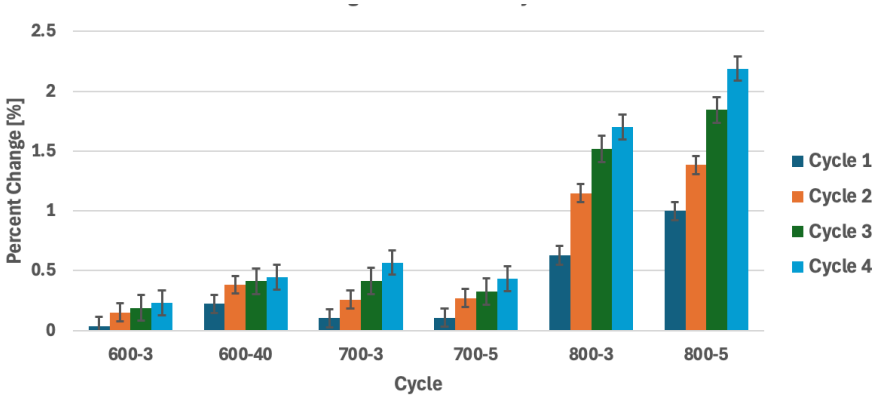

Figure 4.2: Changes in mass throughout 4 thermal cycles with respect to initial masses

Samples treated at 800°C, particularly 800-5, exhibit the highest cumulative mass increases, reflecting rapid oxide formation and continued oxygen uptake throughout the test. This is consistent with prior studies showing that ZrC oxidation is highly thermally activated, with higher temperatures substantially

accelerating the rate of oxide growth [31]. The steady increase in mass over successive cycles suggests that oxidation progresses efficiently across the thermal exposure window.

In contrast, the 700°C and 600°C samples show significantly smaller mass increases, indicating much slower oxidation rates under these conditions. This aligns with the lower thermal energy available to drive oxygen incorporation and zirconia formation, leading to thinner oxide scales and less cumulative mass gain over the same number of cycles [31].

Overall, the results clearly show that temperature strongly influences oxidation behavior, with higher temperatures producing greater mass increases and more extensive oxide growth, while lower temperatures result in slower and more limited oxidation.

4.2. Phase Composition After Thermal Cycling

The observations from mass change trends were further investigated through XRD-based phase composition analysis. Although all samples began as ZrC, progressive oxidation during thermal cycling led to the formation of various zirconia polymorphs, as evidenced by evolving diffraction patterns. These changes were tracked across cycles and oxidation conditions, revealing systematic shifts in surface phase composition. The spectra shown in Figure 4.3–Figure 4.5 illustrate the diffraction peaks corresponding to ZrC and the zirconia polymorphs for each sample from Cycle 1 through Cycle 4. Reference spectra for each phase are included to aid identification of dominant oxide products and transformation behavior. All patterns were refined using Rietveld analysis, with GOF values below 1.6 across all samples, indicating reliable phase quantification and overall good agreement between the measured and calculated patterns.

4.2.1. Phase Composition of 600-Series

In the 600-3 sample (Figure 4.3a), all four cycles exhibit prominent ZrC peaks near 2θ = 34°, 39°, and 61°, with minimal oxide peak development. This reflects limited surface oxidation during the short 3-minute exposure. The most changes occur after Cycle 1 as oxidation freely takes place on the surface without constraints. Only faint diffraction features for t/c-ZrO_2 are visible, and m-ZrO_2 is nearly absent. In contrast, 600-40 (Figure 4.3b) shows greater peak suppression of ZrC with increasing cycle number, and a concurrent increase in intensity for the oxide phases. Tetragonal and cubic peaks become more prominent after Cycle 2, and m-ZrO_2 features begin to appear around 28° and 31°, growing in clarity by Cycle 4. This suggests that prolonged exposure, even at a moderate temperature, leads to appreciable ZrC degradation and oxide scale thickening.

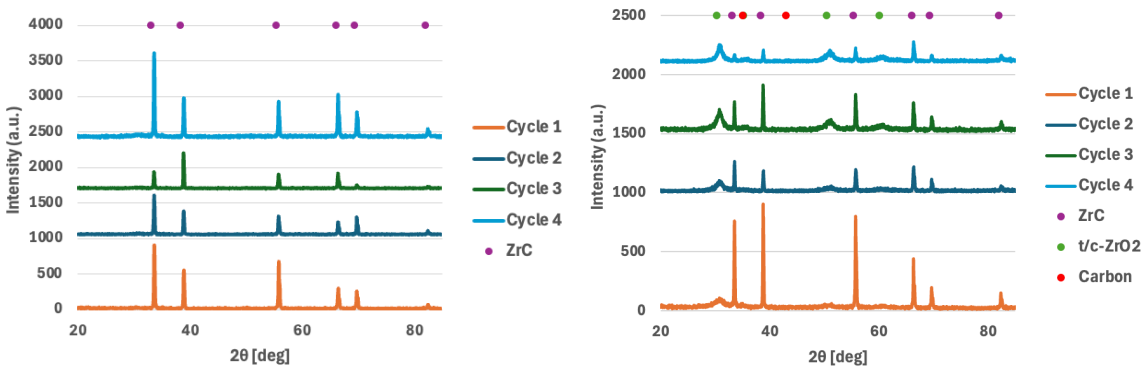

(a) Spectra of Sample 600-3

(b) Spectra of Sample 600-40

Figure 4.3: Phase analysis for 600-series samples

4.2.2. Phase Composition of 700-Series

At 700°C, oxidation becomes more aggressive. In 700-3 (Figure 4.4a), ZrC peaks are visible in early cycles but decline sharply by Cycle 4, indicating progressive consumption of the carbide phase. The oxide-related peaks, particularly for t/c-ZrO_2 near 30° and 50°, dominate the spectrum by the final cycle. These t/c-ZrO_2 peaks appear relatively broad, suggesting nanocrystalline or disordered grain structures

that stabilize the metastable phase. A low but growing m-ZrO_2 contribution is also seen, with slightly sharper peaks emerging, signaling the onset of phase destabilization and partial transformation.

For 700-5 (Figure 4.4b), the ZrC signals are even weaker, especially after Cycle 2, reflecting more extensive oxidation. The t/c-ZrO_2 features are sharp and intense, indicative of larger, more ordered oxide grains forming after prolonged exposure. Monoclinic peaks around 28° and 31° are more pronounced than in 700-3 and appear sharper as well, supporting the interpretation that longer oxidation durations enhance t/c→m transformation by relieving internal stress during cooling.

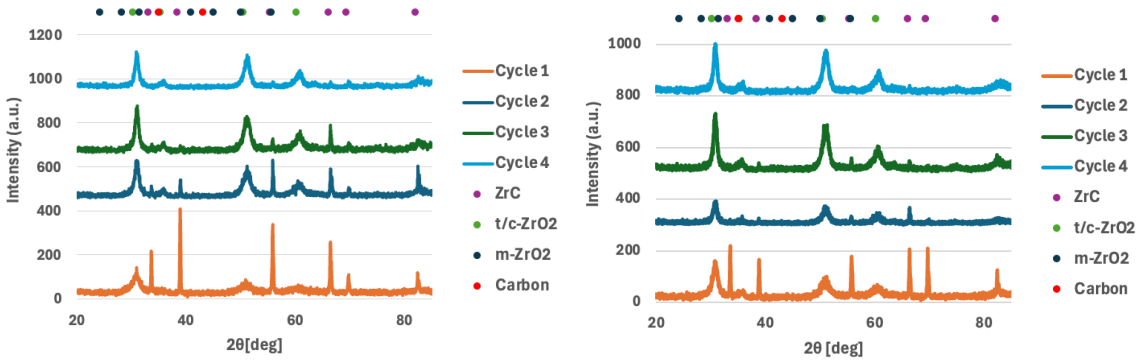

(a) Spectra of Sample 700-3

(b) Spectra of Sample 700-5

Figure 4.4: Phase analysis for 700-series samples

4.2.3. Phase Composition of 800-Series

The 800-series samples exhibit rapid and intense oxidation, with ZrC peaks fading after just one cycle and oxide peaks dominating the spectra. In both 800-3 (Figure 4.5a) and 800-5 (Figure 4.5b), m-ZrO_2 becomes increasingly prominent by Cycle 4, indicating progressive oxidation and transformation of high-temperature phases during cooling.

The early presence of t/c-ZrO_2 indicates initial stabilization via nanocrystalline effects, while the rise in m-ZrO_2 intensity across cycles reflects grain coarsening and stress relaxation. The broad nature of many oxide peaks suggests fine grain sizes, residual stress, or incomplete crystallinity typical of fast, diffusion-driven oxidation.

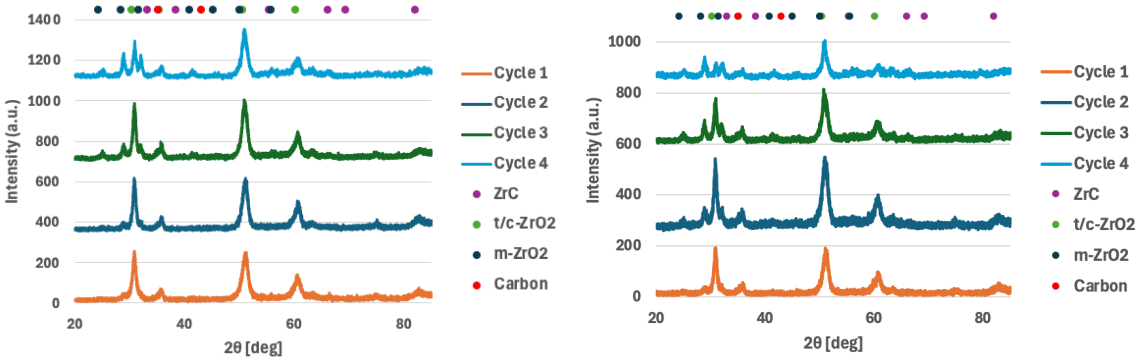

(a) Spectra of Sample 800-3

(b) Spectra of Sample 800-5

Figure 4.5: Phase analysis for 800-series samples

A closer look at phase-specific growth and depletion trends across cycles can provide a deeper quantitative basis for interpreting oxidation behavior.

4.2.4. ZrC Decline with Cycling and Temperature

As shown in Figure 4.6, ZrC content consistently decreases with both rising oxidation temperature and longer cycling duration. The 600-3 sample maintains over 90% ZrC across all cycles, reflecting limited oxidation at short exposure. In contrast, 600-40 begins to drop significantly after Cycle 2, and the 700°C and 800°C samples see near-complete ZrC loss by Cycle 4. This trend demonstrates the strong influence of temperature and time on surface carbide depletion.

The 700-series samples exhibit faster ZrC depletion, with both 700-3 and 700-5 falling below 10% by Cycle 4, especially in the longer-cycled 700-5. At 800°C, ZrC is nearly eliminated after just one or two cycles in both 800-3 and 800-5, confirming that oxidation is essentially complete at the surface under these conditions. This progression reflects a transition from stable carbide to fully oxidized surfaces as a function of increasing thermal exposure.

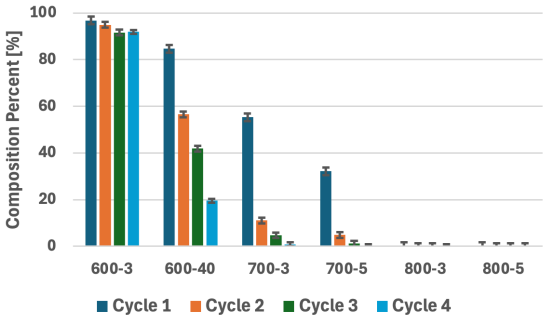

Figure 4.6: Surface evolution of ZrC composition over cycles

This loss of ZrC reflects the transition from a carbide-dominated surface to one where oxidation products dominate. The degree of ZrC depletion across cycles effectively tracks the progression of surface transformation and aligns with trends seen from section 4.1. Samples with minimal ZrC loss likely remain only slightly oxidized, while those with sharp reductions have undergone further oxide scale development.

4.2.5. Zirconia Polymorph Growth

While ZrC reduces in concentration, tetragonal and cubic zirconia dominate the oxide composition during intermediate oxidation stages, as shown in Figure 4.7. At 700°C, t/c-ZrO_2 content increases rapidly and stabilizes, becoming the primary oxide phase. In contrast, the 800°C series shows a rise in t/c-ZrO_2 followed by a decline, coinciding with increased m-ZrO_2 formation. This transition suggests that metastable t/c phases destabilize over prolonged high-temperature exposure, leading to a t/c→m transformation as the oxide layer matures.

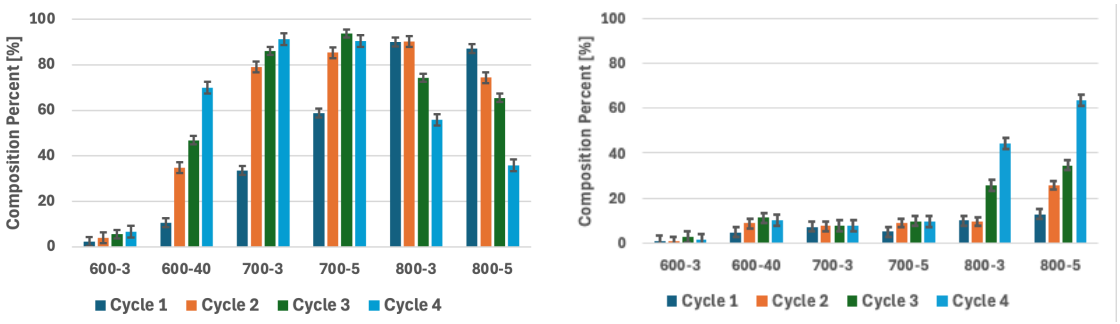

(a) t/c-ZrO_2 composition

(b) m-ZrO_2 composition

Figure 4.7: Surface evolution of zirconia polymorphs over thermal cycles

This progression from t/c-ZrO_2 to m-ZrO_2 reveals the impact of oxidation history on oxide phase stability. Initially, oxidation favors the rapid formation of nanocrystalline t/c structures, but as temperature and

duration increase, these phases destabilize and transform into the more thermodynamically stable monoclinic form. These results confirm that the oxide layer evolves continuously during cycling, rather than remaining static. As a result, the samples exhibit a controlled spectrum of oxide surface states (ranging from metastable to fully transformed) that can be systematically examined in the subsequent thermal shock experiments.

4.3. Phase and Stress Signatures After Thermal Cycling

Raman spectroscopy was employed to complement XRD analysis by providing surface-sensitive insight into the phase composition and structural evolution of the oxidized ZrC samples. As shown in Figure 4.8, the Raman spectra reveal clear trends in oxide phase formation across the temperature and time conditions used during thermal cycling.

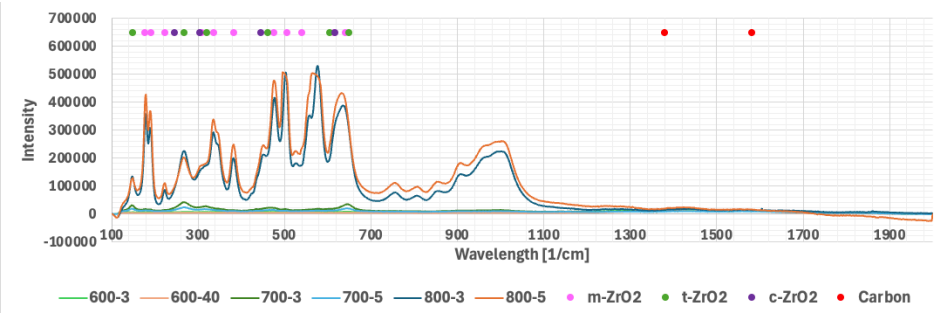

Figure 4.8: Raman spectra of all samples after thermal cycling

Samples exposed to 800°C exhibit the most intense and well-defined peaks for both m-ZrO_2 and t-ZrO_2. This indicates extensive oxide growth and phase transformation, supported by the long oxidation duration and high temperature. The high m-ZrO_2 intensity in 800-5 suggests significant transformation from metastable t/c-ZrO_2, likely driven by stress relief during cooling and grain coarsening, both of which destabilize the tetragonal structure. Additionally, a broad spectral feature near 1000 cm^{-1} is observed, attributed to Zr–O stretching in distorted or stressed oxide structures [54]. This signal likely results from residual strain introduced during the t/c→m transformation and thermal gradients, which distort bond angles and shift vibrational modes [55]. The 800-series also shows relatively stronger D and G bands, indicating residual or reorganized amorphous carbon. These carbon signatures are weaker or absent in lower-temperature samples, consistent with less extensive oxidation and carbon evolution.

In comparison, 700-series samples show moderate Raman intensity, with detectable but broader t/c-ZrO_2 and m-ZrO_2 peaks. This suggests partial oxidation and phase transformation, especially in 700-5, which displays slightly higher signal intensity than 700-3 due to its longer oxidation duration. The presence of weak D and G bands also reflects limited carbon restructuring. These results indicate that oxidation at 700°C initiates measurable surface transformation but may not fully transition to a diffusion-limited regime.

600-series samples display the weakest and least structured Raman spectra. Peaks are largely absent or broad, consistent with limited surface oxidation and the persistence of unoxidized ZrC, which is Raman-inactive due to its high symmetry. Even at extended durations (600-40), the oxide layer remains thin, as evidenced by low peak intensity and minimal carbon features. The absence of strong zirconia peaks supports the conclusion that these samples remain in a surface-reaction-limited regime.

Overall, these Raman results support and expand upon the XRD findings. They confirm that surface phase evolution intensifies with oxidation temperature and duration, leading to more defined phase separation, internal stress redistribution, and carbon reorganization. The dominance of t/c-ZrO_2 at early stages (stabilized by nanocrystallinity) is gradually replaced by m-ZrO_2 as higher thermal exposure drives grain growth and stress relaxation. The combined spectral trends reinforce that zirconia phase evolution and oxide structure complexity scale with thermal load.

4.4. Microstructural Analysis After Thermal Cycling

The development of the oxide scale was also seen through microstructural changes. Figure 4.9 shows the unoxidized surface of the ZrC samples as comparison.

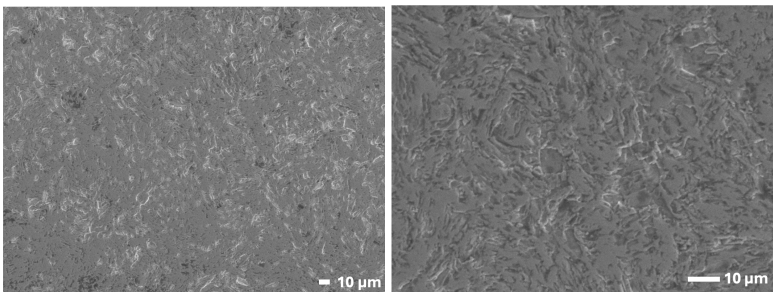

(a) 330x LEI surface image **(b)** 1000x LEI surface image

Figure 4.9: SEM images of ZrC samples prior to thermal cycling

4.4.1. Microstructure of 600-series

After four thermal cycles, the surface morphology of Sample 600-3 changed significantly, as shown in Figure 4.10. Compared to the unoxidized samples in Figure 4.9, thermal cycling introduced distinct dark spots and surface roughening. These dark features are likely residual carbon, which forms as a byproduct of the ZrC oxidation reaction; however, in this case, carbon remains solid rather than volatilizing at lower temperatures. This is especially plausible at 600°C, where oxidation is relatively slow, preventing complete carbon removal. The contrast arises because carbon, having a much lower atomic number than zirconia, appears darker under LEI conditions. Alongside these features, the surface also exhibits increased roughness and fine topographical changes, indicating that oxidation and thermal stresses have begun driving microstructural evolution and surface degradation during cycling.

The cross-sectional images presented in Figure 4.11 further support the observation that thermal cycling has driven microstructural evolution in Sample 600-3. The oxide layer remains relatively thin, consistent with low-temperature oxidation, but now exhibits interfacial roughening and layered contrast variations, indicating local differences in density or composition across the scale [37]. Notably, higher magnification reveals the presence of sub-surface discontinuities near the oxide–substrate interface, suggesting the onset of delamination or stress-induced microcracking. These features likely originate from repeated thermal expansion and contraction, which introduce cyclic tensile stresses at the interface [32]. The absence of full-through-thickness cracks implies that the scale remains partially intact, though its structural integrity has clearly degraded compared to the uncycled state.

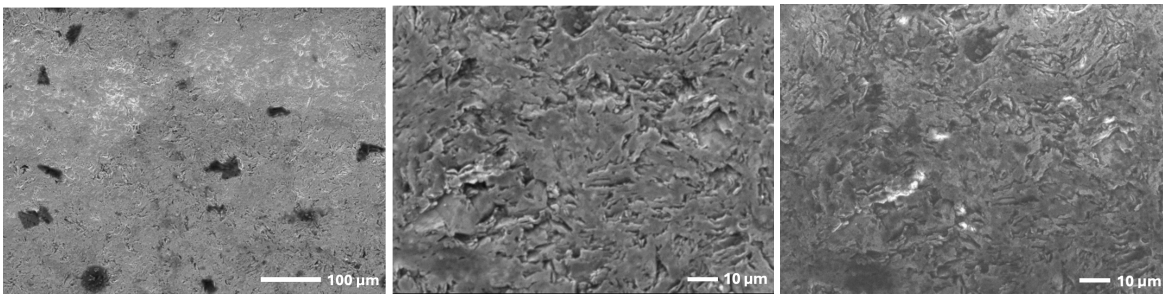

(a) 200x LEI image **(b)** 1000x LEI image **(c)** 1000x using SEI

Figure 4.10: Surface SEM images of Sample 600-3

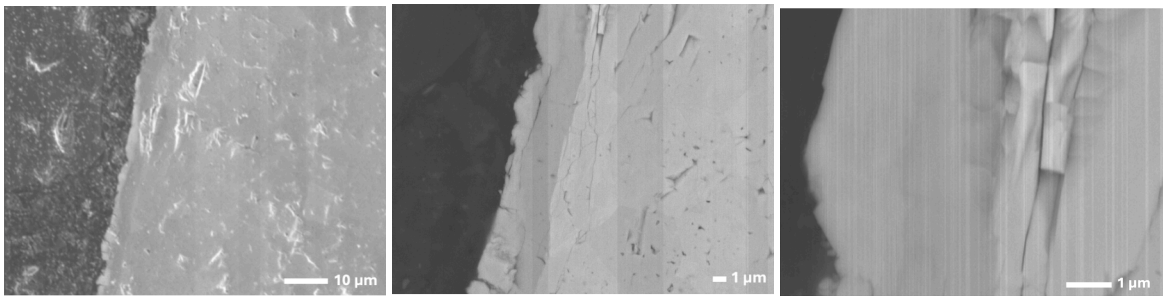

(a) 1000x LEI cross-sectional image **(b)** 3000x COMPO cross-sectional image **(c)** 11000x COMPO cross-sectional image

Figure 4.11: Cross-section SEM images of Sample 600-3

In contrast to Sample 600-3, Sample 600-40 reveals a more degraded surface (Figure 4.12). At low magnification, a higher density of the dark carbon-rich spots is evident, along with a generally rougher surface. This reflects more developed oxidation compared to the 600-3 sample because longer exposure allows for greater ZrC conversion to ZrO_2, which in turn produces more liberated carbon and increases the extent of surface restructuring. As the oxide scale grows, stresses from both volume expansion and mismatched thermal properties accumulate, driving the development of more pronounced topographical features. At higher magnification, the surface appears significantly more uneven and fractured, with sharp relief features and overlapping oxide layers. The disappearance of the wrinkled textures observed in Sample 600-3 suggests that the oxide has grown thicker and more rigid, shifting the material's response from elastic surface deformation toward brittle cracking and fragmentation [32] [31] [56].

The cross-sectional SEM images in Figure 4.13 reveal the internal consequences of more-developed oxidation and repeated thermal cycling in Sample 600-40. Compared to Sample 600-3, the oxide layer here is noticeably thicker and more structurally evolved, with well-defined boundaries and internal contrast gradients. Notably, a faint intermediate contrast zone can be observed between the bulk ZrC and outer ZrO_2, suggesting the formation of a transitional layer, possibly a compacted ZrO_2 region or an oxygen-enriched ZrC zone. The higher magnification images reveal straight, planar cracks that traverse significant portions of the oxide layer, along with localized voids and delamination zones, particularly near the mid-thickness and oxide–substrate interface. These features indicate that the scale has shifted from being stress-accommodating to stress-intolerant, responding to thermal strain through brittle fracture rather than elastic deformation. The appearance of a more uniform oxide morphology, coupled with crack propagation patterns, points to this critical shift in failure mechanism. This confirms that continued oxidation and thermal cycling cause the scale to lose mechanical compliance, promoting through-thickness cracking and setting the stage for potential spallation under further stress.

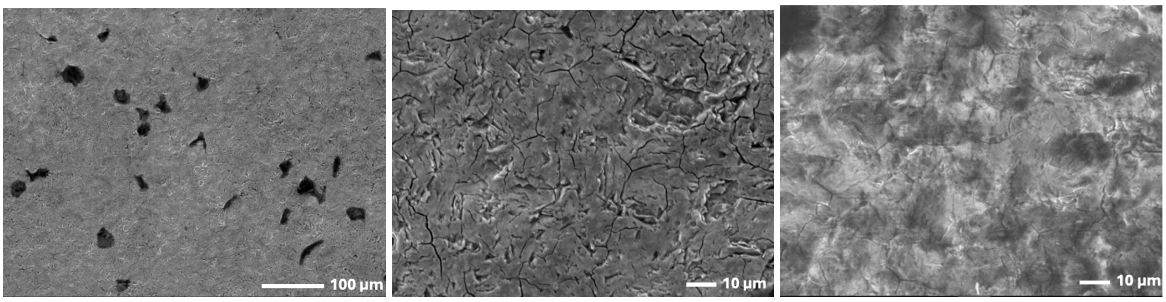

(a) 200x LEI image **(b)** 1000x LEI image **(c)** 1000x using SEI

Figure 4.12: Surface SEM images of sample 600-40

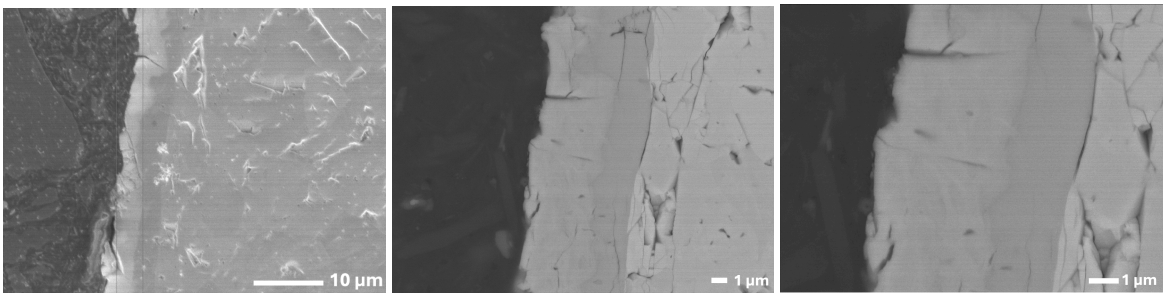

(a) 1800x LEI cross-sectional image **(b)** 5000x COMPO cross-sectional image **(c)** 9000x COMPO cross-sectional image

Figure 4.13: Cross-section SEM images of sample 600-40

4.4.2. Microstructure of 700-series

Degradation in Sample 700-3 is marked by the disappearance of carbon spots and the emergence of distinct surface microcracks (roughly 18µm), as shown in Figure 4.14. These seemingly intergranular cracks, along with the smooth oxide surroundings and continuous fracture paths in the compositional image, indicate a thick, brittle scale where fracture is the dominant stress-relief mechanism [32] [31] [56]. This further suggests the broader trend: as the oxide thickens and stiffens, stress accommodation shifts from elastic deformation to cracking. The absence of carbon spots at 700°C suggests that oxidation kinetics and internal stress accumulation have intensified, with compressive stresses exceeding the fracture threshold during cooling [37] [32] [31]. Thus, elevated temperature not only accelerates oxidation but also fundamentally alters how the oxide responds to thermal stress.

The cross-sectional SEM images in Figure 4.15 confirm the formation of a thick, continuous oxide scale in Sample 700-3, consistent with accelerated oxidation at elevated temperature. The oxide layer exhibits pronounced through-thickness cracks that extend toward the substrate, reflecting a brittle response to internal stress buildup during cycling. These cracks are straight and well-defined, with little evidence of crack deflection or energy dissipation, suggesting that the oxide has transitioned to a fully brittle regime. The intermediate contrast zone between the ZrO_2 and ZrC is even more clearly visible, supporting the formation of a transitional interfacial layer as oxidation progresses. Interfacial roughness and subtle void-like gaps along the substrate boundary indicate localized debonding, likely driven by thermal mismatch and phase expansion. Overall, the morphology confirms the shift in stress-relief mechanism from elastic accommodation to fracture-dominated failure.

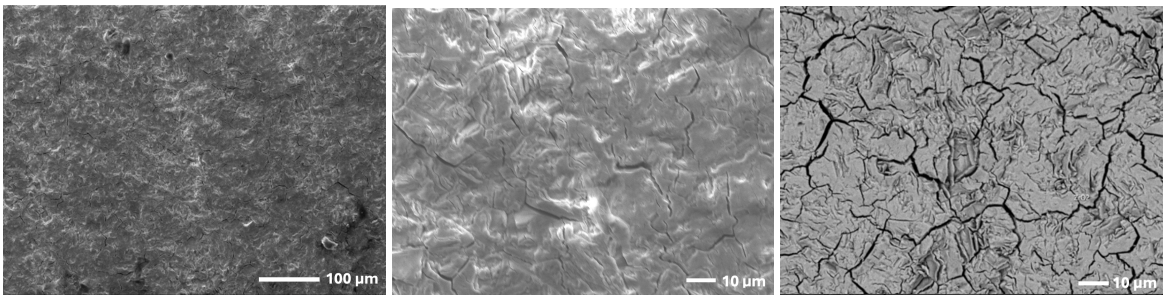

(a) 200x LEI image **(b)** 1000x LEI image **(c)** 1000x COMPO surface image

Figure 4.14: Surface SEM images of Sample 700-3

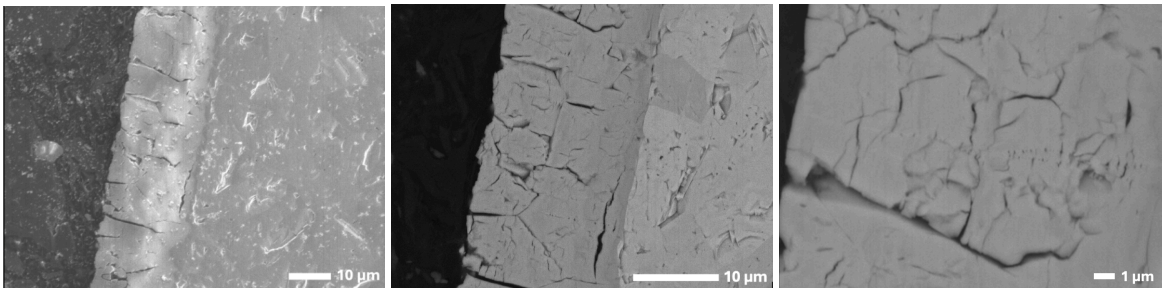

(a) 1000x LEI image **(b)** 2000x COPMO cross-sectional image **(c)** 5000x COMPO cross-sectional image

Figure 4.15: Cross-section SEM images of Sample 700-3

Sample 700-5 exhibits continued degradation following prolonged exposure at 700°C. As shown in Figure 4.16, the surface displays a more extensive and interconnected crack network than 700-3, indicating deeper fracture penetration into the oxide layer. This behavior reflects further thickening of the oxide scale and higher compressive stress accumulation during cooling, which drives more frequent fracture events [32] [31]. Low-magnification images reveal a uniformly textured surface, while high-magnification views show a relatively smooth oxide disrupted by dense cracking, evidence of a more brittle, developed scale. Although crack lengths remain comparable to 700-3, the increased density points to greater crack nucleation activity. These features confirm that fracture has become the dominant stress-relief mechanism, and that the oxide continues to grow with prolonged oxidation [32].

The cross-sectional SEM images in Figure 4.17 also show that Sample 700-5 developed a thicker, more fractured oxide layer than 700-3, consistent with its longer thermal exposure. The oxide scale displays interconnected through-thickness cracks and localized delamination, particularly near the interface. These cracks are sharper and more frequent than those in 700-3, confirming increased internal stress accumulation during thermal cycling. The intermediate contrast zone remains visible but is more diffuse, likely due to enhanced oxygen penetration or continued transformation of the interfacial region. Higher magnification reveals fragmentation and roughness within the oxide, suggesting widespread decohesion and reduced structural integrity. These observations indicate that with increasing time at elevated temperature, the oxide transitions to a fully brittle state, and fracture-driven stress relief becomes dominant, promoting progressive mechanical degradation under cyclic thermal loading.

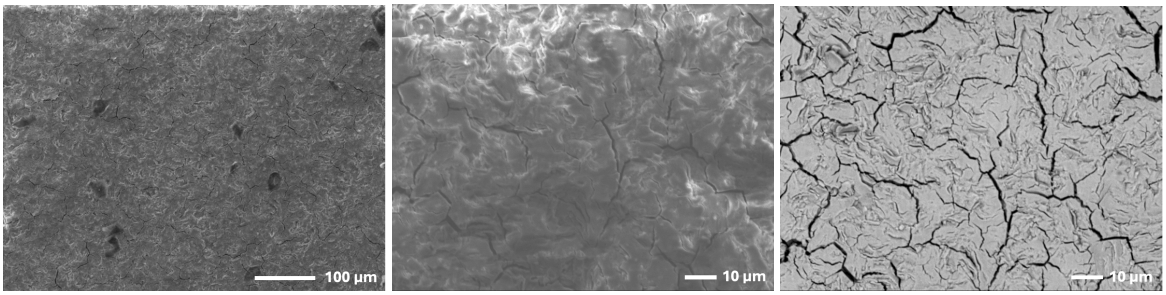

(a) 200x LEI image **(b)** 1000x LEI image **(c)** 1000x COMPO surface image

Figure 4.16: Surface SEM images of Sample 700-5

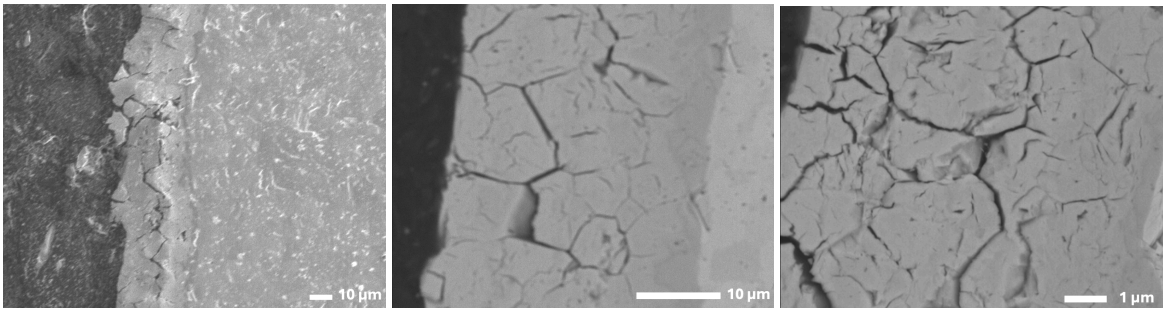

(a) 500x LEI cross-sectional image **(b)** 2000x COMPO cross-sectional image **(c)** 3000x COMPO cross-sectional image

Figure 4.17: Cross-section SEM images of Sample 700-5

4.4.3. Microstructure of 800-series

SEM images of the 800-series samples reveal an even more developed stage of oxidation-induced degradation. In Sample 800-3 (Figure 4.18), the oxide surface displays a dense network of wide and deep cracks, more numerous and interconnected than those observed in the 700-series. These features suggest significant scale thickening and the accumulation of high internal stresses during cooling, leading to fracture-driven stress relief. The overall surface morphology points to a brittle and mechanically compromised oxide layer, even after relatively short exposure at 800°C.

Cross-sectional images (Figure 4.19) confirm the severity of damage. Cracks extend through much of the oxide thickness, with some reaching near the ZrC interface. COMPO images show porous and fragmented regions along with partial delamination, indicating poor internal cohesion and weakened bonding at the interface. These observations demonstrate that brief high-temperature exposure is sufficient to generate a structurally unstable scale, prone to through-thickness cracking and interfacial failure under thermal stress.

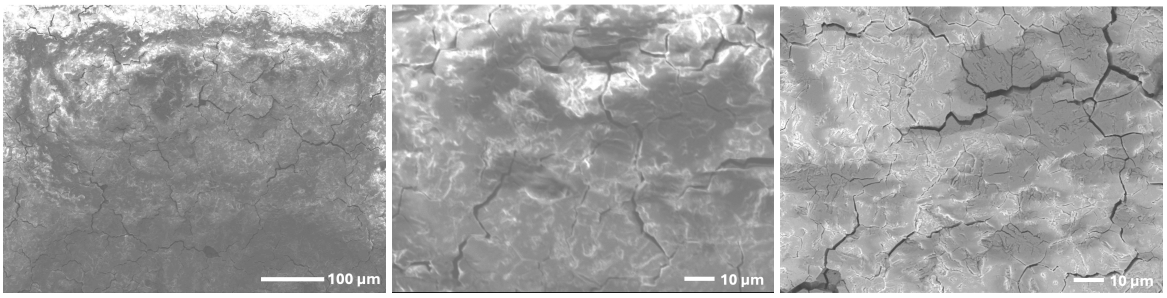

(a) 200x LEI surface image **(b)** 1000x LEI surface image **(c)** 1000x COMPO surface image

Figure 4.18: Surface SEM images of Sample 800-3

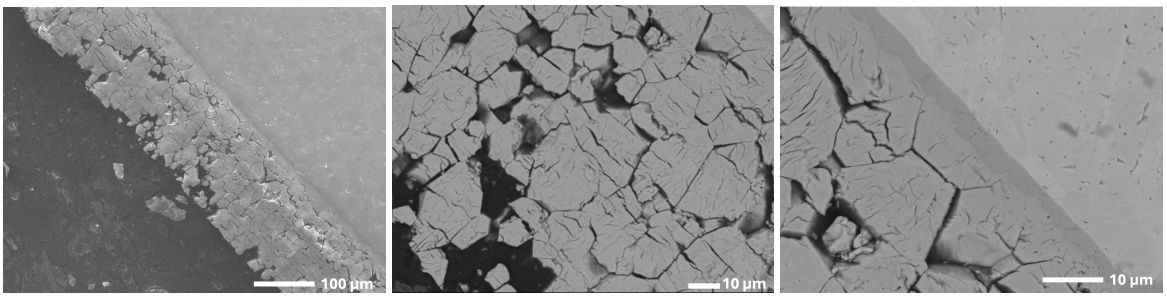

(a) 200x LEI cross-sectional image **(b)** 1000x Compo cross-sectional image **(c)** 2000x COMPO cross-sectional image

Figure 4.19: Cross-section SEM images of Sample 800-3

Sample 800-5 shows the most degradation from this study. Figure 4.20 indicates a heavily fractured and

roughened surface, with cracks distributed nearly uniformly across the field of view. The sharp, jagged cracks are both wide and numerous, with little evidence of intact regions between them, suggesting that the oxide layer has transitioned into a fully brittle regime. Compared to 800-3, 800-5 exhibits a more fully developed crack network, reflecting the longer oxidation exposure and thicker oxide scale. This suggests that under the combined conditions of high temperature and extended oxidation, the system reaches a stress state where crack nucleation and propagation become the dominant failure mechanisms, fully compromising the integrity of the surface layer.

Cross-sectional images (Figure 4.21) also reveal extensive through-thickness cracking and fragmentation. The oxide layer appears delaminated and porous in several regions, with cracks penetrating toward the substrate. These features suggest that internal cohesion has broken down, and the system has reached a stress state dominated by fracture-driven failure. Under prolonged oxidation at 800°C, crack nucleation and propagation become the primary stress relief mechanisms, severely compromising the structural integrity of the surface layer.

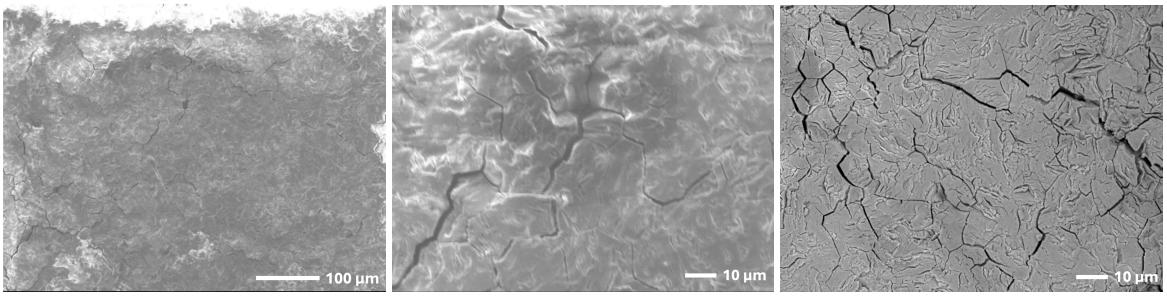

(a) 200x LEI surface image **(b)** 1000x LEI surface image **(c)** 1000x COMPO surface image

Figure 4.20: Surface SEM images of Sample 800-5

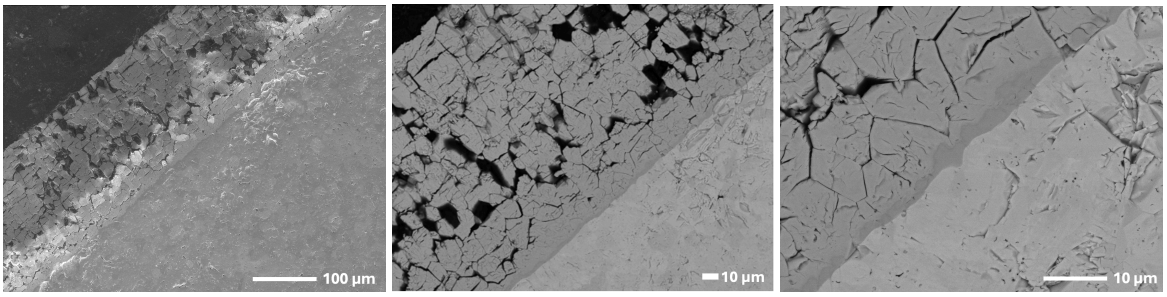

(a) 200x LEI cross-sectional image **(b)** 500x COMPO cross-sectional image **(c)** 2000x COMPO cross-sectional image

Figure 4.21: Cross-section SEM images of Sample 800-5

4.4.4. Microstructural Differences

The oxidation history, governed by temperature and exposure duration, played a key role in shaping the thickness, morphology, and mechanical behavior of the oxide layers. At lower temperatures, the 600-series samples developed thin oxides that were structurally underdeveloped and exhibited minimal internal stress. Cross-sectional images confirm these oxides were continuous but thin and compliant, with little evidence of delamination or cracking. This mechanical compatibility with the ZrC substrate likely reduced the risk of spallation or severe damage under thermal shock.

In contrast, the 700-series samples formed thicker, more evolved oxide layers. The longer exposure and elevated temperature promoted denser, stress-bearing scales. Cross-sectional data reveal an increasing presence of through-thickness cracks, interfacial roughening, and the emergence of a transitional intermediate layer. These features indicate a shift toward more rigid oxides that accumulate greater internal stresses during cooling, raising susceptibility to fracture once stress exceeds the oxide's mechanical tolerance. This trend aligns with the well-established relationship between oxidation kinetics and stress buildup in ceramics [4] [31].

At the highest temperature, the 800-series samples developed the thickest and most rigid oxide scales. The cross-sectional views show pervasive cracking, loss of phase cohesion, and widespread delamination, especially at the oxide–substrate interface. The intermediate layer becomes increasingly diffuse and indistinct, suggesting collapse or coalescence with the surrounding fractured oxide. These observations imply that high-temperature oxidation rapidly produces brittle, unstable scales with little residual compliance, setting the stage for catastrophic failure when subjected to thermal shock. Overall, the cross-section data reinforce that oxide evolution progresses from thin, compliant layers to thick, fracture-prone structures as oxidation advances with temperature and time.

To better assess the mechanical impact of oxide evolution, crack density was measured on both the sample surface and cross-section (Table 4.1). Surface and internal cracking both increased with oxidation severity, reflecting the buildup of residual stress in thicker oxide layers formed at higher temperatures. However, crack density plateaus in the most oxidized samples, suggesting that once a critical damage threshold is reached, further degradation may shift toward spallation or stress relaxation rather than continued crack accumulation.

Table 4.1: Crack density (surface and internal) of samples after thermal cycling

Image	600-3	600-40	700-3	700-5	800-3	800-5
Surface	2.25%	5.97%	6.49%	13.60%	13.97%	13.53%
Cross-Section	0.43%	2.00%	6.75%	8.48%	20.47%	17.75%

This trend reflects a transition in damage behavior: the 600-series oxides show primarily surface cracking, consistent with thin, compliant scales. In contrast, the 700- and 800-series exhibit much higher cross-sectional crack densities, marking the shift to a brittle failure regime where stored strain is released via deep fracture propagation. Although one might expect Sample 800-5 to show greater damage due to its longer oxidation duration, its slightly lower crack density may be explained by spallation. With a higher spallation concentration, Sample 800-5 likely released more of its surface oxide through detachment, effectively reducing the volume of fractured material captured in SEM analysis. This suggests that in more severely oxidized samples, damage may manifest as large-scale delamination rather than retained cracking. These results demonstrate a strong correlation between oxide growth, internal stress buildup, and mechanical degradation, confirming that thicker, more rigid oxides become increasingly prone to subsurface damage and structural failure under thermal cycling.

Complementing the crack density results, Table 4.2 quantifies oxide scale thickness and highlights the emergence of a two-layer structure at higher temperatures, consisting of a porous zirconia outer layer and a dense intermediate layer (as described in subsection 2.2.2). The outer layer thickens with both time and temperature. The intermediate layer, appearing in samples beyond 600-3, likely represents a compact transition zone between the porous oxide and the substrate. To account for non-uniform growth, thickness was measured at three representative locations per cross-section using the SEM ruler tool, and the average was reported.

Table 4.2: Oxide scale thickness after thermal cycling

	600-3	600-40	700-3	700-5	800-3	800-5
Outer Layer	3.469 µm	3.958 µm	18.750 µm	29.625 µm	143.802 µm	148.990 µm
Intermediate Layer	0 µm	2.269 µm	1.312 µm	3.422 µm	4.216 µm	3.414 µm

This layered architecture is typical of extended high-temperature oxidation, where oxygen diffusion and grain coarsening promote subsurface densification. However, no clear trend links oxide thickness to mechanical damage. For example, although 800-5 has the thickest scale, its internal crack density is lower than that of 800-3. Similarly, changes in intermediate layer thickness do not consistently align with crack severity. These inconsistencies suggest that while oxidation extent influences degradation, other factors govern how damage develops. As such, oxide thickness alone cannot predict failure risk, highlighting the complex interplay between oxidation history and mechanical response.

5

Thermal Shock Results

Once oxidized through thermal cycling, the ZrC samples were subjected to thermal shock to investigate how prior oxidation history influences their mechanical degradation under rapid cooling conditions.

5.1. Mass Change After Thermal Shock

Following thermal shock exposure, all samples exhibited a measurable reduction in mass (Figure 5.1).

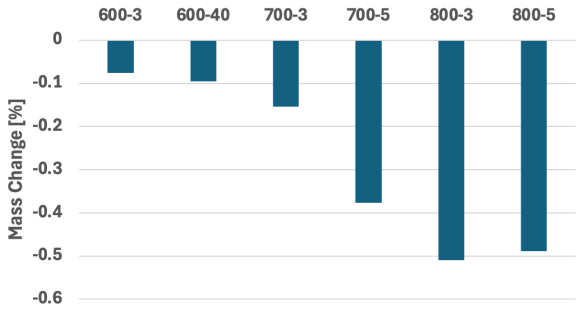

Figure 5.1: Mass change after thermal shock

This decrease in mass after thermal shock is likely attributed to the mechanical ejection or spallation of surface oxides, driven by the thermal expansion mismatch between the ZrC substrate and the oxide scale. The magnitude of this mass loss varied depending on the extent of prior oxidation and thermal exposure.

The largest reductions were observed in the 800°C samples, particularly 800-5, which lost approximately 0.5% of its mass. This correlates with the more advanced oxidation state of these samples prior to shock, suggesting that thicker or more continuous oxide layers are more prone to delamination when subjected to rapid thermal gradients [4]. The 700°C samples showed moderate mass loss, with 700-5 exhibiting a slightly larger decrease than 700-3, consistent with its greater pre-shock oxidation level and possibly reduced mechanical integrity of the oxide. In contrast, the 600°C samples exhibited minimal mass change, reflecting their limited oxide development during prior cycling. Their relative stability likely stems from the mechanical resilience of the ZrC substrate and the absence of a sufficiently thick oxide scale that could fracture or spall during thermal shock.

These results demonstrate that the extent of pre-existing oxidation plays a critical role in shock-driven material loss. More developed oxide layers, while necessary for oxidation protection, appear more susceptible to spallation under abrupt thermal gradients. Conversely, samples with thinner oxide scales experience less mass loss, highlighting the influence of oxidation history on structural resilience during thermal shock.

5.2. Phase Composition After Thermal Shock

After shock, the oxide layer was expected to undergo notable changes. Thermal shock introduces significant thermal stresses, which can trigger phase transformations or alter the material's morphology. These phase shifts and grain size variations are often detectable through XRD analysis.

5.2.1. Phase Composition of 600-series

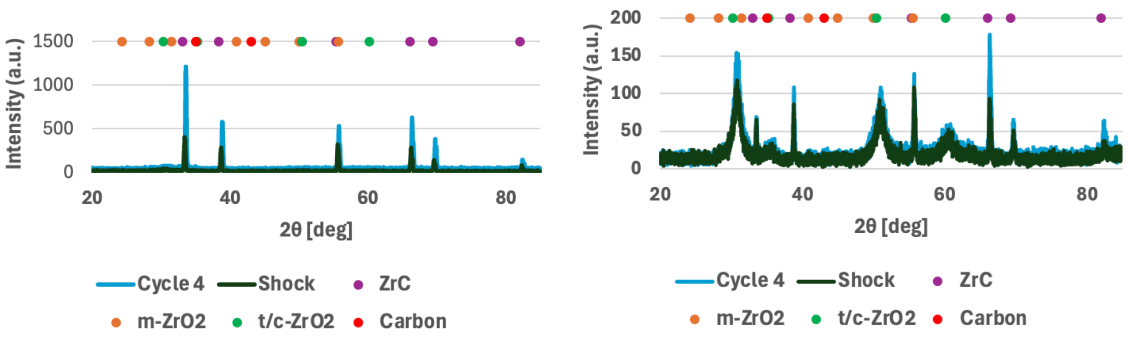

(a) 600-3 shock spectra comparison

(b) 600-40 shock spectra comparison

Figure 5.2: Shock comparison for 600-series samples

Following thermal shock, the 600-series samples showed small but observable shifts in phase composition. Sample 600-3, which initially underwent minimal oxidation and retained a high fraction of ZrC after cycling, experienced only a slight decrease in ZrC and small increases in t/c-ZrO_2 and m-ZrO_2. These changes, supported by subtle intensity differences in the XRD spectra (Figure 5.2a), suggest that even in relatively stable systems, thermal shock can trigger localized phase transformations, particularly encouraging the conversion of previously stabilized high-temperature oxides into m-ZrO_2.

In contrast, 600-40, which had already developed a thicker oxide scale by the end of cycling, showed more muted changes after shock. The ZrC content declined slightly, and moderate increases were observed in t/c-ZrO_2 and m-ZrO_2. The XRD spectra (Figure 5.2b) show some changes in oxide peak intensities but no signs of dramatic restructuring. This implies that most of the phase development occurred during the extended thermal cycling, with the shock serving only to redistribute or refine existing oxide features [4] [31] [37].

5.2.2. Phase Composition of 700-series

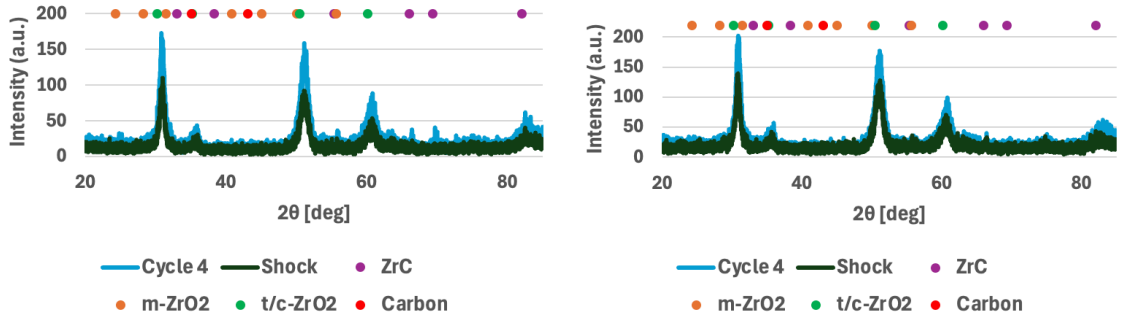

(a) 700-3 shock spectra comparison

(b) 700-5 shock spectra comparison

Figure 5.3: Shock comparison for 700-series samples

The 700-series samples, which were already more heavily oxidized by the end of cycling, also showed limited changes following thermal shock. For 700-3, ZrC remained nearly absent, and only minor redistributions occurred among the oxide phases. The XRD data (Figure 5.3a) point to a small gain in

m-ZrO_2 at the expense of the higher-temperature oxides, consistent with a localized t/c→m transformation driven by thermal shock stresses [4] [31] [37].

Sample 700-5, which had already reached a nearly fully oxidized state, exhibited negligible structural adjustments after shock. The spectra (Figure 5.3b) before and after treatment were nearly identical, indicating that the system had already stabilized, and the applied stress introduced no significant further transformation [31] [37].

5.2.3. Phase Composition of 800-series

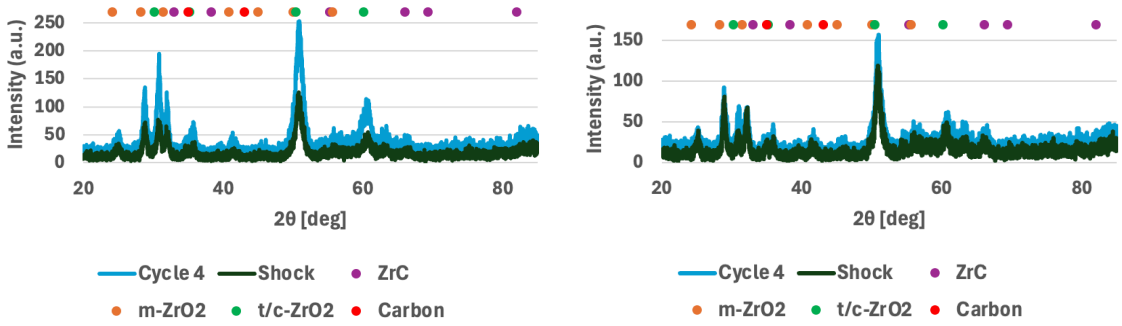

(a) 800-3 shock spectra comparison

(b) 800-5 shock spectra comparison

Figure 5.4: Shock comparison for 800-series samples

At 800°C, the combination of high temperature and severe oxidation history produced the most significant shock-induced phase shifts. For 800-3, which had nearly lost all ZrC during cycling, a very small reappearance of ZrC was detected, likely due to retained pockets or slight measurement fluctuation. The dominant oxide phases also shifted modestly: m-ZrO_2 increased while t/c-ZrO_2 decreased. These trends are reflected in the XRD spectra (Figure 5.4a), which show enhanced m-ZrO_2 peak intensities post-shock. This suggests that thermal shock promoted t/c→m transformation in the partially oxidized surface layer [31] [37].

For 800-5, already near-total ZrC depletion intensified post-shock. The small remaining amount of ZrC was eliminated, and a substantial increase in m-ZrO_2 was observed. Meanwhile, c-ZrO_2 content declined, and t-ZrO_2 remained steady. The spectra (Figure 5.4b) show strong m-ZrO_2 features post-shock, suggesting that under these extreme conditions, the shock helps lock the material into a stabilized monoclinic oxide state [31] [37].

5.2.4. Effects of Thermal Shock on Phase Composition

The post-shock XRD analysis across the samples reveals key trends in how thermal shock influences the phase composition and structural evolution of oxidized ZrC systems (Figure 5.5). While each series experienced different degrees of oxidation during thermal cycling, the application of thermal shock introduced stresses that altered the oxide structure to varying extents depending on prior damage state.

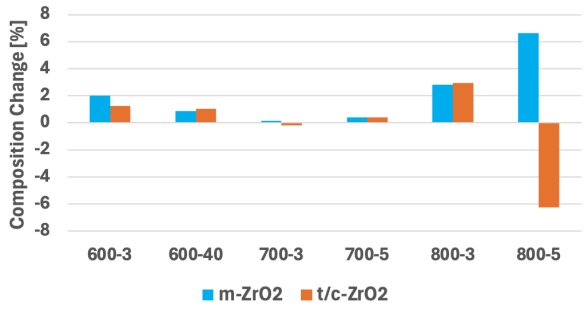

Figure 5.5: Surface evolution changes before and after shock

In the 600-series, both samples showed small but consistent increases in m-ZrO_2 and t/c-ZrO_2 content following shock. This suggests that even moderately developed oxide scales may still undergo minor stress-driven rearrangements from t/c→m. These increases in m-ZrO_2 reflect subtle transformation of metastable phases into more stable configurations under compressive stress during cooling, but it is unexpected that the t/c-ZrO_2 concentration also increases slightly. This may be a result of surface rearrangement, allowing a better signal of these phases to be detected.

The 700-series samples exhibited nearly negligible composition changes post-shock. Both 700-3 and 700-5 remained compositionally stable, with less than 1% change in either zirconia phase. This suggests that surfaces already near full oxidation are resistant to further transformation under thermal shock, likely due to stress relaxation already having occurred during the final oxidation cycles.

The 800-series samples showed the most pronounced evolution. In 800-3, both m-ZrO_2 and t/c-ZrO_2 content increased, with a notably larger rise in m-ZrO_2. This shift supports the interpretation that thermal shock at high temperatures promotes completion of the t/c→m transformation through stress-induced stabilization or grain coarsening. 800-5, in contrast, showed a large drop in t/c-ZrO_2 and a corresponding sharp increase in m-ZrO_2, indicating that any remaining metastable tetragonal/cubic content was fully converted under the extreme post-shock cooling conditions. This marks the final transition to a thermodynamically stable m-ZrO_2-dominated surface. This is so extreme in this sample likely because the stress was not high enough to induce complete transformations.

Less oxidized samples may only show minor redistribution, while highly oxidized systems, especially those near phase saturation, exhibit substantial stress-driven phase stabilization. These results emphasize the importance of controlling oxide maturity prior to shock exposure when designing materials for high-temperature applications.

5.3. Phase and Stress Signatures After Thermal Shock

Raman spectroscopy was employed to investigate the stress states, local bonding environments, and structural distortions within the oxide layers, providing complementary insights to the phase composition data obtained from XRD.

5.3.1. Phase and Stress Signature of 600-series

The Raman spectra of the 600-series samples (Figure 5.6) show minimal intensity and lack distinct peaks both before and after thermal shock. This is expected given that Sample 600-3 retained roughly 90 wt% ZrC after cycling, and Sample 600-40, while slightly more oxidized, still contained roughly 20 wt% ZrC. ZrC itself has a very weak or nearly undetectable Raman signal under standard conditions, as its metallic bonding character limits its Raman activity, and its low oxide content leaves little for detection [33].

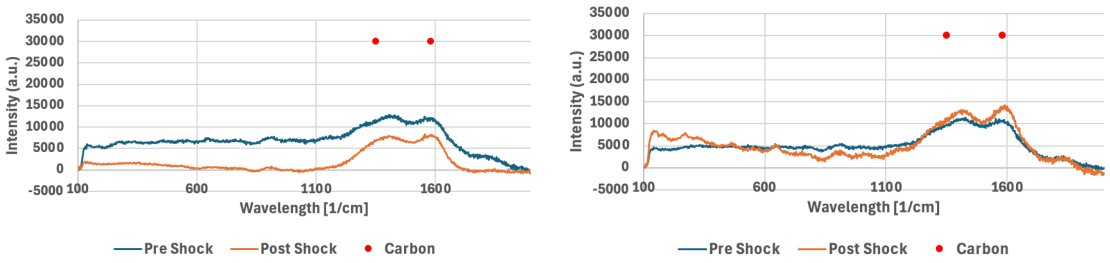

(a) Sample 600-3 **(b)** Sample 600-40

Figure 5.6: Raman spectra for 600-series samples before and after shock

Both pre- and post-shock spectra show broad, low-intensity D and G bands (1350 and 1580 cm^{-1}), indicating the presence of disordered or amorphous carbon near the surface. In Sample 600-3, the carbon signal decreases after shock, suggesting oxidation or surface disruption may have consumed or scattered near-surface carbon. In contrast, 600-40 shows a slight increase in carbon signal post-shock, likely due to surface cracking or roughening exposing residual carbon beneath the more developed

oxide layer. These trends highlight how oxidation duration alters both carbon retention and how it responds to thermal shock.

Notably, no distinct ZrO_2 peaks are observed in either sample, even post-shock. This suggests that the oxide content remains too low, nanocrystalline, or amorphous to generate detectable Raman signals. In 600-40, although XRD confirms some zirconia formation, its presence remains below the detection threshold for Raman analysis, possibly due to thin, poorly crystalline oxide layers or interference from the surrounding carbide matrix.

Importantly, the comparison between pre- and post-shock spectra shows no drastic changes, reinforcing the conclusion that thermal shock did not induce any detectable stress shifts, phase transitions, or structural reorganization in the 600-series. The nearly flat and featureless Raman baseline observed in both conditions aligns with the minimal structural damage seen in SEM and XRD. Together, these results confirm that the oxide layers formed at 600°C remain structurally compliant, with no measurable transformation or fracture signatures arising from shock exposure. The dominant contribution to the spectra remains from residual carbon, not oxidized zirconia.

5.3.2. Phase and Stress Signature of 700-series

The Raman spectra of the 700-series samples (Figure 5.7-Figure 5.8) show moderate but distinct spectral features both before and after thermal shock, reflecting the relatively more developed oxidation state compared to the 600-series. The presence of characteristic bands associated with t-ZrO_2 and m-ZrO_2 is evident, with sharper peaks and stronger intensities than in the low-temperature samples, indicating that the oxide layers formed at 700°C are both thicker and structurally more developed.

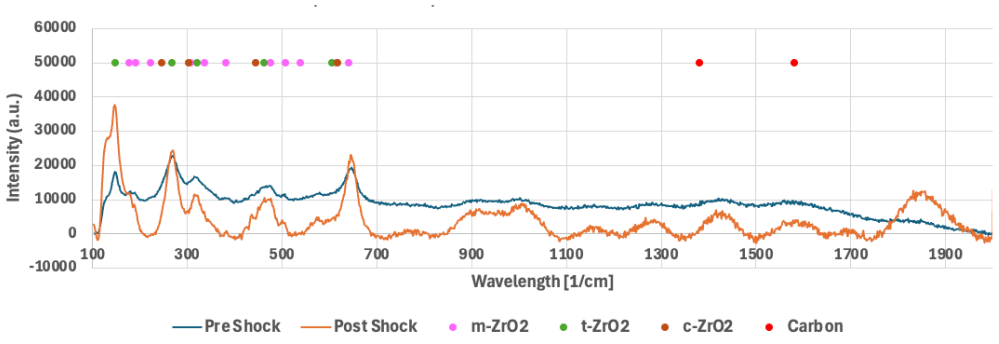

Figure 5.7: Sample 700-3 Raman spectra before and after shock

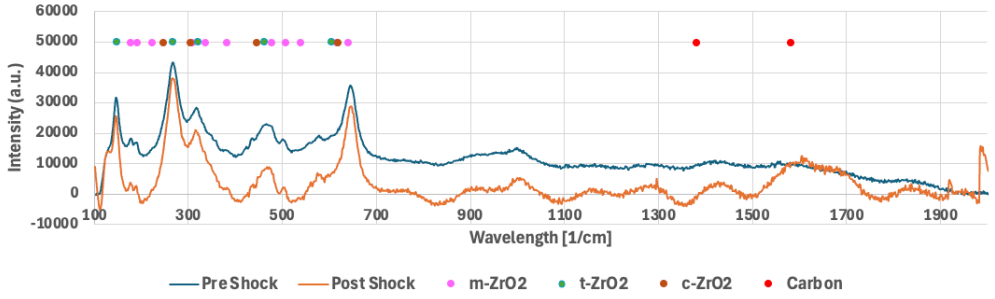

Figure 5.8: Sample 700-5 Raman spectra before and after shock

Sample 700-3, with a shorter oxidation time, shows clear oxide peaks alongside persistent D and G bands near 1350 and 1580 cm^{-1}, confirming the presence of disordered carbon. After thermal shock, the overall spectrum remains similar, although significant peak sharpening is observed, possibly due to densification or restructuring of the oxide. Sample 700-5 shows even stronger ZrO_2 peaks and slightly diminished carbon signals, suggesting further carbon oxidation or burial beneath a thicker oxide. The clearer oxide features and reduced baseline noise in 700-5 support the interpretation that oxide

layers grow more crystalline with longer exposure, while residual carbon diminishes or becomes less accessible to the laser.

The post-shock spectra for both samples exhibit no new major peaks, but the intensities and sharpness of existing bands slightly increase, consistent with structural rearrangement or stress reorganization rather than phase transformation. This is aligned with XRD results that showed minimal t/c→m transformation at this temperature.

The wavy spectral shape above 800 cm^{-1} in the 700-series samples likely results from combined contributions of amorphous carbon and oxide layer development. The broad D and G bands of disordered carbon create a characteristic dual-peak form that dominates this region, particularly in samples where free carbon persists after oxidation. Additionally, the more developed zirconia layers in these samples, especially post-shock, exhibit enhanced phonon scattering and potential second-order contributions, raising the spectral baseline [54]. These factors combine to produce a smooth, undulating profile shaped by overlapping vibrational modes and residual carbon rather than sharp, discrete peaks.

5.3.3. Phase and Stress Signature of 800-series

The Raman spectra of the 800-series samples (Figure 5.9-Figure 5.10) display strong and distinct peaks both before and after thermal shock, reflecting the fully oxidized nature of these samples. The spectra show characteristic bands corresponding to t-ZrO_2 and m-ZrO_2, with sharp features and high peak intensities, indicative of well-developed oxide layers.

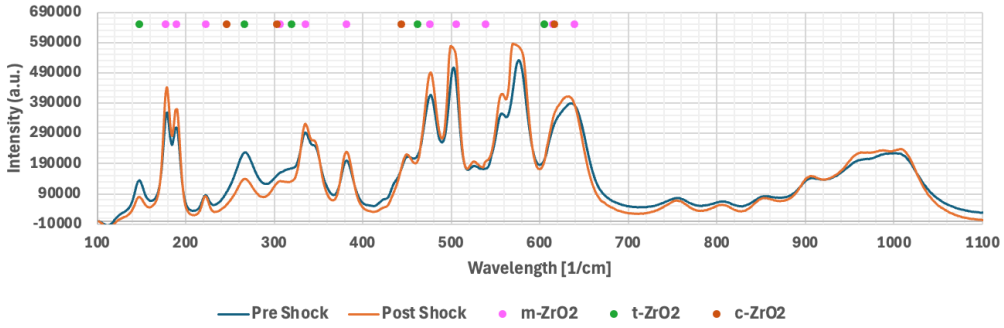

Figure 5.9: Sample 800-3 Raman spectra before and after shock

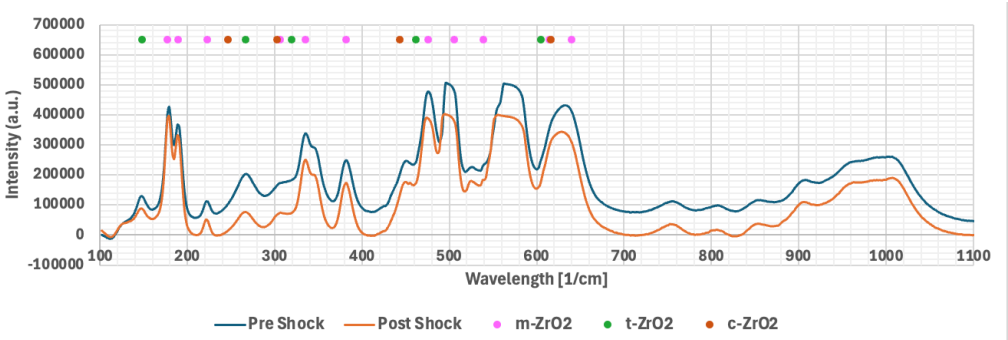

Figure 5.10: Sample 800-5 Raman spectra before and after shock

For Sample 800-3, a comparison of pre- and post-shock spectra reveals moderate increases in peak intensity, particularly in regions associated with m-ZrO_2. These changes suggest that thermal shock may have driven additional t/c→m phase transformation and partially relieved internal stresses accumulated during prior oxidation, allowing the oxide lattice to relax and scatter more coherently, resulting in sharper and stronger Raman signals [31] [33].

Sample 800-5 exhibits a pronounced spectral change after thermal shock, but contrary to typical expectations of intensity gain from stress relief, the Raman spectrum shows a decrease in overall intensity,

despite slight improvements in peak sharpness for m-ZrO_2. This aligns with phase composition data, which showed a significant increase in m-ZrO_2 content (+10.4%) and a decrease in tetragonal/cubic content (–38.7%) post-shock. The phase shift supports the occurrence of a t/c→m transformation and potential stress relaxation. However, the reduced Raman intensity may indicate that the oxide layer experienced surface degradation, such as fragmentation, roughening, or partial spallation, effects that would reduce the volume of Raman-active material and scatter the incident laser. Together, these findings suggest that while thermal shock promoted structural reordering and phase stabilization, it may have also compromised the surface integrity of the oxide, limiting Raman signal enhancement despite improved crystallinity [31] [33].

One unexpected feature of interest is a broad but distinct peak that appears around 1000cm^{-1} in both 800-series samples, becoming more defined after thermal shock. This peak is likely attributed to Zr–O bond stretching modes in m-ZrO_2, potentially arising from second-order Raman processes or high-frequency lattice vibrations [54]. Stretching vibrations occur at higher wavenumbers because they involve direct oscillation of the Zr–O bonds along their bond axis, which requires more energy than bending or deformation modes. This is directly linked to the relaxation of internal stresses. As the t/c→m transformation proceeds and strain is relieved during cooling, the local lattice distortions decrease, allowing the Zr–O bonds to adopt more stable configurations. This results in a stronger, clearer Zr–O stretching signal. The enhanced definition of this band, combined with overall spectral sharpening across the Raman range, reflects a transition from a strained, nanocrystalline oxide to a more crystalline, stress-relieved m-ZrO_2 structure.

5.3.4. Changes in Raman Spectra After Shock

To enable direct comparison of Raman responses after thermal shock across all oxidation conditions, the post-shock spectra of each sample are overlaid in Figure 5.11. This view reveals clear differences in spectral intensity, sharpness, and oxide phase signatures, reflecting how the degree of prior oxidation governs the oxide layer's structural state and stress response.

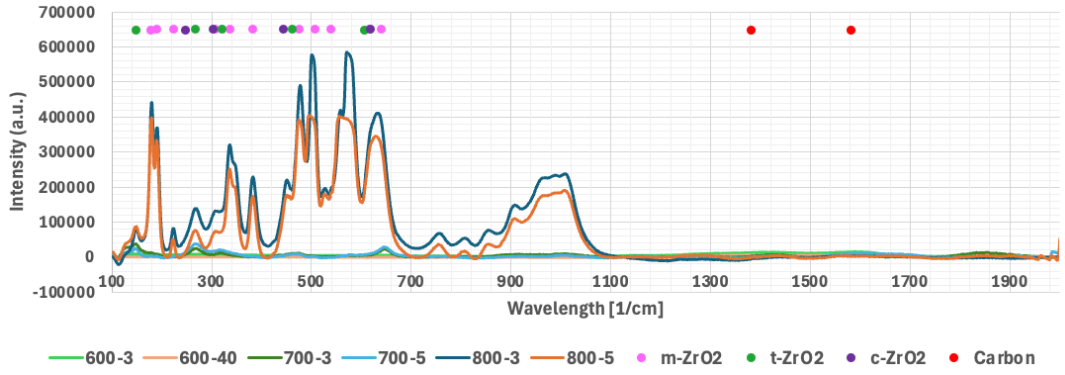

Figure 5.11: Raman spectra of all samples after thermal shock

The 600-series samples exhibit weak and mostly flat spectra, dominated by broad D and G bands or amorphous carbon. These features confirm that the oxide layer is minimal or poorly developed. The absence of distinct zirconia peaks suggests that thermal shock had little impact on the structural organization or stress state of these lightly oxidized, ZrC-rich surfaces.

In contrast, the 700-series samples show moderate Raman activity after shock, including identifiable t-ZrO_2 and m-ZrO_2 features. The spectra are asymmetrically elevated across the range, with broader peaks and a slightly skewed baseline, suggesting a more heterogeneous oxide structure. Such peak broadening and asymmetry are often associated with local strain fields, grain size variation, or subtle compositional disorder, all of which scatter phonons and reduce spectral coherence [54]. This spectral profile implies that thermal shock may have promoted minor stress redistribution or localized oxide reorganization, possibly reducing microstructural constraints without fully relieving internal stresses.

The 800-series samples display the strongest and sharpest Raman peaks, particularly from m-ZrO_2.

A significant increase in intensity and peak sharpness post-shock suggests that thermal shock not only relieved residual stress but also enhanced crystallinity, likely through grain coarsening and phase reordering. This structural maturation is further supported by the emergence of a broad but distinct peak around 1000cm^{-1}, attributed to Zr–O bond stretching in m-ZrO_2. The enhanced definition of this stress-sensitive mode indicates that thermal gradients facilitated the relaxation of internal strain, allowing the oxide lattice to adopt a more ordered and stable configuration.

Overall, this comparative view demonstrates that the extent of prior oxidation strongly influences the material's ability to reorganize under thermal shock. Low-oxidation samples remain spectrally inert, while highly oxidized samples exhibit enhanced Raman responses, consistent with stress relief and oxide refinement. These trends reinforce the idea that thermal shock acts as a structural filter, having minimal impact on underdeveloped oxides, but a significant reorganizing force in well-developed ones.

5.4. Microstructural Analysis After Thermal Shock

As with thermal cycling, SEM was used to examine morphological changes in the oxide scale.

5.4.1. Microstructure of 600-series

The post-shock SEM images of Sample 600-3 reveal subtle but measurable changes relative to the pre-shock condition. While the oxide layer still remains largely smooth and continuous, higher-magnification surface images show a reduction in surface texturing and dark spots previously observed after cycling, suggesting a degree of surface relaxation [4]. Notably, the wrinkling that characterized the thermally cycled state are now less prominent or absent, implying that rapid cooling may have relieved some of the accumulated surface strain or caused minor flattening of surface roughness. The absence of widespread cracking or delamination confirms that the thin oxide layer remains mechanically compliant, but the loss of finer features suggests that thermal shock has subtly altered the surface microstructure, potentially through microstructural densification or stress redistribution.

Cross-sectional SEM images in Figure 5.13 further confirm the limited but distinct effects of shock. Compared to the pre-shock condition, the oxide scale remains thin and continuous, but has a slightly more uniform contrast profile, with less evidence of sub-surface segmentation. This suggests that interfacial stresses may have relaxed or redistributed during rapid cooling, helping preserve overall structural integrity. No signs of delamination, interfacial voids, or through-thickness cracking are observed, reinforcing the idea that the low-strain, low-oxidation regime at 600°C produced a robust and compliant oxide that can withstand moderate thermal shock without catastrophic damage. However, the slight homogenization of contrast and reduced surface roughness suggest a modest reconfiguration of the surface and near-interface region, reflecting the response of the initial-oxidation regime to quench-induced stress.

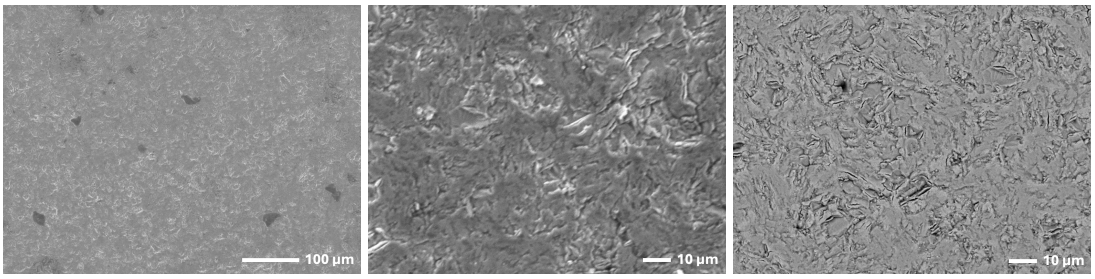

(a) 200x LEI surface image **(b)** 1000x LEI surface image **(c)** 1000x COMPO surface image

Figure 5.12: Surface SEM images of Sample 600-3 oxide layer after thermal shock

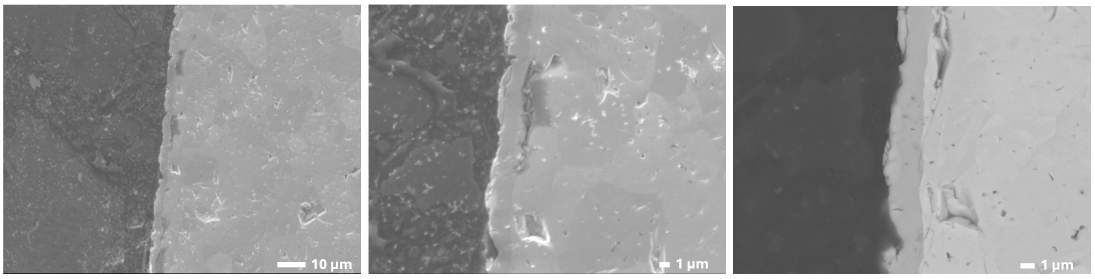

(a) 1000x LEI cross-sectional image **(b)** 3000x LEI cross-sectional image **(c)** 5000x COMPO cross-sectional image

Figure 5.13: Cross-section SEM images of Sample 600-3 oxide layer after thermal shock

The post-shock SEM images of Sample 600-40 (Figure 5.14) show a clear evolution from its pre-shock condition, marked by the emergence of fine, shallow surface cracks across a surface that was previously smooth and voided. Compared to the thermally cycled state, where oxidation produced localized voids and irregular surface relief, the oxide layer now appears more uniformly cracked, with fine but organized crack networks indicative of growing internal stress. The loss of the dark voids and wrinkled topography seen in pre-shock images suggests that the oxide has transitioned from a deformable, stress-accommodating state to a more rigid, brittle regime, where fracture has become the dominant stress-relief mechanism. This transition highlights how prolonged oxidation increases scale stiffness, allowing compressive stress to accumulate and initiate surface cracking during quenching.

Cross-sectional images in Figure 5.15 further reflect this transition. The oxide layer, already thickened during cycling, now appears more uniform structurally consolidated, with localized porosity and interfacial roughening more apparent than before. Compared to the thermally cycled state, the layer remains well-adhered but shows clearer signs of internal stress, particularly in the form of incipient cracking and contrast gradients near the mid-thickness. The intermediate contrast zone between ZrC and outer ZrO_2 remains visible, but now appears more continuous, supporting the idea of ongoing transitional layer growth. Thus, the oxide remains mostly intact, but its resistance to thermal shock is declining as the scale stiffens, loses compliance, and adopts fracture-dominated stress accommodation.

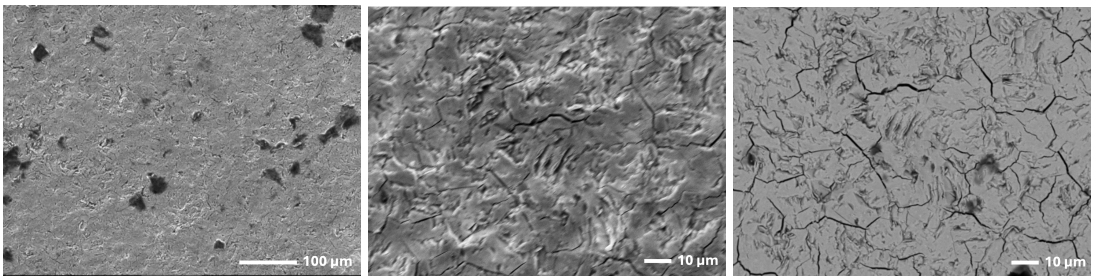

(a) 200x LEI image **(b)** 1000x LEI image **(c)** 1000x COMPO image

Figure 5.14: Surface SEM images of Sample 600-40 oxide layer after thermal shock

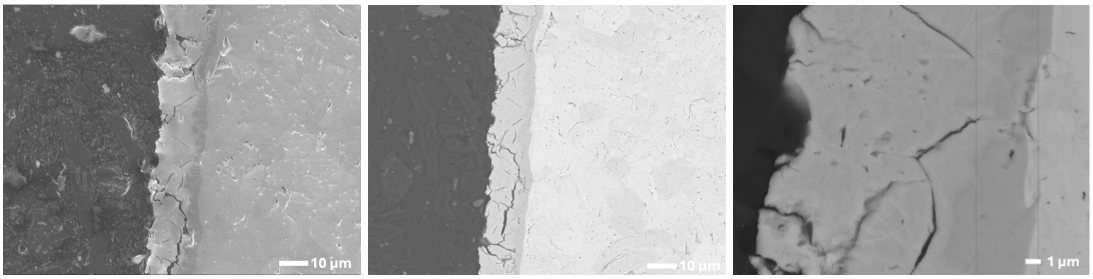

(a) 1000x LEI cross-sectional image **(b)** 1000x COMPO cross-sectional image **(c)** 5000x COMPO cross-sectional image

Figure 5.15: Cross-section SEM images of Sample 600-40 oxide layer after thermal shock

5.4.2. Microstructure of 700-series

Following thermal shock, Sample 700-3 shows a distinct shift in surface and sub-surface microstructure compared to its pre-shock state. After shock (Figure 5.16), the oxide layer presents a dense, interconnected network of sharp cracks, many of which span significant lengths (roughly 65 µm). These cracks often intersect at smooth oxide regions, further indicating that stress relief has transitioned from partial elastic accommodation to brittle fracture. The increase in crack density and continuity highlights a loss of mechanical compliance, consistent with the behavior of a thickened, stiff oxide layer unable to absorb thermal strain without breaking [32] [31].

Cross-sectional images (Figure 5.17) reveal how this transition extends through the oxide thickness. The layer, already developed prior to shock, now shows well-defined through-thickness cracks and expanded internal voiding. Notably, the intermediate contrast zone between the ZrO_2 and ZrC becomes more distinct and structured, suggesting continued interfacial evolution, likely from oxygen diffusion and densification. Additional signs of localized debonding and contrast variation near the oxide–substrate boundary further reflect stress-driven delamination and phase separation not visible before shock. Collectively, these changes confirm that thermal shock pushed the system beyond its elastic limits, transforming it from a stress-tolerant structure into a brittle, fracture-dominated oxide scale.

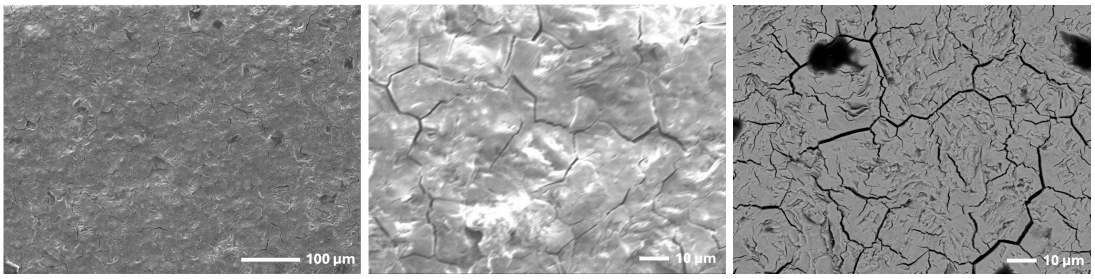

(a) 200x LEI image **(b)** 1000x LEI image **(c)** 1000x COMPO image

Figure 5.16: Surface SEM images of Sample 700-3 oxide layer after thermal shock

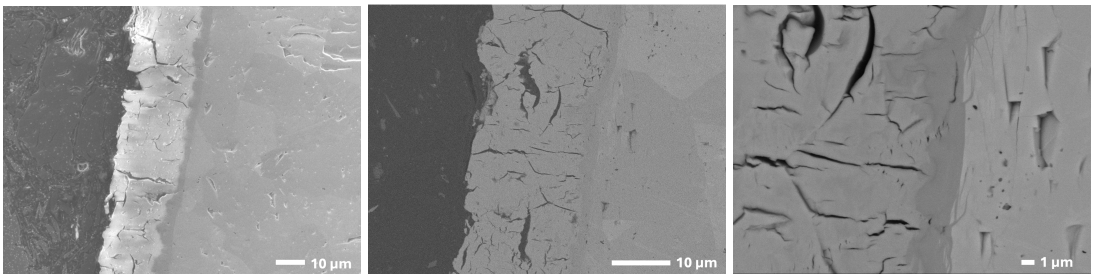

(a) 1000x LEI cross-sectional image **(b)** 2000x COMPO cross-sectional image **(c)** 5000x COMPO cross-sectional image

Figure 5.17: Cross-section SEM images of Sample 700-3 oxide layer after thermal shock

Following thermal shock, Sample 700-5 exhibits substantially greater degradation than both its pre-shock condition and Sample 700-3. While the pre-shock surface already showed roughness and oxidation, post-shock images (Figure 5.18) reveal a denser, more continuous crack network with deeper, sharper fractures that penetrate through the oxide layer. Compared to 700-3, the crack patterns are more pervasive and interconnected, indicating intensified stress buildup and more frequent fracture events due to the longer oxidation duration.

Cross-sectional images (Figure 5.19) reveal a significant transformation in oxide scale microstructure after shock. Compared to the pre-shock state, which showed a thick but relatively stable oxide, the post-shock condition exhibits widespread through-thickness cracking, lateral fracture propagation, and visible delamination. These fractures are sharper and more interconnected than those in 700-3, reflecting higher residual stress and more severe mechanical degradation. The intermediate contrast zone

also becomes broader and more defined, indicating enhanced oxygen diffusion and structural evolution at the interface.

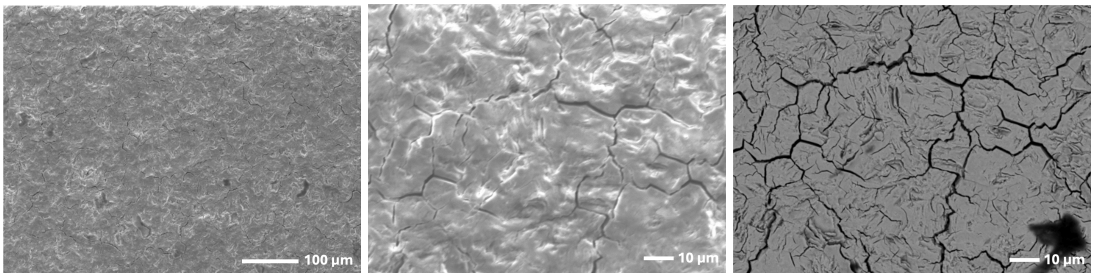

(a) 200x LEI image **(b)** 1000x LEI image **(c)** 1000x COMPO image

Figure 5.18: Surface SEM images of Sample 700-5 oxide layer after thermal shock

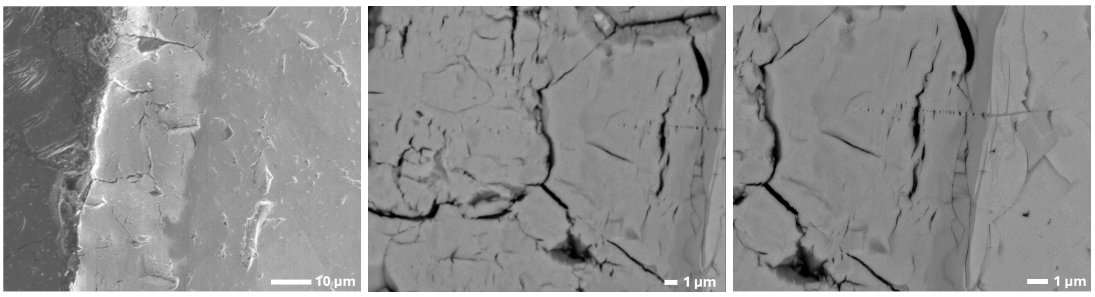

(a) 1000x LEI cross-sectional image **(b)** 4000x COMPO cross-sectional image **(c)** 5000x COMPO cross-sectional image

Figure 5.19: Cross-section SEM images of Sample 700-5 oxide layer after thermal shock

5.4.3. Microstructure of 800-series

Thermal shock significantly intensified the degradation observed in Sample 800-3, amplifying damage beyond what was seen in the 700-series. Compared to its pre-shock state, which already displayed signs of oxidation and isolated cracking, post-shock SEM images (Figure 4.18) reveal a densely interconnected network of wide and deep cracks spanning the oxide surface. These features reflect a substantial progression in damage, indicating that the already-brittle scale could no longer contain internal stresses generated during rapid cooling. Unlike 700-5, the cracks in 800-3 are broader, more pervasive, and suggest catastrophic fracture as the primary stress-relief mechanism.

Cross-sectional images (Figure 4.19) further confirm the extreme nature of the post-shock response. The oxide layer exhibits extensive through-thickness cracking and fragmentation, with many cracks reaching the ZrC interface—more severe than in 700-5. COMPO mode reveals porous regions, microvoids, and evidence of interfacial debonding, especially at crack tips and grain boundaries. While a transitional contrast zone is still visible, it is largely obscured by the widespread fracture and delamination. These observations indicate that the oxide has fully transitioned into a mechanically unstable, brittle regime, where stress relief is dominated by large-scale volumetric failure rather than any ductile accommodation. The progression from pre-shock to post-shock thus marks a critical loss of structural integrity, confirming that even short-duration exposure at 800°C can produce a severely compromised oxide scale under thermal stress.

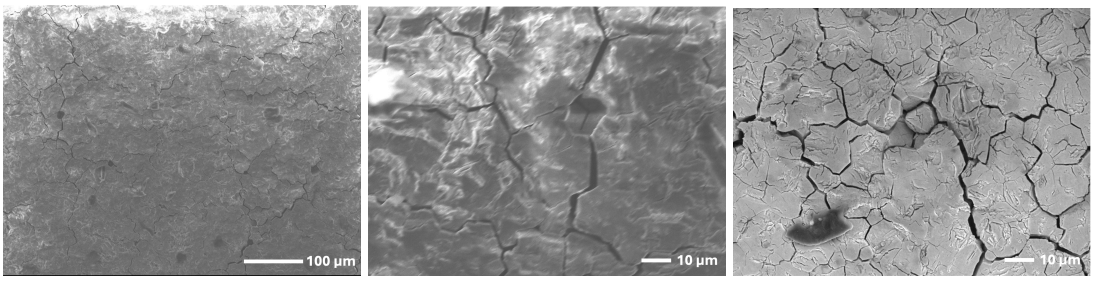

(a) 200x LEI surface image **(b)** 1000x LEI surface image **(c)** 1000x COMPO surface image

Figure 5.20: Surface SEM images of Sample 800-3 oxide layer after thermal shock

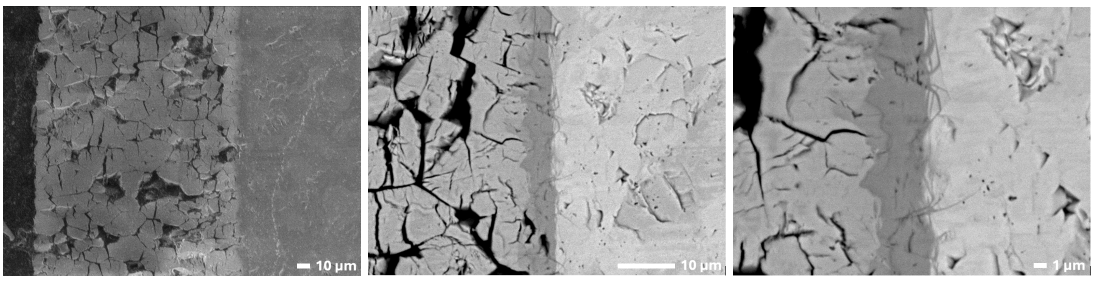

(a) 500x LEI cross-sectional image **(b)** 2000x COMPO cross-sectional image **(c)** 4000x COMPO cross-sectional image

Figure 5.21: Cross-section SEM images of Sample 800-3 oxide layer after thermal shock

Post-shock SEM images of Sample 800-5 reveal the most severe degradation among all conditions. Before shock, the surface already exhibited a thick, roughened oxide scale. However, after thermal shock, the damage becomes more extreme: wide, jagged cracks are distributed densely across the surface, forming a chaotic fracture network with limited regions of intact oxide in between (Figure 5.22). Compared to the pre-shock state, the cracks in 800-5 are broader, more irregular, and appear to slice through larger surface areas, reflecting a critical loss of mechanical stability. Detached and lifted flakes of the oxide are visible, pointing to localized spallation and complete breakdown of surface cohesion under thermal loading.

The cross-sectional SEM images (Figure 5.23) further confirm the catastrophic extent of damage. The oxide scale is both thicker and more fragmented than in 800-3, with pervasive through-thickness and lateral cracking that spans the full depth of the scale. In some regions, cracks extend past the oxide–substrate boundary, indicating widespread interfacial delamination. Internal features appear disordered and porous, lacking clear grain boundaries or phase continuity. These observations suggest that residual thermal stresses at this stage exceed the oxide's ability to deform or absorb strain energy, leaving brittle fracture as the dominant failure mode. Overall, 800-5 exhibits systemic structural failure driven by the combined effects of prolonged high-temperature oxidation and thermal shock.

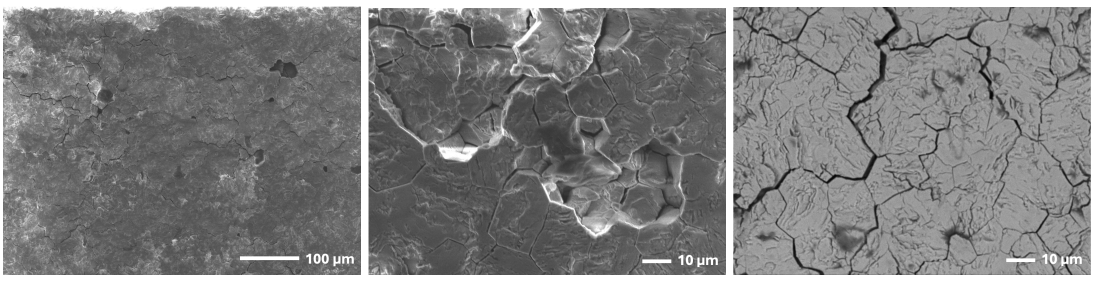

(a) 200x LEI surface image **(b)** 1000x LEI surface image **(c)** 1000x COMPO surface image

Figure 5.22: Surface SEM images of Sample 800-5 after thermal shock

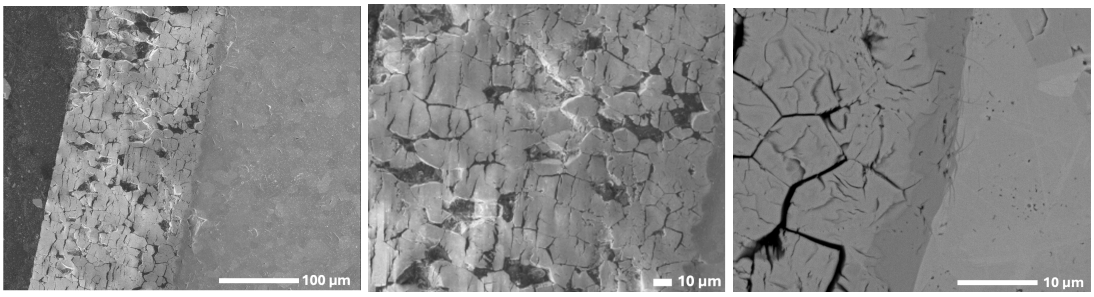

(a) 200x LEI cross-sectional image **(b)** 500x LEI cross-sectional image **(c)** 2000x COMPO cross-sectional image

Figure 5.23: Cross-section SEM images of Sample 800-5 after thermal shock

Altogether, the observations indicate that thermal shock significantly exacerbated pre-existing oxidation damage, pushing the brittle, fully oxidized surface past its mechanical limits. The resulting crack network reflects a transition to a structurally compromised state, where the oxide can no longer accommodate thermal strain or function as a protective barrier.

5.4.4. Crack Densities Before and After Shock

The trends in Figure 5.24 reveal distinct behaviors between surface and internal cracking in response to thermal shock. Surface crack density shows noticeable increases post-shock, particularly in the 600- and 700-series, where the oxide layers are thinner and less developed. This suggests that thermal shock stresses have a stronger impact when the oxide is thin and less able to redistribute strain. Thinner oxides experience higher effective thermal gradients through their thickness, leading to steep stress concentrations at the surface. Additionally, the lower stiffness and reduced ability to absorb strain energy in thin, developing oxide layers make them more susceptible to surface fracture under rapid temperature change.

In contrast, internal crack density shows relatively minor changes between pre- and post-shock for most samples, particularly in the heavily oxidized 800-series, where internal cracking is already severe prior to shock. This indicates that internal cracks are primarily driven by oxidation-related stress (such as CTE mismatch between the growing oxide and ZrC substrate or phase transformation strain) rather than by transient thermal shock loads. Once the oxide reaches a certain thickness and stiffness, internal stresses accumulate to the point where thermal cycling alone generates extensive subsurface damage, leaving little room for additional cracking from quenching.

Together, these results highlight that surface cracking is more sensitive to thermal shock effects in thinner oxides, where transient thermal gradients dominate the stress profile. Conversely, internal cracking is largely governed by long-term oxidation-driven stress, with thermal shock having a limited additional effect once critical damage levels are reached.

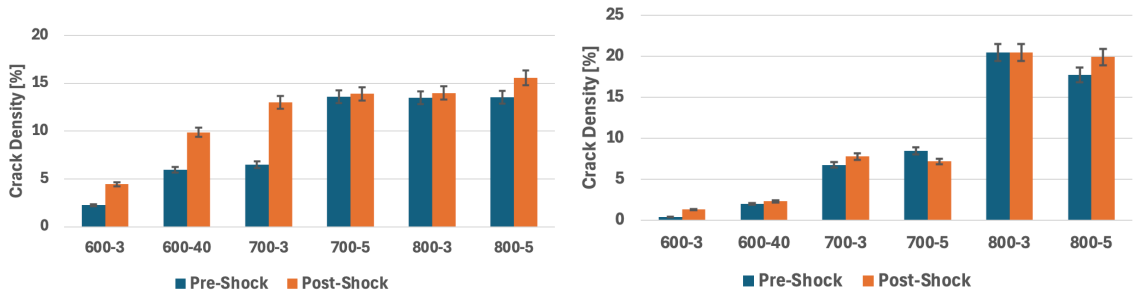

(a) Surface crack densities **(b)** Internal crack densities

Figure 5.24: Changes in crack density before and after thermal shock

5.4.5. Oxide Layer Growth Before and After Shock

In addition to crack density, oxide layer growth was monitored. However, the data in Figure 5.25 do not reveal a clear, consistent trend in oxide scale growth as a result of thermal shock. While some samples, particularly 800-5, exhibit noticeable increases in both the outer and intermediate layer thicknesses post-shock, others show minimal change or even slight reductions. This variability suggests that thermal shock does not uniformly drive additional oxidation or growth but may instead interact with pre-existing defects, porosity, or localized damage within the oxide.

In cases like 800-5, the post-shock thickening, particularly in the intermediate layer, may result from microcrack-assisted oxygen ingress or local densification and structural rearrangement. However, the absence of similar growth in other samples, such as 800-3, implies that this effect is not solely driven by oxidation temperature or scale thickness but is likely influenced by stochastic factors such as local crack distribution or variations in oxide integrity.

Overall, while the data suggest that thermal shock can in some cases contribute to further oxide development, particularly in already compromised or heavily oxidized scales, it does not universally drive significant oxide growth across all conditions. This highlights the complex interplay between mechanical damage, oxidation kinetics, and microstructural variability in the post-shock evolution of the oxide scale.

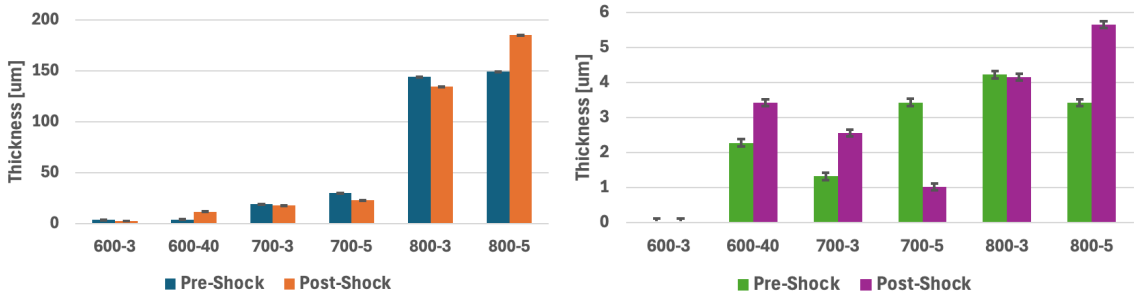

(a) Outer layer of oxide scale

(b) Intermediate layer of oxide scale

Figure 5.25: Growth of oxide layer before and after thermal shock

6

Research Question 1

This chapter addresses the question: How does prior oxidation history (temperature and duration) affect the extent of surface and internal damage after thermal shock?

This question focuses on quantitatively linking pre-oxidation conditions to measurable post-shock outcomes. The aim is to assess how variations in oxidation severity shape the system's susceptibility to thermal shock-induced changes, focusing on the crack density. By establishing these quantitative relationships, the study seeks to clarify how oxidation history governs the severity and type of surface degradation observed.

6.1. Experimental Goal

To address this question, experiments were designed to systematically compare the post-shock phase and damage evolution across samples with controlled oxidation histories. Samples were cycled at different temperatures (600°C, 700°C, 800°C) and durations, creating a range of oxide thicknesses and phase distributions. Before and after thermal shock, quantitative data was collected on crack density and oxude thickness via SEM. This section presents how these metrics vary with oxidation history, revealing how the combined effects of prior oxidation and thermal shock determine the surface system's damage response.

6.2. Observations From Before and After Thermal Shock

Post-shock analysis revealed a strong correlation between oxidation history and surface degradation severity. As shown in Figure 6.1, both surface and internal crack densities increased with oxidation temperature and duration, and spallation became more prevalent in heavily oxidized samples.

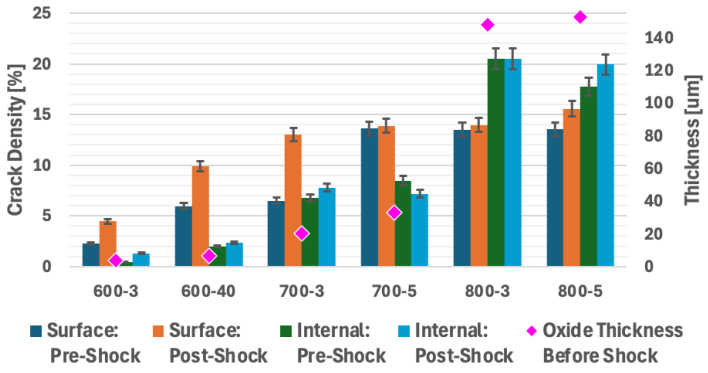

Figure 6.1: Assessment of crack density and spallation for all samples before and after thermal shock. Error bars for oxide thickness are included but are too small to be visible at this scale.

The 600°C samples showed minimal thermal shock damage. Sample 600-3 reached a post-shock surface crack density of 4.45%, while 600-40 reached 9.87%. Internal crack densities remained low,

at just 0.43% and 2.00%, respectively. No spallation was observed. These results confirm that thin, patchy oxides formed under low-temperature conditions are compliant and lack the mechanical stiffness or stored strain energy needed to drive delamination or through-thickness failure.

At 700°C, both surface and internal cracking became more pronounced. Sample 700-3 reached 13.0% surface crack density and 6.75% internal density, while 700-5 increased to 13.9% and 8.48%, respectively. The elevated internal cracking in both samples indicates that stresses are no longer confined to the surface.

The 800°C samples exhibited the most extensive degradation. Surface crack densities rose to 13.97% (800-3) and 15.56% (800-5), while internal crack densities were 20.47% and 17.75%, respectively, the highest of all samples. Both also exhibited significant spallation and extensive structural damage. These observations confirm that at elevated temperatures, thick, rigid oxide scales accumulate high thermal mismatch stresses, which ultimately lead to brittle fracture and interfacial delamination.

In addition, the significant increase in oxide thickness with both temperature and exposure time promotes t/c→m phase transformation. As thermal stress accumulates within the growing oxide, it can exceed the stability limits of the metastable tetragonal phase, triggering transformation to the monoclinic form. This phase change further contributes to volume expansion, localized stress concentration, and crack nucleation. These observations support stress-driven damage models involving both oxide scale fracture and t/c→m transformation as key failure mechanisms [4] [31] [33].

6.3. Linking Damage Evolution to Oxidation History

The progression of crack density and oxide thickness across the sample series highlights how prior oxidation fundamentally determines the material's thermal shock response. Rather than acting as a passive byproduct, oxidation history dictates how stress accumulates and is later released during rapid cooling.

What distinguishes the higher-temperature samples is not just the presence of thicker oxide layers, but the mechanical rigidity and internal strain they carry into the shock step. Elevated internal crack densities, extensive spallation, and a breakdown in interfacial cohesion indicate that these relatively more developed scales likely exceed a critical stress threshold during cooling. This behavior aligns with stress-based failure mechanisms, including t/c→m phase transformation and strain-driven fracture, where residual thermal strain and phase instability trigger widespread degradation rather than localized cracking [4] [31] [33].

In contrast, the 600-series samples showed minimal internal damage and no delamination, despite experiencing the same thermal shock conditions. This underscores the protective role of limited oxidation and confirms that damage is governed less by the shock itself than by the system's prior thermal and structural condition. These findings reinforce that oxidation history, not simply temperature, sets the stage for mechanical vulnerability under thermal loading.

Ultimately, the data support the study's central argument: prior oxidation governs not only the phase constitution of the oxide layer but also its mechanical resilience. As oxidation progresses, stress accumulation can exceed the stability limits of the tetragonal phase, promoting t/c→m transformation, crack propagation, and eventual structural failure. These findings emphasize that controlling oxidation history is as critical as material selection when designing UHTC components for thermal shock resistance. Limiting oxide thickness growth can help delay the transition to bulk damage modes dominated by internal cracking.

7

Research Question 2

This chapter addresses the question: Under what oxidation conditions (temperature and duration) does ZrC become susceptible to critical failure when subjected to thermal shock?

This question focuses on identifying the critical oxidation thresholds beyond which the material system exhibits clear signs of failure after thermal shock. These failure indicators include significant increases in monoclinic ZrO_2 fraction, sharp rises in crack density, or the onset of scale spallation. The aim is to define the operational boundaries where prior oxidation leads to a measurable loss of surface integrity, helping to map the limits of ZrC's thermal shock tolerance.

7.1. Experimental Goal

To address this question, experiments were designed to pinpoint the oxidation conditions at which the surface system shifts from stable to degraded behavior under shock. Samples were pre-oxidized under controlled thermal cycling conditions at varying temperatures (600°C, 700°C, 800°C) and durations, generating different oxide thicknesses and phase compositions. After applying thermal shock, key damage metrics, including phase shifts (from XRD) and crack density (from SEM) were quantified.

This section analyzes how post-shock damage metrics escalate with increasing oxidation severity, focusing on the thresholds where the system transitions into measurable structural degradation. Two independent but complementary failure criteria were used: a rise in m-ZrO_2 content exceeding 10% above the baseline, and a surface crack density exceeding 10% after thermal shock. Either threshold alone is sufficient to indicate that the material has transitioned into a structurally unstable regime. However, when both occur simultaneously, this indicates severe degradation beyond recoverable limits.

A rise in m-ZrO_2 of about 10% above the baseline proves to be a reliable failure metric because it coincides with pronounced losses in key properties. For instance, in additively manufactured zirconia, increasing the monoclinic fraction from roughly 7% to 9% leads to a decrease in biaxial flexural strength of about 21%, demonstrating that even small shifts near this window carry a large penalty in load-bearing capacity [9]. Complementing this, retrieval and aging studies of biomedical zirconia show that once monoclinic content climbs toward 20%, surface roughness jumps from a few nanometers to over 100 nm and microcrack networks become apparent, signifying severe loss of protective behavior and stiffness [10]. Using a 10% threshold is therefore conservative, catching damage accumulation well before such drastic degradation manifests.

Surface crack densities exceeding 10% after thermal shock are also commonly associated with the onset of mechanical instability in oxidized ceramics [31]. This is often accompanied by oxide spallation, signaling that stored thermal stresses have surpassed the fracture tolerance of the oxide layer [4]. Notably, NASA defines failure in thermal barrier coatings as occurring when 10% of the surface area of the ceramic top coat has spalled [11], underscoring that reaching this spall threshold correlates with critical loss of protective behavior. For this reason, a 10% crack density is used as a structural failure threshold, as it marks the stage where microcracks begin to coalesce, leading to rapid mechanical degradation. In one study on zirconia ceramics, this crack density was shown to coincide with the saturation of transformation-induced plasticity [12]. At this point, the material's Young's modulus dropped by about 30%, indicating a significant loss in stiffness and its ability to dissipate energy. Be-

yond this threshold, the structure can no longer accommodate thermal strain, making 10% a practical and mechanistically justified limit for failure under oxidative or thermal stress conditions.

These findings set the stage for defining safe operating conditions for ZrC and establish clear thresholds where prior oxidation pushes the material beyond its structural limits under thermal shock.

7.2. Observations After Thermal Shock

The post-shock data reveal a clear relationship between prior oxidation conditions and the emergence of degradation markers in ZrC (Figure 7.1).

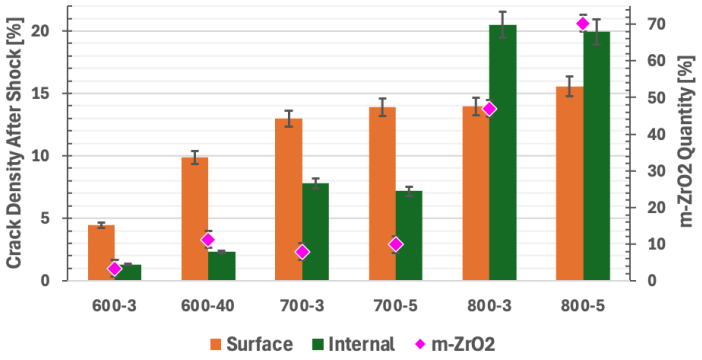

Figure 7.1: Assessment of m-ZrO_2 surface quantity and crack density growth due to thermal shock

Samples cycled at 600°C exhibited minimal thermal shock damage. Surface crack densities remained below 10%, and m-ZrO_2 fractions stayed low (around 10–15%). This indicates that the oxide layers formed at this temperature were thin and compliant enough to avoid significant thermal stress accumulation. Consequently, both phase transformation strain and mechanical failure remained below critical thresholds.

In contrast, the 700°C samples represent a transitional regime. Post-shock surface crack densities rose to 13.0% (700-3) and 13.9% (700-5), exceeding surface instability thresholds commonly cited in literature (10–12%) [11] [12] [31]. However, m-ZrO_2 quantities remained relatively moderate (20–25%), suggesting that while local surface stress was sufficient to drive cracking, the oxide had not yet transformed extensively into the monoclinic phase. Internal cracking remained moderate, indicating that although degradation was advancing, the oxide had not fully entered a brittle, failure-prone regime.

At 800°C, degradation was widespread and severe. Both samples exhibited high monoclinic concentrations (50–65% m-ZrO_2), accompanied by surface crack densities exceeding 13.5% and internal crack densities over 19%. This high monoclinic fraction reflects extensive stress-driven t/c→m transformation, paired with accumulated oxidation strain. The mechanical consequences of this transformation (volume expansion, crack initiation, and interfacial delamination) were evident in the pronounced through-thickness cracking and spallation seen in SEM analysis.

Altogether, these results affirm that oxidation at 700°C represents a threshold regime, where surface cracking begins to dominate but phase transformation-driven embrittlement is not yet severe. In contrast, 800°C conditions result in fully transformed, brittle oxide scales whose mechanical instability under thermal shock leads to catastrophic surface and internal damage. The clear correlation between total m-ZrO_2 fraction and internal crack density underscores the role of phase transformation as a primary driver of mechanical failure in oxidized zirconium carbide systems.

7.3. Identifying Critical Oxidation Conditions for Shock Resistance

These results establish the oxidation conditions under which ZrC-based materials transition from shock-resistant to failure-prone behavior. By combining observations of m-ZrO_2 content, crack densities, and oxide morphology, the data indicate that the critical transition occurs between 700°C and 800°C oxidation conditions, with exposure duration acting as a secondary but amplifying factor.

At 600°C, regardless of duration, the oxide remains thin, compliant, and resistant to failure. Surface crack densities remain below 10%, monoclinic ZrO_2 content stays well below the 10% threshold, and internal crack densities are negligible (≤2%). These results confirm that under mild oxidation, the oxide scale lacks the stiffness and internal strain required to trigger either transformation-driven failure or thermal shock-induced cracking.

At 700°C, the first signs of entering a stress-dominated regime emerge. Surface crack densities rise above 10%, specifically to 13.0% (700-3) and 13.9% (700-5), clearly exceeding the surface crack density threshold associated with the onset of mechanical instability [31]. This confirms that the oxide has entered a mechanically degraded state under thermal shock. Meanwhile, m-ZrO_2 content increases to 20–25%, surpassing the conservative 10% transformation threshold, indicating that stress-driven phase transformation is also actively contributing to degradation. However, internal crack densities remain below 9%, suggesting that while the system has crossed the failure threshold in terms of surface cracking and transformation strain, the damage remains largely surface-concentrated rather than fully propagating through the oxide thickness.

At 800°C, degradation becomes severe and systemic. Both failure criteria are now exceeded by large margins: m-ZrO_2 content rises beyond 50–65%, and surface crack densities exceed 13.5%. Internal crack densities jump above 17%, indicating that damage has fully propagated through the oxide thickness. Here, t/c→m transformation transitions from a stress-relief mechanism into a driver of volumetric strain, contributing directly to fracture, shear failure, and delamination. SEM confirms widespread spallation and cracking, signifying a total breakdown in the oxide's mechanical integrity.

Taken together, these results show that exceeding either 10% monoclinic content or 10% surface crack density serves as a reliable threshold for the onset of thermal shock-induced failure. Monoclinic growth captures stress-driven phase transformation within the oxide, while surface cracking reflects the material's inability to accommodate thermal mismatch strain. Internal cracking and spallation are not required to define failure onset but instead mark the progression toward more severe, through-thickness, and ultimately catastrophic damage. Spallation, in particular, serves as the terminal failure event, occurring once residual stress exceeds either adhesion limits at the substrate interface or cohesion within the oxide.

In summary, oxidation at 700°C marks the transition into a failure-prone regime, where degradation mechanisms (stress-driven transformation and surface cracking) have crossed their critical thresholds. However, this condition remains transitional, as damage is primarily surface-localized, with internal cracking still moderate and no widespread spallation observed. In contrast, oxidation at or above 800°C leads to catastrophic failure, characterized by thick, rigid, stress-laden oxide scales prone to extensive t/c→m transformation, through-thickness cracking, delamination, and spallation upon thermal shock. These conditions define a clear boundary for structural instability. Below this point, as demonstrated by the 600°C samples, oxidation produces thin, compliant oxide layers that remain mechanically stable under thermal shock. These benchmarks offer actionable guidance for defining safe oxidation limits and thermal shock tolerance for ZrC-based systems in harsh environments.

8

Conclusion and Outlook

This thesis investigated how oxidation history influences the thermal shock degradation of monolithic ZrC and identified the oxidation conditions where ZrC transitions from shock-resistant to failure-prone behavior. The results demonstrate that oxidation severity is the primary factor governing damage progression. Samples oxidized at 600°C exhibited minimal thermal shock damage, forming thin and compliant oxide layers that lacked the stiffness or residual stress needed to drive significant cracking. In contrast, oxidation at 800°C produced thick, brittle oxide scales prone to severe cracking and widespread mechanical failure following thermal shock. The oxide structure at this condition is dominated by m-ZrO_2, with a high degree of residual stress from both growth strain and phase transformation, rendering it mechanically incompatible with the underlying ZrC substrate during rapid thermal gradients.

A key outcome is that the transition from stable to failure-prone behavior occurs between 700°C and 800°C. At 700°C, the system crosses the failure threshold, as surface crack densities exceed 10% and m-ZrO_2 content rises to 20–25% after thermal shock. While catastrophic failure mechanisms such as extensive spallation and through-thickness cracking are not yet fully developed at this point, surface damage becomes significant, and the material enters a mechanically unstable regime. In contrast, oxidation at 800°C leads to catastrophic failure, characterized by m-ZrO_2 exceeding 50%, severe surface and internal cracking, and widespread spallation. At this stage, the oxide scale can no longer accommodate thermal mismatch strain or transformation-induced stresses, resulting in mechanical breakdown.

The study validates two primary failure criteria: m-ZrO_2 content exceeding 10% and surface crack density above 10%. Either threshold independently signals the onset of thermal shock-induced failure, while both together indicate fully brittle, transformation-driven degradation. Surface cracking is particularly sensitive to thermal shock when oxide layers are thin, where steep temperature gradients dominate the stress distribution. In contrast, internal damage becomes more prominent in heavily oxidized samples, where failure is primarily driven by oxidation-induced residual stresses, especially those associated with the tetragonal-to-monoclinic phase transformation and thermal expansion mismatch between the oxide and substrate.

Therefore, ZrC transitions from shock-resistant to failure-prone behavior when oxidized at 700°C or higher. The 700°C condition marks the onset of mechanical instability, where degradation initiates through surface cracking and transformation strain, while oxidation at 800°C produces catastrophic failure characterized by severe through-thickness cracking, delamination, and spallation.

These findings have important implications for the use of ZrC in aerospace systems subjected to high temperatures and thermal cycling. The identified failure thresholds, based on monoclinic phase fraction and surface crack density, offer quantitative and practical criteria for assessing material integrity and defining service limits. This work advances the understanding of degradation mechanisms in UHTCs and informs material selection, design strategies, and life prediction models for components such as TPSs in hypersonic and atmospheric re-entry vehicles.

Oxidation prior to thermal shock is the dominant factor governing whether ZrC survives or fails. The failure benchmarks established in this work (monoclinic phase content and surface crack density) provide a practical and reliable framework for defining safe operating limits and predicting the service life of ZrC-based materials in oxidative, thermally extreme environments.

9

Recommendations For Future Work

While this study provides valuable insights into the coupled effects of oxidation and thermal shock on monolithic ZrC, several limitations highlight opportunities for future research. Addressing these limitations would improve the accuracy, applicability, and relevance of the findings for real-world applications.

One key limitation of this study is the use of relatively short oxidation durations which, while effective for controlled testing, do not fully represent the thermal exposure conditions encountered in real orbital or high-speed flight environments. In practice, spacecraft materials often experience lower oxidation temperatures sustained over longer durations for many thermal cycles, rather than brief, high-temperature events. Future studies should adopt oxidation protocols that better reflect these conditions, focusing on extended exposures at moderate temperatures to simulate the cumulative effects of oxygen ingress, residual stress buildup, and thermal cycling seen during orbit or atmospheric flight. Incorporating variable oxygen partial pressures or transitions between oxidative and vacuum conditions would further improve relevance, offering a more realistic picture of long-term degradation behavior.

Additionally, a significant source of experimental variability in this study was the non-uniform geometry of the ZrC samples, which likely influenced oxidation behavior. Variations in edge sharpness, surface curvature, and local thickness can lead to uneven oxidation rates, non-uniform oxide thickness, and localized stress concentrations, which in turn affect cracking behavior and damage progression. For future work, using samples with standardized, well-controlled geometries would reduce this variability. More uniform sample shapes would help isolate the intrinsic material response from geometry-induced artifacts and improve the reliability of quantitative comparisons between conditions.

Additionally, the thermal shock method employed (direct water quenching) proved effective for testing oxide scales within the thickness and integrity range observed here. However, at higher oxidation temperatures or longer durations, the oxide scale becomes significantly thicker and more brittle. In preliminary tests, it was observed that at high oxidation levels, the oxide layers were prone to spalling or detaching entirely during the water quench. This failure mode makes it difficult to isolate thermal shock effects from pre-existing oxidation-driven damage. For future studies exploring higher temperatures or thicker oxide scales, alternative thermal shock methods may be necessary. Options could include gas quenching, controlled air jets, or radiative cooling approaches, which apply thermal gradients without introducing mechanical stresses associated with water impact.

Future work should focus on longer oxidation durations, improved sample uniformity, investigation of ZrC-based composites, and development of alternative thermal shock testing methods for thicker or more brittle oxide scales. These steps will enhance the understanding of how ZrC-based systems behave under realistic service conditions and contribute to the development of more robust, oxidation-tolerant thermal protection materials.

References

[1] B. Wyatt et al. “Ultra-high temperature ceramics for extreme environments”. In: *Nature Reviews Materials* 9 (2024), pp. 773–789.

[2] S. Johnson, M. Gasch, and J. Lawson. “Recent Developments in Ultra High Temperature Ceramics at NASA Ames”. In: *16th AIAA/DLR/DGLR International Space Planes and Hypersonic Systems and Technologies Conference* (2009).

[3] J.F. Justin and A. Jankowiak. “Ultra High Temperature Ceramics: Densification, Properties and Thermal Stability”. In: *Journal Aerospace Lab* (3 2011).

[4] Meng et al. “Mechanisms of thermal shock failure for ultra-high temperature ceramic”. In: *Materials and Design* 30 (2009), pp. 2108–2112.

[5] C. Gasparrini et al. “Zirconium carbide oxidation: Kinetics and oxygen diffusion through the intermediate layer”. In: *Journal of the American Ceramic Society* 101 (2018), pp. 2638–3652.

[6] G. Peterson, R. Carr, and E. Marinero. “Zirconium Carbide for Hypersonic Applications, Opportunities and Challenges”. In: *Materials* 16 (2023).

[7] R. Haggerty et al. “Thermal Expansion of HfO2 and ZrO2”. In: *J. Am. Ceram. Soc.,* 97 (2014), pp. 2213–2222.

[8] Osgood J. Whittemore and Neil N. Ault. “Thermal Expansion of Various Ceramic Materials to 1500°C”. In: *Journal of the American Ceramic Society* 39.12 (1956), pp. 444–453. DOI: 10.1111/j.1151-2916.1956.tb15619.x. URL: https://doi.org/10.1111/j.1151-2916.1956.tb15619.x.

[9] L.G. Yoo et al. “Mechanical properties of additively manufactured zirconia with alumina air abrasion surface treatment”. In: *Scientific Reports* 13 (2023).

[10] Jérôme Chevalier, Laurent Gremillard, and Sylvain Deville. “Low-Temperature Degradation of Zirconia and Implications for Biomedical Implants”. In: *Annual Review of Materials Research* 37 (2007), pp. 1–32. DOI: 10.1146/annurev.matsci.37.052506.084250. URL: https://doi.org/10.1146/annurev.matsci.37.052506.084250.

[11] R. V. Hillery, B. H. Pilsner, and E. C. Duderstadt. *Thermal Barrier Coating Life Prediction Model Development*. Technical Report NASA N88-11184; NASA Contract NAS3-23943. NASA Lewis Research Center; General Electric Aircraft Engine Business Group, 1988.

[12] P. Reyes-Morel and I-W. Chen. “Stress-Biased Anisotropic Microcracking in Zirconia Polycrystals”. In: *Journal of the American Ceramic Society* 73.4 (1990).

[13] *Zirconium Carbide, ZrC*. Matweb Material Data. 2024.

[14] *Zirconium Carbide (ZrC)*. AZO Materials. 2024.

[15] *Carlisle 201HL Carbon-Carbon Composite*. Matweb Material Data. 2024.

[16] *Carbon Fibre / Carbon Matrix Composite - Supplier Data by Goodfellow*. AZO Materials. 2024.

[17] *Special Metals INCONEL® Alloy 718*. ASM Aerospace Specification Metals Inc. 2024.

[18] E. Zapata-Solvas et al. “Mechanical properties of ZrB2- and HfB2-based ultra-high temperature ceramics fabricated by spark plasma sintering”. In: *Journal of the European Ceramic Society* 33 (2013), pp. 1373–1386.

[19] L. Xu et al. “Effects of ZrB2 powders on microstructure and mechanical properties of ZrB2-SiCw ceramics”. In: *Ceramics International* 48 (2022), pp. 31060–31064.

[20] X. Yang et al. “Densification, microstructure and properties of ultra-high temperature HfB2 ceramics by the spark plasma sintering without any additives”. In: *Ceramics International* 49 (2023), pp. 10748–10755.

[21] Ni et al. “Advances in ultra-high temperature ceramics, composites, and coatings”. In: *Journal of Advanced Ceramics* 11 (2022).

[22] Levine et al. “Evaluation of ultra-high temperature ceramics for aeropropulsion use”. In: *Journal of the European Ceramic Society* 22 (2002), pp. 2757–2767.

[23] A. K. Kuriakose and J. L. Margrave. “The Oxidation Kinetics of Zirconium Diboride and Zirconium Carbide at High Temperatures”. In: *Journal of The Electrochemical Society* (1964).

[24] G.A. Rama Rao and V. Venugopal. “Kinetics and mechanism of the oxidation of ZrC”. In: *Journal of Alloys and Compounds* (206), pp. 237–242.

[25] A.H. Ouensanga and M Dode. “Etude thermodynamique et structurale a haute temperature du systeme Zr-C-O. Diagramme de phases a 1555°C”. In: *Journal of Nuclear Materials* (1976).

[26] X. Liu et al. “The degradation behavior of C/SiC composites in complex environment”. In: *Materials Science and Engineering A* 546 (2012), pp. 212–217.

[27] M. Youssef J. Yang and B. Yildiz. “Oxygen self-diffusion mechanisms in monoclinic ZrO2 revealed and quantified by density functional theory, random walk analysis, and kinetic Monte Carlo calculations”. In: *Physical Review* (2018).

[28] L. Tsetseris and S. T. Pantelides. “Oxygen Migration, Agglomeration, and Trapping: Key Factors for the Morphology of the Si-SiO2 Interface”. In: *Phys. Rev. Lett.* (2006).

[29] ASM International. *ASM Alloy Phase Diagram Database*. 1976.

[30] Yong Han and Junfa Zhu. “ChemInform Abstract: Surface Science Studies on the Zirconia-Based Model Catalysts”. In: *Topics in Catalysis* 56 (Nov. 2013). DOI: 10.1007/s11244-013-0156-5.

[31] Florian Frank et al. “In-Situ Investigation of the Oxidation Behaviour of Chemical Vapour Deposited Zr(C,N) Hard Coatings Using Synchrotron X-ray Diffraction”. In: *Coatings* 11.3 (2021), p. 264. DOI: 10.3390/coatings11030264. URL: https://doi.org/10.3390/coatings11030264.

[32] S. Shimada and T. Ishii. “Oxidation Kinetics of Zirconium Carbide at Relatively low Temperatures”. In: *Journal of the American Ceramic Society* (1990).

[33] K. Tamura, T. Ogawa, and K. Fukuda. “The oxidation behavior of ZrC coating and powder studied by laser Raman spectroscopy and X-ray diffraction”. In: *Journal of Nuclear Materials* 175.3 (1990), pp. 266–269. DOI: 10.1016/0022-3115(90)90274-U.

[34] L. Chen et al. “Effect of surface heat transfer coefficient gradient on thermal shock failure of ceramic materials under rapid cooling condition”. In: *Ceramics International* 44 (2018), pp. 8992–8999.

[35] Kane et al. “Oxidation of ultrahigh temperature ceramics: kinetics, mechanisms, and applications”. In: *Journal of the European Ceramic Society* 41 (2021), pp. 6130–6150.

[36] Zhang et al. “Key issues of MoSi2-UHTC ceramics for ultra high temperature heating element applications: Mechanical, electrical, oxidation and thermal shock behaviors”. In: *Journal of Alloys and Compounds* 780 (2019), pp. 156–163.

[37] M.T. Konnik et al. “High-temperature oxidation and nitridation of substoichiometric zirconium carbide in isothermal air”. In: *Journal of the European Ceramic Society* (2023).

[38] M. Inagaki S. Shimada M. Nishisako. “Formation and Microstructure of Carbon-Containing Oxide Scales by Oxidation of Single Crystals of Zirconium Carbide”. In: *Journal of the American Ceramic Society* 78 (1995), pp. 41–48.

[39] L. Backman et al. “The oxidation kinetics and mechanisms observed during ultra-high temperature oxidation of (HfZrTiTaNb)C and (HfZrTiTaNb)B2”. In: *Journal of Applied Physics* (2024).

[40] Pasquale Cavaliere, ed. *Spark Plasma Sintering of Materials: Advances in Processing and Applications*. Springer Nature Switzerland, 2019. ISBN: 978-3-030-05326-0. DOI: 10.1007/978-3-030-05327-7. URL: https://doi.org/10.1007/978-3-030-05327-7.

[41] Xiang Wang et al. “Densification Mechanism, Microstructure and Mechanical Properties of ZrC Ceramics Prepared by High-Pressure Spark Plasma Sintering”. In: *Journal of the European Ceramic Society* 37.4 (2017), pp. 1731–1737. DOI: 10.1016/j.jeurceramsoc.2016.11.005.

[42] Simone Ferrari and Paolo Sciti. “Comparison of Reactive and Non-Reactive Spark Plasma Sintering Routes for the Fabrication of Monolithic and Composite Ultra High Temperature Ceramics (UHTC) Materials”. In: *Journal of the European Ceramic Society* 39.4 (2019), pp. 1117–1125. DOI: 10.1016/j.jeurceramsoc.2018.11.031.

[43] Jian Yang, William G. Fahrenholtz, and Greg E. Hilmas. “Fast Densification of Ultra-High-Temperature Ceramics by Spark Plasma Sintering”. In: *Scripta Materialia* 69.3 (2013), pp. 179–182. DOI: 10.1016/j.scriptamat.2013.03.016.

[44] Bohui Song et al. “Material Characterization, Modelling and Simulation of Epoxy Moulding Compounds under High Temperature Storage and Temperature Cycling Thermal Ageing”. In: *Microelectronics Reliability* 106 (2020), p. 113579. DOI: 10.1016/j.microrel.2019.113579. URL: https://doi.org/10.1016/j.microrel.2019.113579.

[45] André Chrysochoos. “Thermomechanical Analysis of the Cyclic Behavior of Materials”. In: *Procedia IUTAM* 4 (2012), pp. 15–26. DOI: 10.1016/j.piutam.2012.05.003. URL: https://doi.org/10.1016/j.piutam.2012.05.003.

[46] Lenton Furnaces & Ovens. *Lenton Furnaces & Ovens: Laboratory Furnaces Brochure*. Brochure No. 7443, accessed via personal archive. Parsons Lane, Hope, Hope Valley, S33 6RB, United Kingdom, 2016. URL: https://www.lentonfurnaces.com.

[47] D. Yadav, A. Kumar, and R. Chandra. “A review on ultra-high-temperature materials for aerospace applications”. In: *Journal of Materials Research and Technology* 9.6 (2020), pp. 14434–14458. DOI: 10.1016/j.jmrt.2020.10.036.

[48] M.C. Morris et al. *Standard X-ray Diffraction Powder Patterns: Section 21*. Vol. 25, Section 21. NBS Monograph. National Bureau of Standards, 1987. URL: https://nvlpubs.nist.gov/nistpubs/Legacy/MONO/nbsmonograph25-21.pdf.

[49] C. Li et al. “Effect of Zirconia Polymorph on Vapor-Phase Ketonization over Metal Oxide Catalysts”. In: *Industrial & Engineering Chemistry Research* 61.8 (2022), pp. 2933–2943. DOI: 10.1021/acs.iecr.1c04862. URL: https://doi.org/10.1021/acs.iecr.1c04862.

[50] A. Bumajdad et al. “Controlled Synthesis of ZrO□ Nanoparticles with Tailored Size, Morphology and Crystal Phases via Organic/Inorganic Hybrid Films”. In: *Scientific Reports* 8.1 (2018), pp. 1–12. DOI: 10.1038/s41598-018-22088-0. URL: https://doi.org/10.1038/s41598-018-22088-0.

[51] S.I. Moseenkov et al. “Investigation of Amorphous Carbon in Nanostructured Carbon Materials: A Comparative Study by TEM, XPS, Raman Spectroscopy and XRD”. In: *Materials* 16.3 (2023), p. 1112. DOI: 10.3390/ma16031112. URL: https://doi.org/10.3390/ma16031112.

[52] Nicolas Döbelin and René Kleeberg. *Profex: A graphical user interface for the Rietveld refinement program BGMN*. https://profex.doebelin.org. Accessed 8 June 2025. 2015.

[53] B. D. Cullity and S. R. Stock. *Elements of X-ray Diffraction*. 3rd. Prentice Hall, 2001.

[54] David Tuschel. “Exploring Resonance Raman Spectroscopy”. In: *Spectroscopy* 33.12 (2018). Accessed 8 June 2025, pp. 16–21. URL: https://www.spectroscopyonline.com/view/resonance-raman-spectroscopy.

[55] M Gawęda K. Suchorab and L. Kurpaska. “Comparison of Raman imaging assessment methods in phase determination and stress analysis of zirconium oxide layer”. In: *Spectrochimica Acta Part A: Molecular and Biomolecular Spectroscopy* (2023).

[56] Y. M. Han et al. “Hydrogenation Influence on Crack Initiation and Fretting Corrosion Mechanism of Zirconium Alloy Under Partial Slip Regime in High Temperature Pressurized Water Environment”. In: *SSRN Electronic Journal* (2024). DOI: 10.2139/ssrn.4724730. URL: https://doi.org/10.2139/ssrn.4724730.

A

Appendix

The following graph displays the temperature and pressure profile used during SPS to synthesize the ZrC samples from this study.

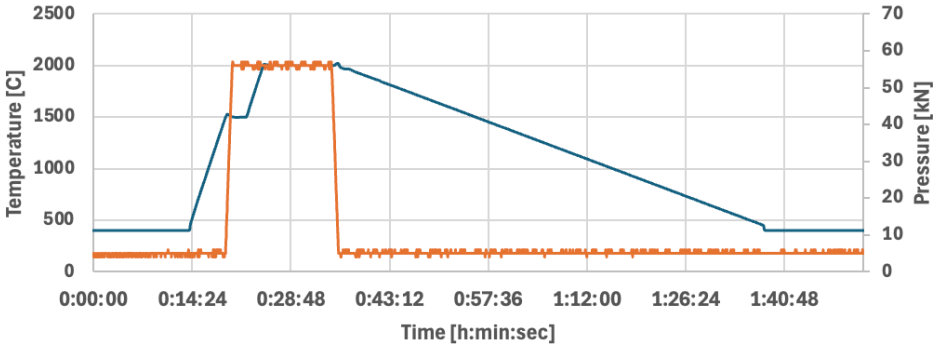

Figure A.1: Temperature and pressure profile during SPS